

Recent Progress in Solar-Blind Deep-Ultraviolet Photodetectors Based on Inorganic Ultrawide Bandgap Semiconductors

Chao Xie, Xing-Tong Lu, Xiao-Wei Tong, Zhi-Xiang Zhang, Feng-Xia Liang,* Lin Liang, Lin-Bao Luo,* and Yu-Cheng Wu*

Due to its significant applications in many relevant fields, light detection in the solar-blind deep-ultraviolet (DUV) wavelength region is a subject of great interest for both scientific and industrial communities. The rapid advances in preparing high-quality ultrawide-bandgap (UWBG) semiconductors have enabled the realization of various high-performance DUV photodetectors (DUVPDs) with different geometries, which provide an avenue for circumventing numerous disadvantages in traditional DUV detectors. This article presents a comprehensive review of the applications of inorganic UWBG semiconductors for solar-blind DUV light detection in the past several decades. Different kinds of DUVPDs, which are based on varied UWBG semiconductors including Ga_2O_3 , $\text{Mg}_x\text{Zn}_{1-x}\text{O}$, III-nitride compounds ($\text{Al}_x\text{Ga}_{1-x}\text{N}$ /AlN and BN), diamond, etc., and operate on different working principles, are introduced and discussed systematically. Some emerging techniques to optimize device performance are addressed as well. Finally, the existing techniques are summarized and future challenges are proposed in order to shed light on development in this critical research field.

extreme ultraviolet (EUV) spectrum (from 10 to ≈ 120 nm).^[3,4] As most UV radiation including UVB, UVC, and EUV light can be absorbed by the earth's atmosphere and the stratospheric ozone layers,^[4] UV radiation from the sunlight with wavelength shorter than ≈ 280 nm cannot penetrate the atmosphere and reach the surface of the earth, for which the 200–280 nm is typically referred to as solar-blind spectrum region.^[5] In the past decades, benefiting from the advance of semiconductor industry in leaps and bounds,^[6,7] UV light detection, solar-blind deep-ultraviolet (DUV) photodetection in particular has been a subject of grand interest in recent years because of the significant applications in a variety of fields including remote control, chemical analysis, flame detection, missile warning system, and secure space-to-space communications.^[5,8–12]


1. Introduction

Ultraviolet (UV) radiation refers to the electromagnetic radiation with typical wavelength range from 10 to 400 nm, which constitutes $\approx 10\%$ of the total solar spectrum.^[1,2] According to the definition recommended by the International Commission Illumination (ICE), UV radiation is commonly divided into the following subregions: ultraviolet A (UVA) spectrum (320–400 nm), ultraviolet B (UVB) spectrum (from 280 to 320 nm), ultraviolet C (UVC) spectrum (from 100 to 280 nm), and

Traditionally, the detection of UV light is dominated by the photomultiplier tubes (PMTs), thermal detectors, narrow bandgap semiconductor photodiodes, or charged-coupled devices (CCDs).^[8,13] The PMTs hold advantages of being highly sensitive to UV photons while being “blind” to photons with wavelengths longer than the cutoff wavelength of the detectors. However, being bulky and heavy, they usually require high voltage (>100 V) for operation, which results in high power consumption and inconvenient use. Thermal detectors including pyrometers and bolometers that are normally employed for calibration in the UV region have proved to be as useful as absolute radiometric standards. Nevertheless, their response is very slow and wavelength independent, rendering them unsuitable for rapid and wavelength selective UV light detection. In comparison, semiconductor photodiodes and CCDs require only moderate voltages for operation. What is more, small, lightweight, and low cost semiconductor photodiodes usually exhibit good linearity and sensitivity as well as capability for high-speed operation. In spite of these outstanding characteristics, there is no denying the fact that these devices have their own weaknesses. Since Si possesses a narrow bandgap of 1.12 eV, costly high-pass optical filters are required to block out visible and infrared photons, leading to a significant loss of effective area of the system. In addition, device aging is inevitable due to exposure to radiation

Dr. C. Xie, X.-T. Lu, X.-W. Tong, Z.-X. Zhang, Prof. L.-B. Luo
School of Electronic Science and Applied Physics
Hefei University of Technology
Hefei 230009, China
E-mail: luolb@hfut.edu.cn

Dr. F.-X. Liang, L. Liang, Prof. Y.-C. Wu
School of Materials Science and Engineering
Hefei University of Technology
Hefei 230009, China
E-mail: fxliang@hfut.edu.cn; ycwu@hfut.edu.cn

 The ORCID identification number(s) for the author(s) of this article can be found under <https://doi.org/10.1002/adfm.201806006>.

DOI: 10.1002/adfm.201806006

with energy much higher than the semiconductor bandgap. Moreover, due to light absorption by the surface passivation layers, typically Si oxide, quantum efficiency in the DUV range is greatly reduced. The passivation layers are also easily degraded by UV illumination. Finally, for highly sensitive UV photodetection, the detectors need to be cooled to reduce dark current; the cooled detectors, however, behave like cold traps for contaminants which degrade the detectivity.

In the past two decades, the emergence of UV photodetectors based on wide-bandgap (WBG) semiconductors has opened up an avenue to circumvent the above-mentioned dilemma. The WBG semiconductors such as SiC, GaN, and some group II–V compounds, typically have bandgaps exceeding ≈ 3.10 eV, enabling room-temperature detectors to possess fast response speed, and offering intrinsic visible-blindness (response cutoff wavelength: ≈ 400 nm).^[14–16] Moreover, these semiconductors generally possess significantly higher thermal conductivity than Si, which renders them suitable for operation in harsh environments (e.g., high temperature and high power). The electron velocity of these materials at large electric fields is generally higher than that of common semiconductors, although WBG semiconductors exhibit relatively lower electron and hole mobilities. Compared with the abovementioned conventional WBG semiconductors, ultrawide-bandgap (UWBG) semiconductors, as the next generation of semiconductor materials with bandgaps significantly wider than the 3.4 eV of GaN, are particularly suitable for solar-blind DUV light detection.^[17–20] This class of materials normally includes Ga_2O_3 , $\text{Mg}_x\text{Zn}_{1-x}\text{O}$, III-nitride compounds ($\text{Al}_x\text{Ga}_{1-x}\text{N}/\text{AlN}$ and BN), diamond, and some other emerging semiconductors.^[21] Based on these UWBG semiconductors, a number of high-performance DUV photodetectors (DUVPDs) with high responsivity, high rejection ratio, fast response speed, and low noise have been developed in recent years.^[8–11,13,22]

In this paper, we provide a comprehensive review of the fabrication of inorganic UWBG semiconductors for solar-blind DUV photodetection in the past decades. As UV photodetectors operating in UVA and UVB regions have been summarized previously,^[4,6,7,23,24] they will not be discussed in detail here. We first give a brief introduction to common device geometries normally adopted by current solar-blind DUVPDs, along with their working mechanisms, pros/cons and important performance parameters. Then, the efforts and significant development in different kinds of solar-blind DUVPDs based on a variety of UWBG semiconductors including Ga_2O_3 , $\text{Mg}_x\text{Zn}_{1-x}\text{O}$, III-nitride compounds ($\text{Al}_x\text{Ga}_{1-x}\text{N}/\text{AlN}$ and BN), diamond, etc., are introduced and discussed systematically. Some emerging techniques to optimize device performance are also included in this paper. In the last section, summaries of the existing techniques and challenges are provided to guide future research activity in this field.

2. Device Geometries and Performance Parameters

2.1. Device Geometries

According to previous reports, numerous types of device structures involving photoconductors, metal–semiconductor–metal (MSM) photodetectors, Schottky photodiodes, avalanche



Chao Xie obtained his B.S. and Ph.D. degrees from the Hefei University of Technology in 2009 and 2014, respectively. He then worked as a postdoctoral research fellow at The Hong Kong Polytechnic University and the Hanyang University, respectively, for the subsequent three years. He is currently an associate professor at the School of Electronic Science and Applied Physics, HFUT. His research interests focus on the development of high-performance optoelectronic devices based on novel functional materials (1D nanostructures, 2D materials, perovskite materials, etc.).



Feng-Xia Liang received her Ph.D. degree from the City University of Hong Kong in 2012. She is currently an Associate Professor in the School of Materials Science and Engineering at the Hefei University of Technology. Her research interest includes the synthesis of low-dimensional semiconductor nanostructures for chemical, biological, and optoelectronic device applications.



Lin-Bao Luo received his Ph.D. from the Department of Physics and Materials Sciences, City University of Hong Kong, in 2009. After one and a half years of postdoc work, he joined the School of Electronic Sciences and Applied Physics, Hefei University of Technology, as a full professor. His research interest is mainly focused on the controlled fabrication of graphene and low-dimensional semiconductor nanostructures for high-performance optoelectronic devices and system applications.

photodiodes, and p–n (p–i–n) photodiodes have been developed for solar-blind DUVPDs. These devices usually have different working mechanisms and possess respective advantages and limitations for DUV photodetection. In this section, we will classify the current solar-blind DUVPDs architectures on the basis of their working principles and pros/cons.

2.1.1. Photoconductors

A photoconductor that is structurally characterized by a semiconductor layer as a channel with two Ohmic contacts affixed to opposite ends of the channel constitutes one of the most common device architectures for DUV detection.^[25] The working principle relies on the process in which photon absorption by the semiconductor produces excess free carriers and gives an increase in conductivity. In the darkness, only a small current (dark current, I_{dark}) is allowed to flow across the channel under a bias voltage. Under illumination, the semiconductor can absorb photons with energy higher than its bandgap, which generates electron–hole pairs. The electron–hole pairs are then separated by the applied voltage, and the free electrons and holes drift oppositely toward electrodes. This process gives rise to a change in channel conductivity, which depends strongly on the intensity of the incident radiation. It is worth noting that the photocurrent ($I_{\text{ph}} = I_{\text{light}} - I_{\text{dark}}$, I_{light} is the channel current under illumination) is primarily contributed by the photoexcited majority carriers since they are free to travel across the Ohmic contacts. However, the presence of minority carriers also has a profound influence on the photocurrent. Because of the presence of injection barriers between minority carriers and electrodes, minority carriers will pile up at one of the contacts. To maintain charge neutrality, additional majority carriers are then supplied from the other contact and circulate in the channel until the minority carriers recombine. This process can produce “photoconductive” gain (G), which depends mainly upon the ratio of the minority carrier lifetime to the majority carrier transit time across the channel. A longer minority carrier lifetime is thus preferable to achieve a larger gain. However, the response time related to the carrier recombination process is also determined by the minority carrier lifetime. A larger gain will slow down the response time. To achieve a reasonable overall performance, a tradeoff should be made between gain and response speed in a photoconductor. An undesirable drawback of photoconductors is the relatively high dark current. Nonetheless, due to the simple device architecture and ease of fabrication, photoconductors are useful for applications where fast response and low dark current are not necessities.

2.1.2. MSM Photodetectors

MSM photodetectors are also planar devices that basically consist of a poorly-doped semiconductor layer with two Schottky metallic contacts deposited on the surface to form back-to-back connected Schottky barrier junctions.^[26] Usually, the metal contacts take the configuration of interdigitated fingers, which allows for a large photosensitive surface area while keeping a short distance between the fingers. The operational mechanism resembles that of the photoconductors. However, due to the presence of Schottky barriers, a sufficiently high applied voltage is often required to separate the photocarriers and drive them as quickly as possible to the electrodes. Owing to the rectifying nature of the contacts, MSM devices normally display relatively lower dark current compared with photoconductors. In addition, given the intrinsically low capacitance per unit area, MSM

photodetectors usually possess fast response speed limited by the carrier transit time. High photoconductive gain is also possible in MSM photodetectors, which could be explained by the following reasons. First of all, photoconductivity is caused by long lifetime traps at the semiconductor surface between the channels. The photocarriers trapped at the surface create an asymmetric electric charge distribution, which modifies the potential distribution at metal-semiconductor contact and eventually induces additional carrier injection from the electrode via tunneling process. The second reason is associated with the minority carrier piling up or trapping in the vicinity of one electrode, which induces injection of majority carriers from another electrode through the tunneling process. Under a sufficiently high electric field, the gain due to impact ionization in the semiconductor could also be observed. In addition, due to the electrode shadowing effect, MSM photodetectors usually show relatively lower external quantum efficiency (EQE), constituting the main limitation that can be mitigated through some strategies like optimizing the width and pitch of electrode fingers and using semitransparent electrodes. With the good device performance, simple device structure, and ease of manufacturing, MSM photodetectors are extremely attractive for monolithic integration with other components on optoelectronic circuits.

2.1.3. *p–n* (*p–i–n*) Photodiodes

p–n photodetectors are normally geometrically composed of junctions with opposite doping types.^[27] The working mechanism relies essentially on the photovoltaic effect: due to the difference in work functions, charge transfer takes place between two semiconductors until their Fermi levels align. In the meantime, a region of free charges (the space charge region) is depleted near the interface and a built-in electric field is created. As a result, an energy barrier preventing the flow of charge carriers across the junction is formed because of the discontinuity in allowed energy states of the two semiconductors at equilibrium state. Therefore, *p–n* photodiodes normally exhibit rectifying behavior, that is, an asymmetric current–voltage characteristic in the darkness. Upon illumination, photons with energy higher than the bandgap are absorbed by the semiconductors, which creates electron–hole pairs in the material on both sides of the junction. The electrons and holes generated within a diffusion length from the junction travel to the space charge region, where they are separated by the built-in electric field and then propelled toward opposite directions. The minority carriers are easy to accelerate and become the majority carriers on the other side of the junction. If the photodiode is short-circuited, the photoexcited carriers flow across the external circuit and generate a sizeable photocurrent (short-circuit current, I_{SC}). Nevertheless, open-circuit will lead to accumulation of electrons and holes on the opposite sides of the junction produce a photovoltage (open-circuit voltage, V_{OC}). The *p–n* photodiodes can operate at two modes: 1) photovoltaic (operation at zero bias) and 2) photoconductive (operation under reverse bias). At the first mode, a photodiode usually has an improved specific detectivity (D^*) and maximum linearity and sensitivity due to relatively low dark current. Under reverse bias, the

depletion region will be widened and the photodiode can have a faster response speed thanks to the reduced transit time and lowered diode capacitance.

As a derivative of p–n photodiodes, p–i–n photodiodes have an intrinsic absorbing layer between a p-type, highly doped and transparent contact layer and an n-type, highly doped contact layer. This structure has been widely explored because it is feasible to optimize the quantum efficiency and the response speed by tailoring the depletion layer thickness (the intrinsic layer). The primary drawback of photodiodes is that they normally have a maximum gain of unity, smaller than that of photoconductors and MSM photodetectors.

2.1.4. Schottky Photodiodes

Schottky photodiodes share some similarities with p–n (p–i–n) photodiodes in that both devices exploit the photovoltaic effect.^[28] The simplest Schottky photodiode is basically made up of a metal layer in contact with a semiconductor, whose work function is quite different from that of a metal. Upon illumination with photon energy larger than the bandgap, optical absorption occurs in the semiconductor and the general characteristics of the devices are very similar to those of p–n (p–i–n) photodiodes. Alternatively, Schottky photodiodes can explore the internal photoemission process. For smaller photon energy, the photoexcited electrons in the metal can have a chance to surmount the Schottky barrier and contribute to the photocurrent. However, in practical application, the quantum efficiency from the internal photoemission is usually very low (typically less than 1%). Due to the fact that the dark current of Schottky photodiodes is dominated by the thermionic emission of majority carriers which does not suffer from charge storage of minority diffusion current, Schottky photodiodes normally possess a faster response speed than p–n (p–i–n) photodiodes. Another advantage lies in that high-temperature processing for diffusion or implantation annealing is not required in the fabrication of Schottky photodiodes.

2.1.5. Avalanche Photodiodes

Under sufficiently large reverse bias, photogenerated electrons can have sufficient energy to initiate impact ionization, which causes avalanche multiplication in photodiodes (avalanche photodiodes), and thus provides internal current gain. The criteria with regard to the quantum efficiency and response speed for avalanche photodiodes are similar to those for nonavalanching photodiodes like p–n photodiodes. Usually, avalanche photodiodes hold the advantages of high response speed, high sensitivity, and large current gain. However, high gain often comes at the expense of noise. That means, for some special application, the noise should be appropriately taken into consideration.

2.1.6. Phototransistors

A phototransistor is typically a three-layer semiconductor device, whose geometry resembles normal transistor except

for the absence of base terminal, a much larger area of the base and collector regions in the case of the phototransistor.^[25] Compared with photodiodes, phototransistors can have higher responsivity and sensitivity owing to the current gain. However, they usually display slower response speed than photodiodes. For solar-blind DUV light detection, heterojunction phototransistors are often employed. This type of devices has a typical geometry consisting of double layers of a heterojunction, where one layer serves as the light absorbing media and another layer acts as the charge carrier transport channel. Under DUV illumination, electron–hole pairs are produced in the light absorbing layer, and subsequently, one type of carrier drifts toward the transport channel, leaving another type of carrier trapped in the optical absorbing layer due to the alignment of energy band levels between two materials. The photocarriers are then collected by source–drain electrodes at the opposite ends of the channel, giving rise to the generation of photocurrent.

Since the working mechanisms of solar-blind DUVPDs discussed in this review paper are based on the photoelectric effect, the long detecting wavelength limit (λ), which is usually named as cutoff wavelength, is directly related to energy transition (ΔE) in the device operation with the following equation: $\lambda = \frac{hc}{\Delta E} = \frac{1240}{\Delta E(\text{eV})}$ (nm), where h is the Planck's constant and c is the speed of light.^[25] In most cases, the energy transition ΔE is the bandgap of the semiconductors. However, it can also be the barrier height for Schottky photodiodes or transition energy between an impurity (defect) level and the band edge for devices where photocarrier excitation stems from the impurity (defect) level within the bandgap of the semiconductors. Therefore, for the majority of DUVPDs discussed in this paper, their cutoff wavelength values are determined by the bandgap of the UWBG semiconductors.

2.2. Performance Parameters

Hitherto, a large number of solar blind DUVPDs have been realized by using different UWBG semiconductors (**Figure 1**). Even though these device geometries vary from one device to another, their photoresponse capability should be assessed in order to compare the device performance in a quantitative way. **Table 1** summarizes some key performance parameters that are often used to evaluate the performance of solar-blind DUVPDs.^[29,30]

3. Ga₂O₃

Ga₂O₃, an important semiconductor oxide, which was first reported in the 1950s, has recently emerged as a promising candidate for a range of power electronic devices with capabilities beyond existing technologies.^[9] Considering the difference in atomic arrangement, there are seven commonly identified polymorphs (i.e., different forms or crystal structures) of Ga₂O₃, which are usually referred to as amorphous, polycrystalline, corundum (α), monoclinic (β), defective spinel (γ), orthorhombic (ϵ), and orthorhombic (δ) phases.^[31–33] Among these phases, the monoclinic β -gallia (β -Ga₂O₃) is the most

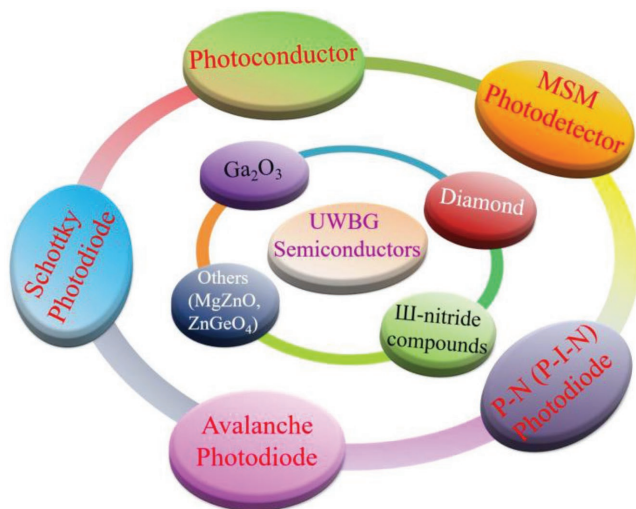


Figure 1. Schematic illustration of various types of solar-blind DUVPDs based on a variety of UWBG semiconductors.

stable crystal structure under normal conditions, and thus has been extensively explored. Due to its appealing properties including wide bandgap exceeding ≈ 4.6 eV at room temperature, large dielectric constant of 10.2–14.2 and high breakdown field strength of 3.5 MV cm^{-1} , $\beta\text{-Ga}_2\text{O}_3$ has found a wide range of applications such as solar-blind DUVPDs, gas sensors, solar cells, catalysis, and transparent conducting electrodes for a variety of optoelectronic devices.^[34,35] Moreover, this material has high chemical and thermal stabilities, making it extremely attractive for applications in high temperature and harsh environments. Besides β -phase, other metastable polymorphs including $\epsilon\text{-Ga}_2\text{O}_3$ and $\gamma\text{-Ga}_2\text{O}_3$ have also been explored for DUV photodetection, which exhibit good device performance.^[36] In this section, we will introduce the development of various types of solar-blind DUVPDs assembled primarily from $\beta\text{-Ga}_2\text{O}_3$ with different structures including thin films, nanostructures, and bulk crystals.

Table 1. Performance parameters of solar-blind DUVPDs.

Quantity	Symbol	Unit	Definition
Responsivity	R	$\text{A W}^{-1}, \text{V W}^{-1}$	The ratio between the photocurrent or photovoltage and the incident optical power on the photodetector.
External quantum efficiency/internal quantum efficiency	EQE/IQE	Unitless	In a photodiode, the ratio between the number of electron–hole pairs with contribution to the photocurrent and the number of incident/absorbed photons.
Photoconductive gain	G	Unitless	In a photoconductor, the ratio between the number of electrons collected by the electrode and the number of incident photons.
Dark current	I_{dark}	A	Current flowing in the photodetector in the absence of light illumination.
Response speed	τ_r, τ_d	s	Rise time (τ_r) and decay time (τ_d) are defined as the time needed for the photoresponse to increase from 10% to 90% or drop from 90% to 10% of its peak value.
Noise current	I_{noise}	$\text{A Hz}^{-1/2}$	The random root mean square fluctuation in current when bandwidth is limited to 1 Hz.
Noise-equivalent power	NEP	$\text{W Hz}^{-1/2}$	The minimum impinging optical power required to achieve a signal-to-noise ratio of unity in a 1 Hz bandwidth.
Specific detectivity	D^*	$\text{cm Hz}^{-1/2} \text{W}^{-1}$ [Jones]	A parameter for comparing the sensitivity between photodetectors with different device area A and bandwidth B . $D^* = (AB)^{-1/2}/\text{NEP}$.
Response rejection ratio	R_a/R_b	Unitless	The ratio between responsivity at light wavelength a and that at light wavelength b .

3.1. Photoconductors

3.1.1. Ga_2O_3 Thin Films

Photoconductors based on $\beta\text{-Ga}_2\text{O}_3$ have been widely studied by many groups for the simple device structure and ease of fabrication. $\beta\text{-Ga}_2\text{O}_3$ thin films are usually grown on sapphire substrates via various synthetic methods. The reported approaches by far include pulsed spray pyrolysis,^[37] the sol–gel method,^[38] molecular beam epitaxy (MBE, plasma-assisted MBE, laser MBE, etc.),^[39–44] precursor oxidation,^[45] metalorganic chemical vapor deposition (MOCVD),^[46–49] low-pressure chemical vapor deposition (LPCVD),^[50] and magnetron sputtering.^[51–54] During these preparation processes, high temperature annealing (500–1200 °C) is usually needed to guarantee a good crystalline quality. Using ethanol solution of gallium trichloride as a precursor, $\beta\text{-Ga}_2\text{O}_3$ thin films have been deposited by pulsed spray pyrolysis in air.^[37] The films exhibited an optical bandgap of ≈ 5.16 eV and a high optical transmittance exceeding 80% for $\lambda > 275$ nm, and were strongly sensitive to 254 nm DUV radiation. Kokubun et al. reported the synthesis of polycrystalline $\beta\text{-Ga}_2\text{O}_3$ films through a sol–gel method, during which heat treatment at different temperatures greatly affected the bandgap and the photoresponse properties of the films.^[38] As shown in **Figure 2a,b**, with the temperature increasing from 600 to 1200 °C, the bandgap increased from 4.9 to 5.6 eV. The peak spectral response turned out to shift toward a shorter wavelength. However, the responsivities were very low, with the maximum value of only $8 \times 10^{-5} \text{ A W}^{-1}$. It should be mentioned that the barrier heights between UWBG semiconductors and metals are large and not easy to achieve reliable Ohmic contact. To resolve this issue, researchers have tried different electrode materials such as Au, Al/Ti, Ni/Au, Ti/Au, and Cr/Au.^[37–44,46–51]

Later on, the MBE technique also proved to be a rational approach to grow $\beta\text{-Ga}_2\text{O}_3$ films with improved crystalline quality. Thin films with a sharp absorption edge at ≈ 5.0 eV have a small dark current of 1.2 nA at a bias of 10 V.^[39] Under

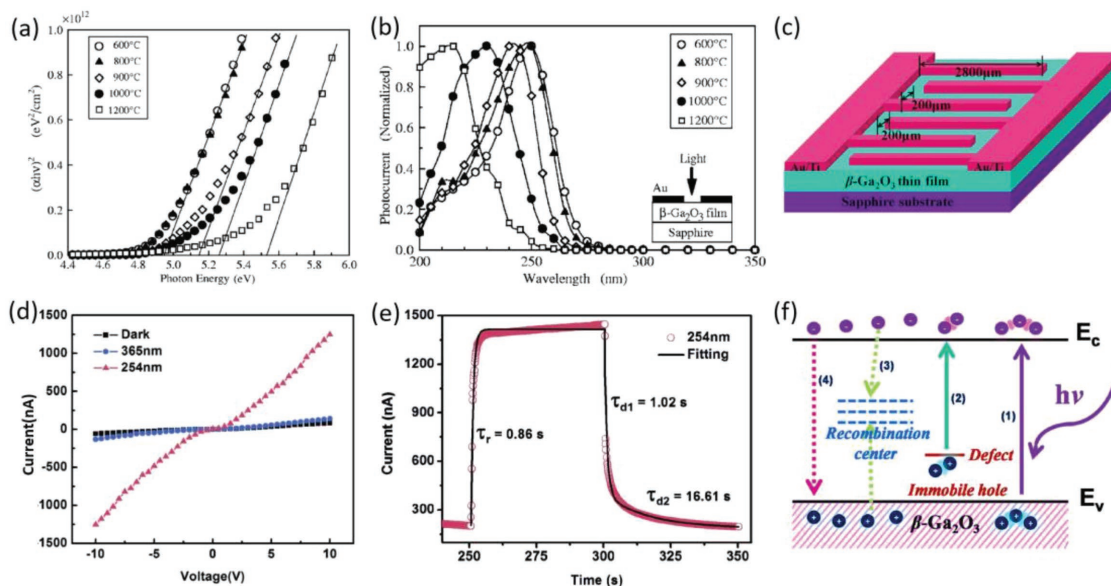


Figure 2. a) Square of absorption coefficient as a function of photon energy for $\beta\text{-Ga}_2\text{O}_3$ films prepared at various temperatures. b) Spectral responses of the photoconductors based on $\beta\text{-Ga}_2\text{O}_3$ films prepared at various temperatures. Reproduced with permission from American Institute of Physics Publishing.^[38] c) Schematic diagram of a photoconductor based on $\beta\text{-Ga}_2\text{O}_3$ thin film. d) Current–voltage (I – V) characteristics of the $\beta\text{-Ga}_2\text{O}_3$ photodetector in dark, under 365 and 254 nm light radiation. e) Experimental curve and fitted curve of the current rise and decay process to 254 nm illuminations. f) Schematic diagram illustrating the carrier transport mechanism in the $\beta\text{-Ga}_2\text{O}_3$ photodetector. Reproduced with permission.^[40] Copyright 2014, Optical Society Publishing.

254 nm illumination, the device can exhibit a photocurrent of 3.7 μA , yielding a large $I_{\text{light}}/I_{\text{dark}}$ ratio of $\approx 3.1 \times 10^3$. The responsivity reached 0.037 A W^{-1} , with an EQE of 18%. In another study, Guo et al. found that $\beta\text{-Ga}_2\text{O}_3$ film prepared by laser MBE was highly sensitive to 254 nm radiation while almost blind to 365 nm illumination.^[40] Figure 2c shows a schematic illustration of the detector. The photocurrent increased by more than 1 order of magnitude upon 254 nm illumination (Figure 2d). Interestingly, the device exhibited a faster rise edge (<1 s) and a relatively slower decay edge with two time constants of 1.02/16.61 s (Figure 2e), which could be explained by the presence of charge trapping/detrapping due to the deep trap states within the bandgap of $\beta\text{-Ga}_2\text{O}_3$, as illustrated by Figure 2f. Furthermore, the crystalline quality of $\beta\text{-Ga}_2\text{O}_3$ has been improved by introducing a $\beta\text{-Ga}_2\text{O}_3$ homo-self-templated buffer layer during MBE growth process^[41] or employing a vacuum-annealed c -plane sapphire substrate.^[42,43] It was revealed that DUVPDs made from $\beta\text{-Ga}_2\text{O}_3$ with buffer layer exhibited not only slightly enhanced photocurrent, but also significantly suppressed dark current.^[41] As a result, the $I_{\text{light}}/I_{\text{dark}}$ ratio increased by 10 times and reached 10^4 . The responsivity and EQE values achieved in this work are 259 A W^{-1} and $7.9 \times 10^4\%$, respectively. Further study found that once the sapphire substrate was annealed, impurity scattering related to structural disorders was suppressed, as a result, the carrier mobility of the prepared $\beta\text{-Ga}_2\text{O}_3$ films was greatly enhanced.^[42] Accordingly, both currents in the darkness and upon 254 nm radiation increased significantly, leading to an enhanced responsivity from 44 to 153 A W^{-1} . However, due to the reduction in the crystallographic defects impacting internal gain and carrier recombination, some degradations in $I_{\text{light}}/I_{\text{dark}}$ ratio and response speed were observed.

The photoresponse can be further improved through some strategies such as impurity doping,^[46,48,49,51,55–57] exploration of the carrier multiplication process,^[47] and adoption of Zener diodes.^[44] It has been reported that implantation of Si ions followed by thermal annealing to activate the ions can facilitate the formation of Ohmic contacts between $\beta\text{-Ga}_2\text{O}_3$ and Ti/Au electrodes, and greatly enhance the electrical conductivity of the films.^[46,48] DUVPDs based on Si-doped $\beta\text{-Ga}_2\text{O}_3$ films can operate properly over a large temperature range from 25 to 350 $^\circ\text{C}$.^[48] Unlike thermal quenching in sensitivity observed in many photoconductors, the sensitivity increased with high temperatures for detectors in this work. This effect could be ascribed to the presence of defect states within $\beta\text{-Ga}_2\text{O}_3$ bandgap, which enables photocurrent generation at high temperatures. As a result, the responsivity under 254 nm illumination increased from 5 to 36 A W^{-1} over the above temperature range. Alema et al. employed MOCVD method to grow Zn-doped $\beta\text{-Ga}_2\text{O}_3$ (ZnGaO) films with a cutoff wavelength of ≈ 260 nm, which is similar to that of undoped films.^[49] Due to the presence of a high concentration of defects including oxygen vacancies and substitutional defects that afford large internal gain, the as-grown ZnGaO and $\beta\text{-Ga}_2\text{O}_3$ films displayed peak responsivities of $\approx 3.6 \times 10^3$ and 1.7×10^4 A W^{-1} , respectively. Once the sample was annealed, both currents in the darkness and under DUV illumination decreased drastically, resulting in significantly dropped responsivity values of 210 and 46 A W^{-1} , respectively. Meanwhile, the photoresponse rejection ratio (R_{232}/R_{320}) increased dramatically from 10^3 to 5×10^4 and 2×10^4 for annealed ZnGaO and $\beta\text{-Ga}_2\text{O}_3$ detectors. The concentration of Zn dopant has a great influence on the crystal lattice spacing and the bandgap of $\beta\text{-Ga}_2\text{O}_3$ films.^[51] In addition, due to decreased

concentration of oxygen vacancies, the Zn-doped β -Ga₂O₃ device exhibited a lower dark current, a higher $I_{\text{light}}/I_{\text{dark}}$ ratio, and a faster response speed. Recently, Hu et al. reported a high-gain photoconductor made from MOCVD-derived β -Ga₂O₃ films.^[47] Upon ≈ 255 nm illumination, the $I_{\text{light}}/I_{\text{dark}}$ ratio exceeded 5×10^3 and the responsivity was as high as 17 A W^{-1} . The relatively large electric field existing at the film surface covered by Au interdigital electrode greatly accelerated photocarriers, which impacted with the lattice of the Ga₂O₃ to release their kinetic energy and therefore provided additional electrons and holes. This carrier multiplication process was responsible for the high gain. In a recent work, Rafique et al. have studied the effect of thermal annealing on photoresponse characteristics of DUVPDs based on LPCVD-grown β -Ga₂O₃ films.^[50] The annealing can help to reduce oxygen or oxygen-related vacancies in the films, and therefore reduce trapped photocarriers to a great degree. As a consequence, the detector after annealing exhibited lower dark current decreasing by ≈ 2 orders of magnitude and higher photocurrent increasing by 10 times at 250 nm. Accordingly, the $I_{\text{light}}/I_{\text{dark}}$ ratio increased significantly from 3.5×10^3 to 1.44×10^6 . What is more, thanks to the reduced sub-bandgap defects, the photoresponse rejection ratio (R_{250}/R_{370}) was enhanced by 2–3 orders of magnitude.

In addition, α -Ga₂O₃ or Sn-doped α -Ga₂O₃ thin films have been prepared by laser MBE technique and utilized for DUV photodetection.^[18,58,59] The α -Ga₂O₃ possesses a bandgap of ≈ 5.15 eV that is slightly larger than that of β -Ga₂O₃.^[58] Detectors made from α -Ga₂O₃ film exhibited high sensitivity to 254 nm DUV radiation, while they were virtually blind to 365 nm illumination. The bandgap of Sn-doped α -Ga₂O₃ decreased linearly with Sn content's increasing, which made it possible to tune their DUV photoresponse.^[18] Photodetectors based on Ga_{1.8}Sn_{0.2}O₃ films have achieved an $I_{\text{light}}/I_{\text{dark}}$ ratio of

1.4×10^2 and a maximum responsivity of $9.55 \times 10^{-2} \text{ A W}^{-1}$. Furthermore, Zhao et al. found that the oxygen partial pressure had a pronounced effect on the crystal lattice spacing and electrical conductivity of the films.^[59] By reducing the impurity altitude compensation effect originating from mixture valence of Sn²⁺ and Sn⁴⁺ ions, increased dark current and photocurrent, along with diminished relaxation time constants were observed in DUVPDs based on α -phase Ga_{1.4}Sn_{0.6}O₃ films.

3.1.2. Ga₂O₃ Nanostructures

Apart from Ga₂O₃ thin films, low-dimensional Ga₂O₃ nanostructures including nanowires (NWs),^[60–66] nanobelts (NBs),^[67–69] nanosheets/nanoflakes,^[70,71] and nanoflowers (NFs)^[72] have also been explored for solar-blind DUV photodetection. By virtue of significant size/surface effect and quantum confinement effect, these nanostructures usually demonstrated attractive advantages of enhanced optical absorption, improved carrier separation and collection, more surface states to interact with surroundings, etc.^[23,73] β -Ga₂O₃ NWs have been successfully grown by some techniques such as CVD method by using Ga metal placed onto alumina substrate^[60,65] or a powder mixture of Ga₂O₃ and graphite as sources,^[61] and heating the GaN/sapphire template.^[62,64] The growth temperature was critical to the density, average length, and diameter of the NWs, and high growth temperature was apt to obtain high crystalline quality NWs. Detectors based on individual NW usually exhibited the dark current on the scale of several to hundreds of picoamperes, but once illuminated by DUV light (254 or 255 nm), the current increased drastically by maximum 3 orders of magnitude. Li et al. reported a high-performance DUVPD using bridged β -Ga₂O₃ NW as building blocks (Figure 3a–c).^[61] The as-fabricated nanodevice

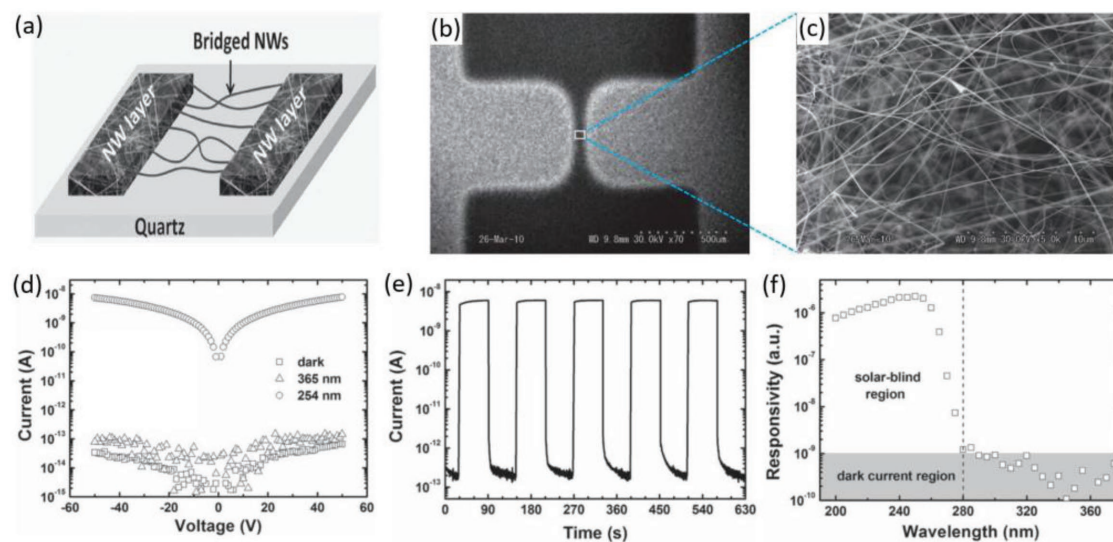


Figure 3. a) Schematic diagram of the bridged NW structure showing the electrodes made of thick β -Ga₂O₃ NW layers and the bridged NWs crossing the gap between the NW electrodes. b) A scanning electron microscopy (SEM) image of the bridged β -Ga₂O₃ NW structure. c) A magnified view of the bridged β -Ga₂O₃ NWs crossing the gap. d) I - V characteristics of the bridged β -Ga₂O₃ NWs in dark (squares), under 365 nm light (triangles), and under 254 nm light (circles). e) Time-dependent photoresponse of the bridged β -Ga₂O₃ NWs measured in dry air under UVC ($\approx 2 \text{ mW cm}^{-2}$ at 254 nm) illumination at a bias voltage of 50 V. f) Spectral response of the bridged β -Ga₂O₃ NWs revealing that the device is blind to solar light. The dashed line indicates the lowest wavelength of the solar spectrum on earth. Reproduced with permission.^[61] Copyright 2010, Wiley-VCH.

possessed an extremely low dark current of only ≈ 0.2 pA even at a large voltage bias of 50 V (Figure 3d). Under 254 nm illumination, the detector exhibited a stable and reproducible photoresponse with a high $I_{\text{light}}/I_{\text{dark}}$ ratio of $\approx 3 \times 10^4$ and a fast response speed (decay time < 20 ms) (Figure 3e). What is more, the photoresponse rejection ratio (R_{250}/R_{280}) can reach as high as $\approx 2 \times 10^3$, as shown in Figure 3f. It was also revealed that the variation in synthetic parameters exerted a great influence on the photoresponse properties. With decrease of the growth temperature, both dark current and photocurrent increased gradually, which gave an enhanced responsivity by several orders of magnitude. However, the response speed and photoresponse rejection ratio inevitably decreased. Such a dependence was understandably related to the varied concentration of defects in NWs grown at different temperatures, which dominated the density and lifetime of carriers. Afterward, $\beta\text{-Ga}_2\text{O}_3$ NBs have been synthesized and utilized as building blocks for DUV photo-detection by using CVD methods.^[67–69] In comparison with an individual NW-based device, the NB detectors exhibited superior performance in terms of lower dark current, larger $I_{\text{light}}/I_{\text{dark}}$ ratio, and higher responsivity. For instance, Zou et al. presented a DUVPD with an ultralow dark current (below the detection limit of 10^{-14} A), an extremely high $I_{\text{light}}/I_{\text{dark}}$ ratio exceeding 10^6 , and fast response speed less than 0.3 s. The responsivity in this work was as high as ≈ 851 A W^{-1} .^[68] In order to further enhance the photoresponse, Tian et al. used In atoms to dope Ga_2O_3 NBs.^[69] It was observed that In-doped devices can achieve higher $I_{\text{light}}/I_{\text{dark}}$ ratio ($\approx 10^3$), responsivity (5.47×10^2 A W^{-1}), EQE ($2.72 \times 10^5\%$) and faster response speed (rise/decay time: 1/0.6 s) than undoped devices. Recently, 2D or quasi-2D $\beta\text{-Ga}_2\text{O}_3$ nanosheets/nanoflakes have been successfully produced by oxidation of 2D GaSe or directly exfoliated from $\beta\text{-Ga}_2\text{O}_3$ bulk crystals.^[70,71] The oxidized nanosheets are polycrystalline with thickness less than 10 nm, while ≈ 400 nm thick exfoliated nanoflakes can maintain the single-crystalline property of the bulk. Photoresponse characterization revealed that detectors made from both nanosheets and nanoflakes were highly sensitive to 254 nm DUV radiation. Specifically, the latter detectors exhibited an ultrahigh responsivity of 1.8×10^5 A W^{-1} , which was the highest value ever reported.^[71] Such excellent responsivity can be explained by the reduced dark current and increased electric field due to modulation of gate voltage. Another possible reason is associated with the advantage resulting from the quasi-2D structure including an increased number of surface trap states that afforded a large photoconductive gain, and shortened carrier transit time.

3.2. MSM Photodetectors

On account of the intrinsic lower dark current and faster response speed, MSM photodetectors based on $\beta\text{-Ga}_2\text{O}_3$ have attracted grand interest and been extensively studied recently.^[74–85] Heretofore, various electrode materials including Ti/Au, Ni/Au, indium zinc oxide (IZO), and graphene have been utilized to form Schottky barrier contacts with $\beta\text{-Ga}_2\text{O}_3$. It is not strange that nearly identical electrode materials can form either Ohmic contact or Schottky contact with $\beta\text{-Ga}_2\text{O}_3$ in different reports considering the fact that the surface states

on $\beta\text{-Ga}_2\text{O}_3$ are crucial to the contact.^[9,86] Taking Ti/Au, for example, Guo et al. found that Ti/Au electrodes can form Ohmic contacts with laser MBE-grown $\beta\text{-Ga}_2\text{O}_3$ films, but this metal–semiconductor structure would become Schottky contact once the films were subject to thermal annealing in oxygen atmosphere.^[74]

To date, $\beta\text{-Ga}_2\text{O}_3$ films suitable for MSM photodetector application are usually prepared through mechanic exfoliation,^[87–89] laser MBE,^[74,81,83,90–92] MOCVD,^[47,75,79] oxidation of GaN films,^[78] thermal evaporation,^[93,94] pulsed laser deposition (PLD),^[80] magnetron sputtering,^[54,95,96] etc. These DUVPDs typically exhibited low dark current in the range of 10^{-13} – 10^{-9} A, large $I_{\text{light}}/I_{\text{dark}}$ ratio with the maximum value exceeding 10^5 , and large photoresponse rejection ratio as high as 10^5 . It has been reported that surface passivation played a pivotal role in determining the photoresponse performance.^[81] For instance, once MSM detectors based on plasma-assisted MBE-grown $\beta\text{-Ga}_2\text{O}_3$ films were passivated with atomic layer deposition-derived Al_2O_3 , the dark current reduced dramatically by tens of times, while the photocurrent under DUV light only suffered from negligible degradation. Similar to the strategies employed in $\beta\text{-Ga}_2\text{O}_3$ photoconductors, optimization in temperature during the growth process and the post thermal annealing have also been adopted for improving the performance of $\beta\text{-Ga}_2\text{O}_3$ MSM photodetectors.^[75,80] For example, Yu et al. observed that $\beta\text{-Ga}_2\text{O}_3$ films prepared by PLD method at higher temperatures (800–1000 °C) possessed single crystalline phase with remarkably reduced vacancies and defects than those grown at lower temperatures.^[80] Due to higher crystal quality and fewer oxygen vacancies, MSM detectors grounded on 800 °C-grown films exhibited reduced dark current by maximum 3 orders of magnitude, and a higher responsivity increasing from 0.359 to 0.903 A W^{-1} , in comparison with devices made from 600 °C-grown films. Annealing $\beta\text{-Ga}_2\text{O}_3$ films prepared by low-pressure MOCVD (LP-MOCVD) in the atmosphere or in nitrogen environment has also led to suppressed dark current and improved photoresponse, while annealing in oxygen environment has yielded an entirely contrary result.^[75]

Wei et al. presented highly transparent $\beta\text{-Ga}_2\text{O}_3$ MSM photodetectors using IZO as electrodes.^[79] Because of the high chemical and thermal stabilities of $\beta\text{-Ga}_2\text{O}_3$, the devices can operate properly under significantly different oxygen concentration in ambient condition, and at working temperatures as high as 700 K. The results indicated excellent reliability and robustness of the devices and great potential of $\beta\text{-Ga}_2\text{O}_3$ DUVPDs for use in harsh environments. Graphene has also been employed as transparent electrodes for $\beta\text{-Ga}_2\text{O}_3$ MSM photodetectors in recent reports.^[97] Kong et al. reported a highly sensitive DUVPD, which was basically composed of multilayer graphene on top side of single-crystalline Sn-doped $\beta\text{-Ga}_2\text{O}_3$ wafer and Cr/Au electrode at back side of the wafer (Figure 4a,b).^[82] Thanks to the asymmetric contacts, the device exhibited obvious rectifying behavior in darkness. Interestingly, it was found that the forward current of the device increased considerably by $\approx 10^3$ when the graphene electrode side was shined with 254 nm DUV illumination, while the current remained almost unchanged to 365 nm radiation (the graphene side with positively applied voltage is defined as forward bias), as illustrated in Figure 4c. The responsivity and specific detectivity attained were as high

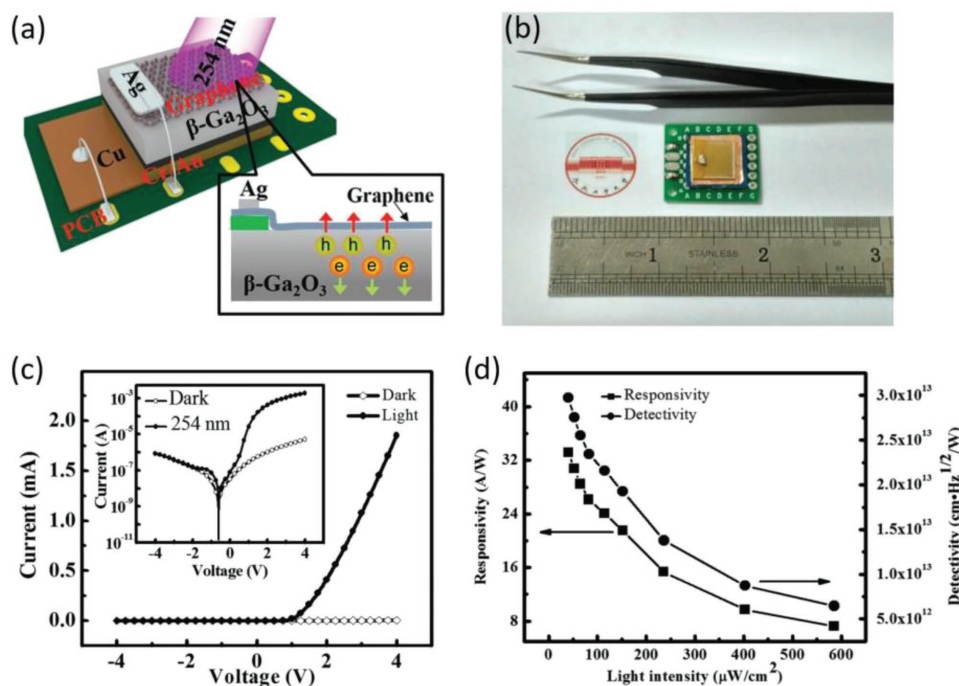


Figure 4. a) Schematic diagram of a graphene/ β -Ga₂O₃/metal MSM photodetector. b) A digital photograph of the device. c) I - V characteristics of the device in dark and under 254 nm light radiation, the inset shows the I - V curves on a logarithmic scale. d) Both responsivity and detectivity of the DUVPD under light illumination with different intensities. Reproduced with permission.^[82] Copyright 2016, Wiley-VCH.

as 39.3 A W^{-1} and 5.92×10^{13} Jones, respectively (Figure 4d). What is more, the devices can operate properly under periodically switched DUV radiation even after one month storage in air condition, suggesting excellent reproducibility and stability of the detectors. Asymmetric graphene electrodes in contact with laser MBE-grown β -Ga₂O₃ films,^[83] or exfoliated single-crystalline β -Ga₂O₃ microflakes^[98] to form MSM photodetectors have also been demonstrated. The devices achieved $I_{\text{light}}/I_{\text{dark}}$ ratio of ≈ 83 and responsivity of 9.66 A W^{-1} , respectively, in the first report. Specifically, the $I_{\text{light}}/I_{\text{dark}}$ ratio, responsivity, photoresponse rejection ratio (R_{254}/R_{365}), and specific detectivity reached as high as 1.18×10^4 , 29.8 A W^{-1} , 9.46×10^3 , and 1.45×10^{12} Jones, respectively, for devices in latter work. These values exceeded those of similar devices with Ni/Au electrodes by 2–4 orders of magnitude, suggesting great potential of using graphene transparent electrodes in solar-blind DUV optoelectronics. The working mechanism of these devices relies on the DUV light modulation of Schottky barrier at graphene/ β -Ga₂O₃ interface. Actually, the Schottky barriers were very sensitive to oxygen in air. In darkness, the oxygen molecules absorbed on Ga₂O₃ surface can capture the free electrons in β -Ga₂O₃, forming negatively charged oxygen ions. Upon DUV illumination, electron-hole pairs were generated in the β -Ga₂O₃, and were then separated by the local built-in electric field at Schottky contact, leading to increased free carrier density. The photogenerated holes in the depletion region will discharge the negatively charged oxygen ions via electron-hole recombination, which reduced the Schottky barrier height and width. Therefore, the current increased considerably upon DUV illumination. After switching off the illumination, the photogenerated electrons will recombine with holes through either

recombination centers or band-to-band annihilation process, recovering the Schottky barrier. More recently, highly integrated MSM β -Ga₂O₃ photodetector arrays of 32×32 , 16×16 , 8×8 , and 4×4 have been reported by Peng et al.^[99] The photodetector array displayed high sensitivity to 254 nm DUV radiation with a high $I_{\text{light}}/I_{\text{dark}}$ ratio exceeding 10^5 , a large responsivity of 0.89 A W^{-1} , and a reasonable DUV/visible rejection ratio (R_{250}/R_{400}) close to 10^3 . In addition, the photoresponse parameters of unit cells from a 4×4 photodetector array were relatively uniform, and the standard deviation of the responsivities was only 12.11%, suggesting great potential of such β -Ga₂O₃ photodetector arrays for DUV imaging applications.

Compared with the crystalline polymorphs, the amorphous Ga₂O₃ thin film usually derived from low-temperature magnetron sputtering or PLD methods has proved to be ideal building block for DUVPD as well.^[100] For instance, Qian et al. developed an ultrahigh-responsivity, rapid-recovery, solar-blind photodetector by using highly nonstoichiometric amorphous gallium oxide that was obtained by a radio frequency (RF) magnetron sputtering approach.^[101] The responsivity is as high as 70.26 A W^{-1} , because of the high internal gain and extrinsic transitions. Besides, the rejection ratio (R_{250}/R_{350}) and specific detectivity can exceed 10^5 and 1.3×10^{14} Jones, respectively, which are highly competitive even compared with other β -Ga₂O₃ film devices. By directly depositing amorphous gallium oxide film on polyethylene naphthalate substrate via a room-temperature RF magnetron sputtering process, Cui et al. recently developed a highly sensitive and flexible MSM DUVPD with a responsivity of 0.19 A W^{-1} .^[102] Interestingly, the as-assembled devices have comparable performance with the rigid ones, and no obvious degradation in performance was found during fatigue and bending measurement.

3.3. Heterojunction Photodiodes

3.3.1. Ga₂O₃ Thin Films

In this part, we will introduce Ga₂O₃/semiconductor hybrid structure, another equally important geometry for DUV detection. Up to now, a variety of semiconductors that have been combined with Ga₂O₃ to form heterojunction photodiodes include GaN,^[103–105] SiC,^[106,107] Nb:SrTiO₃ (NSTO),^[108] Si,^[109–112] ZnO,^[113–118] SnO₂,^[119] diamond,^[120] CuGaSe₂,^[121] and so forth. For example, heterojunctions can be formed by coating β -Ga₂O₃ films on 6H-SiC or GaN substrates through gallium evaporation in oxygen plasma.^[104,106] The as-assembled heterojunction exhibited obvious photovoltaic behaviors under DUV illumination, and the current increased linearly with increasing light intensity. The responsivities reached the maximum values of 0.07–0.18 A W⁻¹ at the wavelength of \approx 225 nm, which decreased rapidly when light wavelength exceeded 280 nm. Moreover, the response speed of these photodiodes was in the order of milliseconds or sub-milliseconds, much faster than the aforementioned photoconductors and MSM photodetectors. Remarkably, the operation of β -Ga₂O₃/GaN photodiodes can be switched between solar-blind and visible-blind modes by simply changing the applied working bias.^[103]

As a matter of fact, the majority of the above devices can only work with bias voltage. To reduce energy consumption, a number of self-powered DUV photodiodes with device

geometry of magnetron-sputtered β -Ga₂O₃ films on NSTO substrates,^[108] laser MBE-grown β -Ga₂O₃ films on Ga-doped ZnO (Ga:ZnO) substrates,^[113] magnetron-sputtered β -Ga₂O₃ films on seed layer-coated Si substrates,^[111] and plasma-enhanced CVD (PECVD)-derived β -Ga₂O₃ films on diamond substrates have been developed.^[120] At zero bias, β -Ga₂O₃/NSTO heterojunctions exhibited relatively faster response speed in the order of tens of milliseconds, however, with much lower responsivity of 2.6 mA W⁻¹.^[108] It was found that when applying a working bias (10 or -10 V), the responsivity values increased significantly to 10.43 or 43.31 A W⁻¹, while the response speed suffered from a severe degradation (several to tens of seconds) (Figure 5a–e). Similar phenomenon has also been perceived in β -Ga₂O₃/Ga:ZnO heterojunctions.^[113] The increased responsivity can probably be related to the internal gain due to the photoconductive effect, while the carrier trapping/releasing process because of the existence of defects like oxygen vacancies is responsible for the slower response speed at an applied bias. In addition, β -Ga₂O₃/Si heterojunctions achieved good DUV photoresponse at zero bias, in terms of a high $I_{\text{light}}/I_{\text{dark}}$ ratio of $>10^3$, a record low dark current of 1.43 pA, fast response speed in milliseconds, with high stability and reproducibility.^[111] At a bias of 5 V, the responsivity was as high as 96.13 A W⁻¹ at 250 nm illumination. Significantly, a prototype device of DUV imaging system has been demonstrated by employing β -Ga₂O₃/diamond photodiode as a sensing pixel.^[120] It was found that the optical pattern of hollow

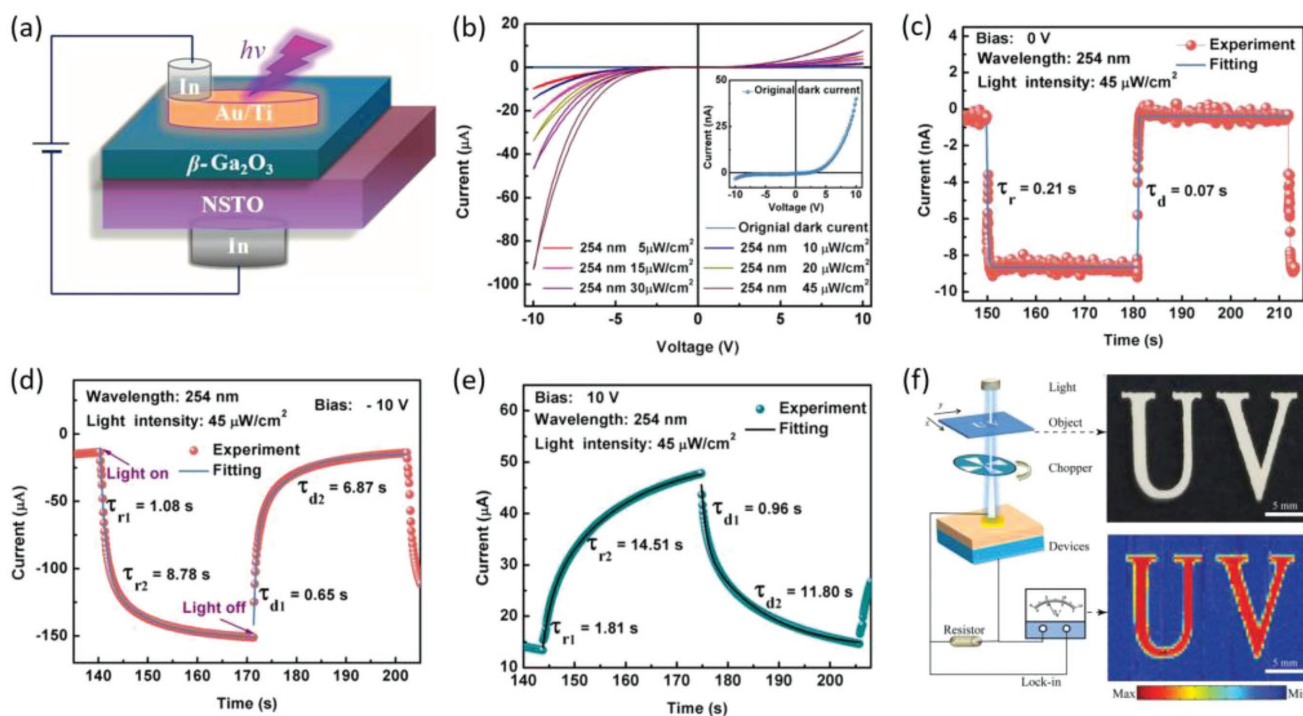


Figure 5. a) Schematic illustration of a β -Ga₂O₃/NSTO heterojunction photodetector. b) I - V curves of the β -Ga₂O₃/NSTO heterojunction photodetector in the dark and under 254 nm light illumination with various light intensities; the inset is the enlarged view of the fresh dark I - V curve. Time-dependent photoresponse of the heterojunction detector illuminated by 254 nm light at a bias of c) 0 V, d) -10 V, and e) 10 V, respectively. Reproduced with permission.^[108] Copyright 2017, American Chemical Society. f) Schematic illustration of the imaging system employing the diamond/ β -Ga₂O₃ heterojunction photodetector as a sensing pixel under 0 V bias (left panel). The image of the object with letters “UV” on a black paper (top right panel). Image obtained from the imaging system (bottom right panel). Reproduced with permission.^[120] Copyright 2018, Royal Society of Chemistry.

letters “UV” can be readily recognized by the sensor and can be presented as an image with sharp boundaries and low background (Figure 5f), suggesting the high fidelity characteristics of the imaging system and further confirming that such heterojunction photodetectors can satisfy the requirement of the imaging system without an external power supply.

By exploring avalanche carrier multiplication effect, avalanche photodiodes (APDs) based on heterojunctions of laser MBE-prepared β -Ga₂O₃ film on Si substrate or cation exchanged-grown β -Ga₂O₃ film on SnO₂ film show superb photoresponse property.^[109,119] At -3 V (reverse bias), a high responsivity of 370 A W⁻¹ was achieved for β -Ga₂O₃/Si APD device, which corresponds to an EQE value exceeding $1.8 \times 10^5\%$.^[109] Although the incident light with photon energy lower than bandgap of β -Ga₂O₃ can excite photocarriers in Si, the effective extraction of photocarriers is suppressed due to the much higher resistance of β -Ga₂O₃ than Si. However, for DUV light which can excite photocarriers in β -Ga₂O₃, the resistance of β -Ga₂O₃ is thus significantly reduced and photocarrier extraction capability is greatly enhanced. This explains the excellent solar-blind DUV detecting property of the β -Ga₂O₃/Si APD device. In another work, the cation exchange growth mechanism reduced the lattice mismatch along the interface between two UWBG semiconductors.^[119] The resultant β -Ga₂O₃/SnO₂ APD showed high selectivity to 254 nm DUV light with excellent photoresponse characteristics with responsivity, EQE, avalanche gain, detectivity, linear dynamic range (LDR), and response speed were 2.3×10^3 A W⁻¹, 4.48×10^6 , 1.7×10^5 , 1.7×10^{15} cm W⁻¹ s⁻¹, 126 dB, and 25 μ s, respectively. The establishment of the avalanche multiplication process can be ascribed to the huge difference between the electron and hole energy barriers of the two UWBG semiconductors. Another

strategy to improve the photoresponse performance was utilizing p-i-n photodiodes.^[110] An et al. found that the dark current of p-Si/n-Ga₂O₃ photodiode can be greatly reduced by 3 orders of magnitude by inserting an intrinsic SiC film that serves as an appropriate electron blocking layer.^[110] Through further diminishing the oxygen vacancies via changing the oxygen pressure during thermal annealing, the photosensitivity was found to increase from $3.4 \times 10^4\%$ to $5.4 \times 10^5\%$.

3.3.2. Ga₂O₃ Microwires

Zhao et al. presented the fabrication of a ZnO/Ga₂O₃ core/shell heterostructure microwire for self-powered solar-blind DUVPD application (Figure 6a).^[115] Figure 6b,c depicts a typical photograph of the core/shell microwire and a high-resolution transmission electron microscopy (HRTEM) image of the interface between the core and shell portions. The heterostructure showed remarkable sensitivity to DUV illumination with a sharp cutoff wavelength at ≈ 266 nm (Figure 6d). The responsivity and DUV/visible rejection ratio (R_{251}/R_{400}) at zero bias were 9.7 mA W⁻¹ and 6.9×10^2 , respectively, which could be significantly enhanced to 11.1 A W⁻¹ and 1.2×10^3 under an applied bias of -2 V, respectively (Figure 6e,f). The device also has a fast response speed with rise time less than 100 μ s and decay time of 900 μ s. Furthermore, such heterostructures can also operate as APD devices exploring carrier multiplication effect.^[114] Under reverse bias, the dark current can retain an approximately linear increase ($\approx 10^{-11}$ A) from 0.1 to 4.3 V, while it increased exponentially (10^{-10} – 10^{-7} A) from 4.3 to 10 V, indicating a breakdown voltage of ≈ 4.3 V for the device at room temperature. The responsivity reached 1.3×10^3 A W⁻¹ at -6 V, which further increased

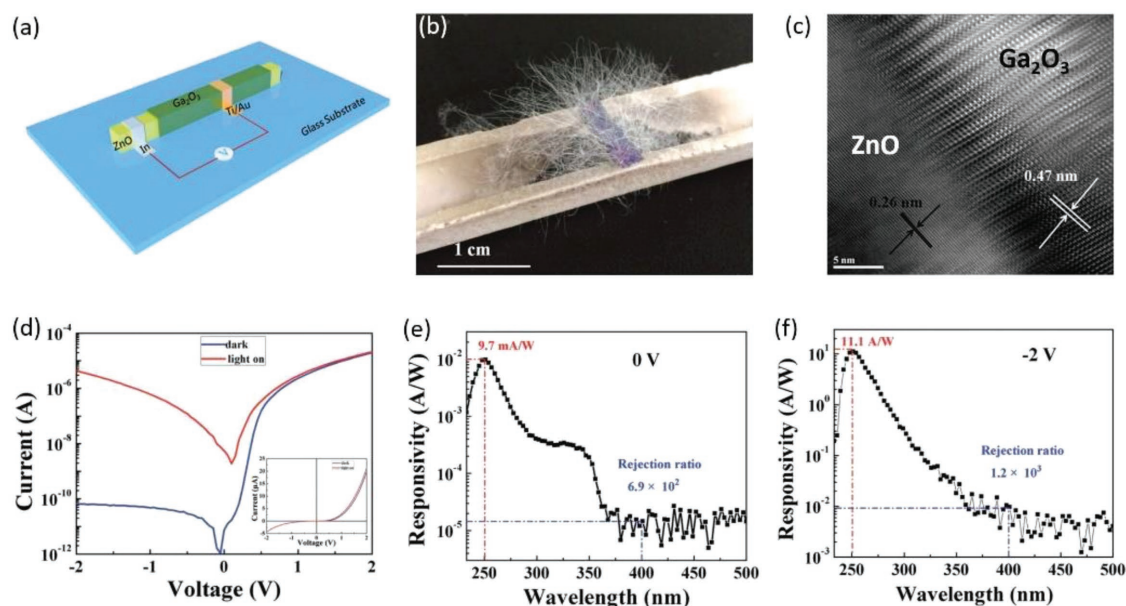


Figure 6. a) Schematic diagram of a ZnO/ β -Ga₂O₃ core/shell microwire heterojunction DUVPD. b) A photograph of the as-synthesized ZnO/ β -Ga₂O₃ core/shell microwires. c) A HRTEM image of the interface between the core and shell portions. d) I - V characteristics of the photodetector under dark (blue line) and illumination with 254 nm light with a power density of 1.67 mW cm⁻² (red line). Spectral responsivity of the device at a bias of e) 0 V and f) -2 V, respectively. Reproduced with permission.^[115] Copyright 2017, Wiley-VCH.

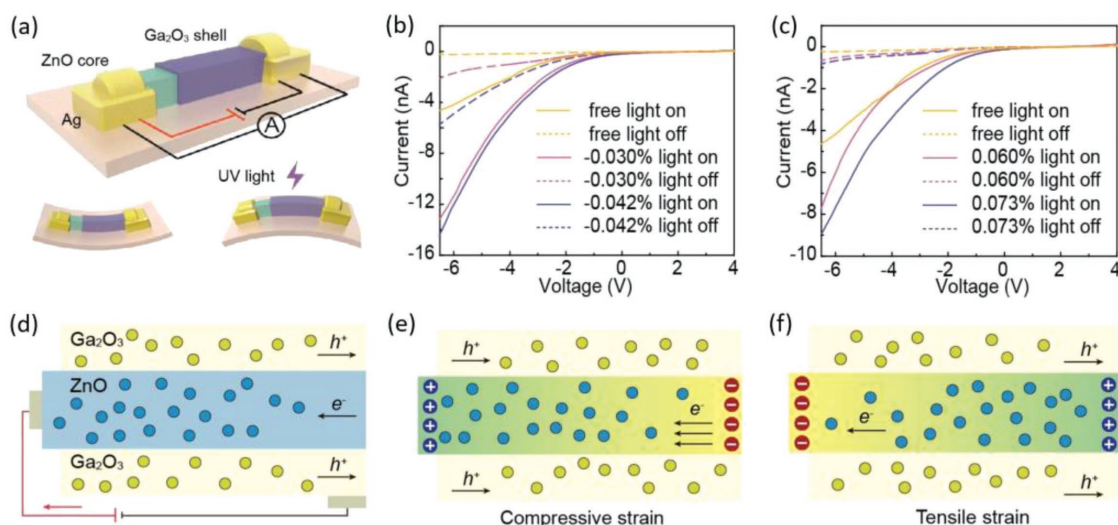


Figure 7. a) Structure design of the ZnO/ β -Ga₂O₃ core/shell microwire photodetector, showing the device under compressive and tensile strains, respectively. *I*-*V* characteristics of the photodetector under b) compressive and c) tensile strains upon 268 nm radiation, respectively. d) Schematic diagram exhibiting electron-hole pair separation and transfer in the ZnO/ β -Ga₂O₃ heterostructure under 268 nm light illumination. The proposed model of the device under strains, that is, electron transport is modulated in ZnO core by the piezopotential and the color indicates the piezopotential distribution in the ZnO core under e) compressive and f) tensile strains. Reproduced with permission.^[116] Copyright 2018, Wiley-VCH.

to $5.18 \times 10^3 \text{ A W}^{-1}$ at -10 V . Furthermore, other photoresponse parameters including $I_{\text{light}}/I_{\text{dark}}$ ratio, specific detectivity, response speed, DUV/visible rejection ratio (R_{251}/R_{400}), and LDR (at -5 V) are $\approx 10^6$, 9.91×10^{14} Jones, $20/42 \mu\text{s}$, 5×10^3 , and 119.3 dB , respectively, at reverse bias of 6 V . Further performance improvement has been realized by exploiting the piezophototronic effect of the ZnO/Ga₂O₃ core/shell heterostructure microwire (Figure 7a).^[116] Under static strain of -0.042% , the DUV current response can be enhanced by ≈ 3 times (Figure 7b), which was attributed to the modulation of the energy band diagrams and charge carriers in the heterojunction area upon straining. However, it was observed that photoresponse under tensile strain did not increase as obviously as that under compressive strain (Figure 7c). Such finding is reasonable in that under compressive strain, the introduced piezopotential strengthened the electron transport in ZnO core, enhancing the photocurrent obviously, whereas the opposite piezopotential was introduced under tensile strain, bringing about limited enhanced effect (Figure 7d-f).

Apart from the above work, direct combination of Ga₂O₃ with GaN can lead to sensitive solar-blind DUVPDs as well.^[122-124] For instance, Jaiswal et al. recently tried to deposit Ga₂O₃ on GaN epilayers using the microwave radiation technique. The heterojunction thin film-based device with Ni/Au contact displayed a peak spectral response at 230 nm and a good DUV/visible rejection ratio (R_{230}/R_{400}) of 10^3 , which is expected to open up new opportunities for integrating solar-blind DUVPDs toward next generation high-performance optoelectronics.^[123] In order to improve photoresponse of the Ga₂O₃/GaN photodetector, a surface plasmon resonance strategy using gold nanoparticles was developed.^[125] It was revealed that upon covering of Au nanoparticles, the reverse leakage current decreased by more than 100 times. Meanwhile, the photoresponse rejection ratio (R_{250}/R_{360}) was increased by nearly 95-fold at 1 V applied bias.

3.4. Schottky Photodiodes

The preliminary β -Ga₂O₃ solar-blind DUV Schottky photodiode was fabricated by directly depositing Ni/Au electrode, followed by thermally annealing at $1100 \text{ }^\circ\text{C}$ in oxygen ambient to reduce oxygen vacancies and decrease the carrier concentration near the surface.^[126] The diodes showed a high rectification ratio exceeding 10^6 in darkness, and obvious DUV response at reverse bias with responsivities of $2.6\text{--}8.7 \text{ A W}^{-1}$ at the wavelengths of $200\text{--}260 \text{ nm}$. These relatively high values can be associated with the carrier multiplication process occurring at the highly resistive surface region that was subject to a very high electric field at a reverse bias. Postannealing has also proved to be effective on improving the electrical and optoelectrical properties of β -Ga₂O₃-based photodiodes. Suzuki et al. found that annealing at temperature above $200 \text{ }^\circ\text{C}$ can improve the ideality factor of the diodes to near unity, while keeping the reverse leakage current almost unaffected.^[127] Furthermore, annealing at $400 \text{ }^\circ\text{C}$ gave rise to a dramatic enhancement in responsivity by a factor of more than 10^2 with the maximum value exceeding 10^3 A W^{-1} in the region below 260 nm , and a high photoresponse rejection ratio (R_{240}/R_{350}) of $\approx 10^6$. In another study, the same group observed that inserting a sol-gel-derived high resistivity β -Ga₂O₃ cap layer in an Au/ β -Ga₂O₃ Schottky photodiode can lead to solar-blind photoresponse in both forward and reverse biases, which was in contrast to conventional Schottky photodiodes.^[128] The odd forward photoresponse can be ascribed to the photoconductive effect in the cap layer. In darkness, because of the high resistivity, the cap layer supported a large fraction of the applied forward voltage. Therefore, the voltage applied to the i-n junction barrier between the cap layer (i-region) and β -Ga₂O₃ substrate (n-region) was small, leading to a slight change of current with applied voltage unless the voltage was high enough to

surmount the junction barrier. However, upon DUV illumination, the resistance of the cap layer decreased drastically due to the photogenerated carriers, and thus considerable forward bias was applied to the *i-n* junction. Consequently, the junction barrier decreased at a lower forward bias and the electron injection took place from the substrate to the cap layer. As the voltage further increased, the barrier disappeared, and a large number of electrons were then injected into the cap layer, producing the large forward current.

Recently, by a simple partial oxidation process, Chen et al. developed a self-powered solar-blind DUV photodiode based on Au- β -Ga₂O₃ NW array Schottky junction.^[129] The device exhibited a good rectifying behavior with the dark current of ≈ 10 pA at a large bias of -30 V. Under zero bias, the responsivity turned out to be only 0.01 mA W⁻¹, which could be enhanced to 2.9 mA W⁻¹ by increasing the operation voltage to -50 V. In addition, the detectors had a rapid response speed of rise/decay time of $1/64$ μ s. Such a fast response speed along with the excellent stability and good reproducibility renders the device potentially suitable for high-speed DUV optoelectronic application.

In summary, photoconductors based on β -Ga₂O₃ thin films show relatively good DUV sensitivity, with $I_{\text{light}}/I_{\text{dark}}$ ratio ranging from 10^3 to 10^6 , peak responsivities as high as 10^4 A W⁻¹, and photoresponse rejection ratio typically in the order of 10^3 – 10^4 . Performance improvement has been realized via some strategies including optimizing temperature during material preparation, high-temperature post thermal annealing, optimization of contact electrodes, introducing a buffer layer, annealing growing sapphire substrate, rational doping with impurity, surface passivation, exploring carrier multiplications process, etc. Thanks to the superior advantages, MSM photoconductors made from β -Ga₂O₃ nanostructures exhibit even higher peak responsivities exceeding 10^5 A W⁻¹, and ultralow dark currents below 10^{-14} A. In addition, β -Ga₂O₃ thin film-based MSM photodetectors usually have lower dark current in the range of 10^{-13} – 10^{-9} A, comparable $I_{\text{light}}/I_{\text{dark}}$ ratio exceeding 10^5 , and higher photoresponse rejection ratio as high as 10^5 . In particular, MSM photodetectors with graphene transparent electrodes possess specific detectivity as high as 10^{13} Jones, which is several orders of magnitude larger than similar devices with metal electrode and suggests the great potential for weak DUV detection. On the other hand, heterojunction or Schottky junction photodiodes based on β -Ga₂O₃ thin films or micro-/nanostructures usually display faster response speed in the order of milliseconds or sub-milliseconds, however, with much lower peak responsivities (the maximum value is tens of A W⁻¹). These photodiodes can work at zero bias voltage as self-powered photodetectors, exhibiting relatively low responsivities. Further optimization in device performance is achievable through some avenues like exploring avalanche carrier multiplication effect to form APDs, constructing devices with geometry of *p-i-n* photodiode, or exploiting the pizeophototronic effect. Nevertheless, challenges still remain. For example, the application of Ga₂O₃ to *p-n* (*p-i-n*) and Schottky junction photodiodes is largely hindered by the difficulty pertaining to realizing *p*-type doping of Ga₂O₃ due to the high activation energy of acceptors and strong localization of holes.

4. Mg_xZn_{1-x}O

The cutoff wavelength of photodetectors based on pure ZnO lies in the UV region exceeding 300 nm, making them unsuitable for DUV light detection.^[6,7,130,131] However, many studies have shown that doping ZnO is a feasible way of tailoring its bandgap.^[132] So far, the bandgap of ZnO has been successfully changed by alloying it with some group II and III elements such as Be, Mg, Ca, Cd.^[133,134] Among these ZnO-based ternary metal oxides, Mg_xZn_{1-x}O is the most widely studied one due to the comparable radius of Mg²⁺ ion (0.57 Å) with Zn²⁺ (0.60 Å) ion. More importantly, the incorporation of high bandgap of MgO (≈ 7.5 eV) can extend the bandgap to DUV wavelength region.^[135] On this account, the tunable bandgap from 3.37 to 7.5 eV, along with the excellent optoelectronic characteristics inherited from ZnO renders Mg_xZn_{1-x}O highly attractive for solar-blind DUV photodetection. Nevertheless, doping also changes lattice properties of the compound and phase separation appears with the increase of Mg content. In addition, the crystallinity of the compound is inevitably affected by the solubility of MgO in Mg_xZn_{1-x}O, which depends strongly on the preparation process and growth conditions. The above issues thus constitute the main challenge for the application of Mg_xZn_{1-x}O in solar-blind DUV photodetection. In this section, we will discuss the recent progress in Mg_xZn_{1-x}O compound-based solar-blind DUVPDs.

4.1. Photoconductors

Mg_xZn_{1-x}O alloy thin films with varied Mg contents have been successfully prepared with various techniques including PLD,^[136–138] MOCVD,^[139,140] magnetron sputtering,^[141–145] plasma-assisted MBE,^[146,147] etc. During the growing period, sapphire or quartz wafer are often employed as growing substrates. However, in some special cases, Si can also be used as growing substrate, on which a thin SrTiO₃ buffer layer was coated to overcome large lattice and thermal expansion mismatch between Si and Mg_xZn_{1-x}O.^[136] The as-synthesized films had good crystalline quality and showed peak photoresponse at ≈ 225 nm. In addition, some groups reported the usage of MgO or SiO₂/Si substrates to prepare Mg_xZn_{1-x}O films as well.^[140,144] Photodetectors based on MOCVD-grown Mg_{0.52}Zn_{0.48}O films on MgO substrates exhibited peak response at ≈ 238 nm and cutoff wavelength located at ≈ 253 nm.^[140] The responsivity at 15 V bias reached 129 mA W⁻¹, and the DUV/visible rejection ratio (R_{240}/R_{400}) was as high as 10^4 . However, the presence of native defects such as oxygen vacancies at Au/Mg_{0.52}Zn_{0.48}O interface degraded the barrier effect, which led to relatively large dark current and the undesirable visible response at wavelength region exceeding 450 nm.

The bandgap of Mg_xZn_{1-x}O films can be readily tuned by changing the atomic ratio of Mg/Zn during preparation process. According to a previous study, Mg_xZn_{1-x}O films prepared on *c*-plane sapphire with Mg content <37% has a hexagonal wurtzite crystal structure (*h*-Mg_xZn_{1-x}O), while pure cubic-phase Mg_xZn_{1-x}O (*c*-Mg_xZn_{1-x}O) appeared when Mg content exceeded $\approx 62\%$.^[136] With Mg content between 37–62%,

Mg_xZn_{1-x}O films usually had a mixed phase with undefined bandgaps. Ju et al. have obtained Mg_xZn_{1-x}O films with different Mg contents by changing the molar ratio of Zn and Mg precursors during MOCVD process.^[139] With Mg content decreasing from 0.70 to 0.50, the absorption cutoff edge of the Mg_xZn_{1-x}O films shifted gradually from 220 to 260 nm, which corresponded to the change of bandgap from ≈5.64 to ≈4.77 eV (Figure 8a,b). What is more, no multiabsorption edge was observed for all films, confirming no phase separation in these samples. In another study, by adjusting the composition of the Mg_xZn_{1-x}O ceramics as precursor targets, Mg_xZn_{1-x}O films with Mg content from 0.70 to 0 were successfully prepared via magnetron sputtering.^[141] Similar tendency of gradually

enlarged bandgap with increasing Mg content has also been observed. However, for *x* value of 0.5 and 0.55, the films had obvious double absorption edges, suggesting the appearance of phase separation. The exact reason for the different findings in the two works was not clear, but it might be related to the fact that MOCVD was a nonequilibrium growth technique, and at relatively low growth temperature, it is kinetics, rather than thermodynamics that dominates the growth process. That means most radicals did not have enough time to reach their energy-minimum sites, and thus were unable to form single-phased Mg_xZn_{1-x}O films. It has also been reported that the absorption cutoff edges of Mg_xZn_{1-x}O films shifted to long wavelengths after thermal annealing treatment, and the shift

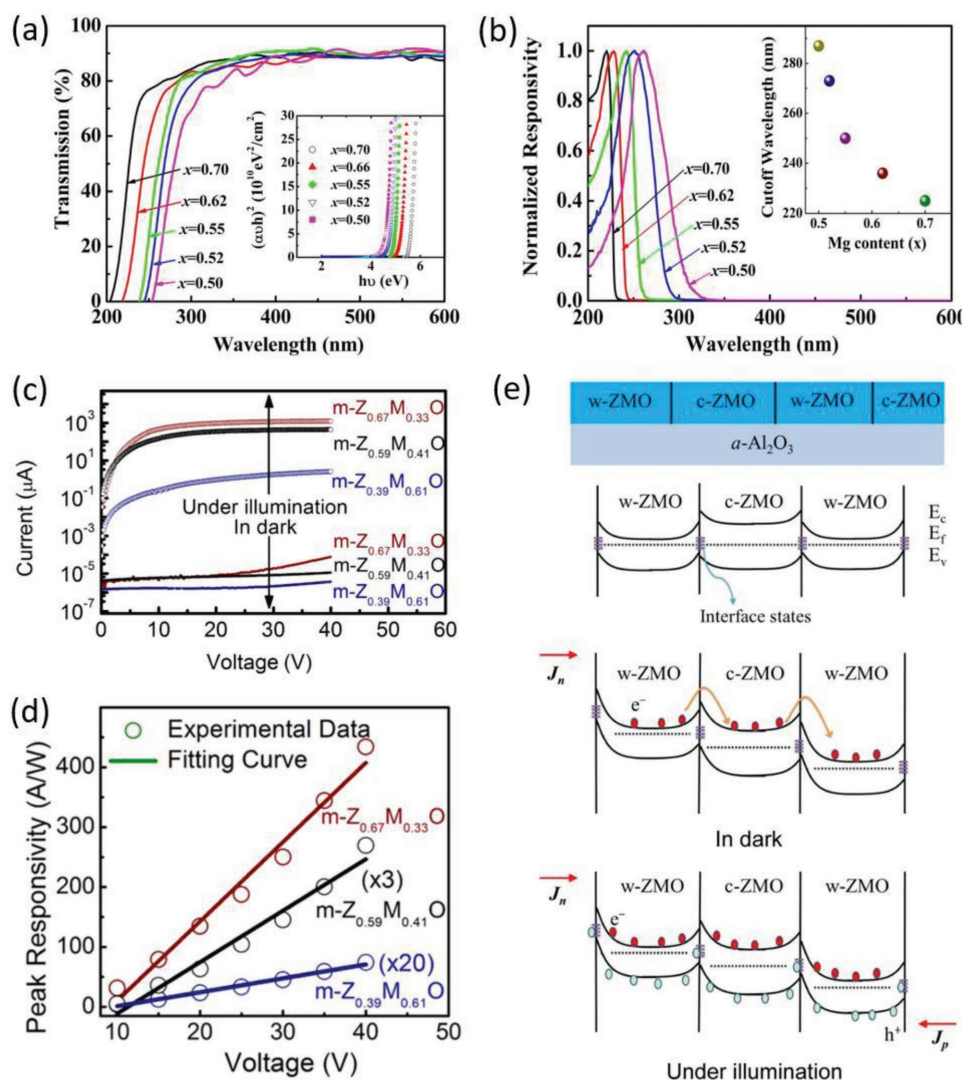


Figure 8. a) Transmission spectra of Mg_xZn_{1-x}O thin films (*x* = 0.50, 0.52, 0.55, 0.62, and 0.70). The inset is a plot of $(\alpha hv)^2$ versus $h\nu$ that gives the bandgaps of these films. b) Normalized response spectra of a Mg_xZn_{1-x}O photoconductor with *x* = 0.50, 0.52, 0.55, 0.62, and 0.70. The inset shows the cutoff wavelength of the photodetector as a function of Mg content. Reproduced with permission.^[139] Copyright 2008, American Institute of Physics Publishing. c) *I*–*V* characteristics of the m-Zn_{0.67}Mg_{0.33}O, m-Zn_{0.59}Mg_{0.41}O, and m-Zn_{0.39}Mg_{0.61}O photodetectors in a dark condition and under DUV illumination. d) Peak responsivity of the m-Zn_{0.67}Mg_{0.33}O, m-Zn_{0.59}Mg_{0.41}O, and m-Zn_{0.39}Mg_{0.61}O photodetectors as a function of bias voltage. e) Energy band diagram and carrier transport process of m-ZMO photodetector at different conditions: at thermal equilibrium (top panel), under bias in dark (middle panel), and under bias with UV illumination (bottom panel). Reproduced with permission.^[147] Copyright 2015, American Chemical Society.

was more obvious in films with higher Mg content.^[143] The effect could be ascribed to the diffusion of Zn atoms gathering at the film surface during the thermal treatment process, which led to the absorption of DUV light occurring mainly at the film surface. Photodetectors based on annealed wurtzite $\text{Mg}_{0.445}\text{Zn}_{0.555}\text{O}$ and cubic $\text{Mg}_{0.728}\text{Zn}_{0.272}\text{O}$ films showed peak responsivities of 17 mA W^{-1} at 275 nm and 0.53 mA W^{-1} at 250 nm , respectively.

Phase separation in $\text{Mg}_x\text{Zn}_{1-x}\text{O}$ films usually resulted in an extra response band, in addition to the main response peak. For example, Jiang et al. observed the appearance of a shoulder in the response spectrum at $\approx 265 \text{ nm}$ besides the dominant peak at $\approx 225 \text{ nm}$ for photodetectors based on magnetron sputtering-grown cubic $\text{Mg}_{0.70}\text{Zn}_{0.30}\text{O}$ films accompanied by a small amount of hexagonal phases.^[142] However, due to the higher Mg content in $\text{h-Mg}_x\text{Zn}_{1-x}\text{O}$ and small lattice mismatch of both ZnO and MgO with *a*-face sapphire, photodetectors made from mixed-phase $\text{Mg}_x\text{Zn}_{1-x}\text{O}$ films prepared on *a*-face sapphire substrates can also show only one response peak.^[146,147] As an example, Fan et al. have prepared mixed-phased $\text{Mg}_x\text{Zn}_{1-x}\text{O}$ films on *a*-face sapphire substrates via plasma-assisted MBE technique and systematically studied the Mg content-dependent photoresponse properties.^[147] They found that at a bias of 40 V , with *x* value increasing from 0.33 to 0.41 and 0.61 , the photodetector witnessed a gradual decrease in dark current from 78 , 11 , and 4 pA , respectively (Figure 8c). In addition, the corresponding peak responsivities also decreased from 434 to 89.8 and 3.7 A W^{-1} (Figure 8d), while the specific detectivity changed from 7.9×10^{13} to 3.5×10^{13} and 2.26×10^{12} Jones, respectively. The authors proposed an operation mechanism to interpret the low dark current and high responsivities achieved in this work. As shown in Figure 8e, *c*- and *h-Mg}_x\text{Zn}_{1-x}\text{O} were grown uniformly and dispersedly on the surface of the sapphire substrate. Therefore, the low dark current could be attributed to the inherently high resistance of *c-Mg}_x\text{Zn}_{1-x}\text{O}, and the presence of large amount of heterojunctions between *c*- and *h-Mg}_x\text{Zn}_{1-x}\text{O}. Electrons could be trapped at interfaces of these heterojunctions, which induced potential barriers that can impede the flow of electrons under an applied bias. On the other hand, the high responsivities arose from the internal gain due to the prolonged lifetime of photogenerated holes. Upon DUV illumination, electron-hole pairs were excited and partial photogenerated holes were trapped during the transport process at *c/h-Mg}_x\text{Zn}_{1-x}\text{O} interfaces or by interface defects and deep defects, prolonging their lifetime. What is more, devices based on these mixed-phase $\text{Mg}_x\text{Zn}_{1-x}\text{O}$ films also exhibited fast response speed with decay times of 37 , 30 , and 0.7 ms , respectively.****

In addition to thin films, photodetectors based on $\text{Mg}_x\text{Zn}_{1-x}\text{O}$ nanostructures have also been realized.^[148] By using a chemical solution method, Wu et al. successfully grew vertical $\text{Mg}_x\text{Zn}_{1-x}\text{O}$ nanorod arrays with good uniformity on glass substrates. They found that aluminum-doped zinc oxide (AlZnO) can form good Ohmic contacts with $\text{Mg}_x\text{Zn}_{1-x}\text{O}$ nanorod array film, due to the high carrier density resulting from the existence of defect states including oxygen vacancies and zinc interstitials. The photodetector assembled from the $\text{Mg}_x\text{Zn}_{1-x}\text{O}$ nanorod array exhibited a decent responsivity and DUV/visible rejection ratio (R_{260}/R_{360}) of 2.01 A W^{-1} and 6.24×10^2 , respectively.

4.2. MSM Photodetectors

As a supplement to photoconductors, MSM photodetectors based on $\text{Mg}_x\text{Zn}_{1-x}\text{O}$ films have also received wide research interest.^[149–159] To overcome phase separation in $\text{Mg}_x\text{Zn}_{1-x}\text{O}$ films with high Mg content, some strategies have been developed such as using a ZnO buffer layer during MBE growth or adopting relatively high substrate temperature and low growth rate during magnetron sputtering.^[149,150] MSM photodetectors made from single-phase $\text{h-Mg}_{0.46}\text{Zn}_{0.54}\text{O}$ films showed peak responsivity of 31.1 A W^{-1} at 70 V bias with a cutoff wavelength of 280 nm and an internal gain of 148 .^[150] Such a large internal gain was attributed to the trapping of photogenerated holes at deep energy levels, as evidenced by the deep-level transient spectral measurement. Furthermore, by employing a relatively low growth temperature and oxygen-rich conditions during MOCVD growth process or using lattice matched ZnO substrates as growth substrates during reactive magnetron cosputtering, single-crystalline $\text{Mg}_x\text{Zn}_{1-x}\text{O}$ films were successfully prepared.^[153,154] The corresponding MSM photodetectors exhibited the maximum responsivity of 396 mA W^{-1} upon 246 nm DUV illumination, and a low dark current density of $1.5 \times 10^{-11} \text{ A cm}^{-2}$, at 10 V bias.^[153] When using ZnO substrates, the response from ZnO could be suppressed by increasing thickness of the $\text{Mg}_x\text{Zn}_{1-x}\text{O}$ films.^[154] Devices with $2 \text{ }\mu\text{m}$ thick films showed responsivity of 304 mA W^{-1} at 260 nm , and photoresponse rejection ratio (R_{260}/R_{365}) exceeding 5×10^2 , at a bias of 10 V . Interestingly, when cubic MgO films were used as growing substrates, the surface roughness of MOCVD-grown $\text{Mg}_{0.58}\text{Zn}_{0.42}\text{O}$ films can be reduced dramatically from 38 to 1.6 nm .^[155] However, due to the smoother surface with fewer defects and reduced absorption probability for sub-bandgap light, DUVPDs showed lower sub-bandgap photoresponse than the ones made from films with rougher surface. In addition, the devices also exhibited low dark current of 0.16 pA at 15 V , thanks to the high crystal quality. The maximum responsivity was 15.8 mA W^{-1} , and the DUV/visible rejection ratio (R_{240}/R_{400}) was as high as 10^4 .

The performance of $\text{Mg}_x\text{Zn}_{1-x}\text{O}$ -based DUVPDs can be further improved by reasonable design of electrode structures or doping of $\text{Mg}_x\text{Zn}_{1-x}\text{O}$.^[156–158] Wang et al. observed that compared with the DUV devices that used conventional electrode, MSM photodetectors utilizing semicircular and triangular electrodes displayed a 20.5% and 100% increase in photocurrent, respectively.^[156] Furthermore, by using asymmetric Schottky barrier and electrode area, the dark current of MSM photodetectors can be reduced by 20 times and 1.3 times, respectively, without a noticeable loss in photocurrent.^[158] The *n*-type conduction of $\text{Mg}_x\text{Zn}_{1-x}\text{O}$ films can be overwhelmingly improved by 2 orders of magnitude through employing triethylgallium as the dopant source during MOCVD growth process.^[157] In sharp contrast with undoped samples, the responsivity of MSM photodetectors made from Ga-doped films increased by ≈ 50 times from ≈ 1 to $\approx 50 \text{ mA W}^{-1}$ under 265 nm illumination at 10 V bias. On the strength of theoretical simulation, such improvement could be ascribed to higher electrical field intensity in the effective layer of Ga-doped devices resulting from the narrower depletion region under the sample applied bias that could facilitate more efficient separation of carriers.

4.3. Hetero-/Homojunction and Schottky Photodiodes

DUV photodiodes rooted in $Mg_xZn_{1-x}O/Si$ heterojunctions have been successfully fabricated by depositing high-quality $Mg_xZn_{1-x}O$ films on p-type Si substrates, on whose surface a thin BeO layer was coated to provide an excellent template for high-Mg-content $Mg_xZn_{1-x}O$ growth.^[160] The heterojunctions had a large rectification ratio of ≈ 300 in darkness and peak responsivities of $\approx 11 \text{ mA W}^{-1}$ at 240–275 nm. Due to the efficient block of photogenerated holes in Si by the large valance band offset, no visible photoresponse was observed, which contributed to a sharp cutoff wavelength at $\approx 280 \text{ nm}$. Recently, through depositing the vertically aligned dense doped polyaniline (PANI) on $Mg_xZn_{1-x}O$ films, Chen et al. realized a self-powered DUV photodiode based on the organic/inorganic hybrid p–n heterojunctions (Figure 9a).^[161] Upon a relatively weak 250 nm DUV illumination ($130 \mu\text{W cm}^{-2}$), the photodetectors achieved a high $I_{\text{light}}/I_{\text{dark}}$ ratio of $\approx 10^4$, giving rise to a maximum responsivity of $160 \mu\text{A W}^{-1}$, at 0 V bias, as depicted in the Figure 9b,c. What is more, the DUV/visible rejection ratio (R_{250}/R_{400}) can reach as high as $\approx 10^4$ (Figure 9d). Even at a bias of -1 V , the device still possessed a low dark current of 0.44 pA and a decent specific detectivity of 1.5×10^{11} Jones. These results suggested that such self-powered photodiodes signified great potential for energy-efficient weak signal detection in solar-blind DUV region. By doping $Mg_xZn_{1-x}O$ with Be atoms, it is possible to achieve $Mg_xBe_yZn_{1-x-y}O$ films on p-Si substrate. It was observed that inserting an Al-doped ZnO interfacial contact layer can remarkably improve the peak responsivity from 0.003 to 0.11 A W^{-1}

at 0 V bias, which accords with a high EQE value of 53% at 270 nm.^[162] Such an improvement was likely to happen due to the significantly enhanced carrier collection efficiency. Through changing the stoichiometry spatial gradient, novel DUV photodiodes on account of graded-bandgap n- $Mg_xZn_{1-x}O/i\text{-MgO/p-Si}$ heterojunctions were successfully constructed, another example was schematically shown in Figure 10a.^[163] The considerable spatial gradient of the conduction band edge can supply a quasi-electric force exerted on the electrons, which promoted efficient separation of photogenerated electron–hole pairs in $Mg_xZn_{1-x}O$ layer (Figure 10b). The quasielectric fields also impelled the generation of multiple carriers through impact ionization under ultralow threshold bias voltage. As a consequence, the detectors achieved good DUV response performance in terms of a high peak responsivity approaching 1200 mA W^{-1} with an acute cutoff wavelength at $\approx 280 \text{ nm}$, and DUV/visible rejection ratio (R_{240}/R_{600}) of $\approx 10^2$, at -6 V bias (Figure 10c).

DUV photodiodes composed of $Mg_xZn_{1-x}O$ Schottky junctions have also been reported.^[164] $Mg_xZn_{1-x}O$ films grown via plasma-assisted MBE on Sn-doped $\beta\text{-Ga}_2\text{O}_3$ substrates, and 7 nm Pt semitransparent electrode was chosen as Schottky barrier contact. It was observed that $Mg_xZn_{1-x}O$ grown on an MgO buffer layer possessed a rocksalt lattice structure, while the film without buffer layer entertained a mixed phase of rocksalt and wurtzite lattice structures. Photoresponse analysis revealed that devices made from rocksalt $Mg_xZn_{1-x}O$ can present solar-blind response characteristic with peak responsivity of $0.1 \mu\text{A W}^{-1}$ at 0 V bias, whereas the devices based on mixed-phase $Mg_xZn_{1-x}O$ was susceptible to incident illumination with wavelength as long as $\approx 370 \text{ nm}$.

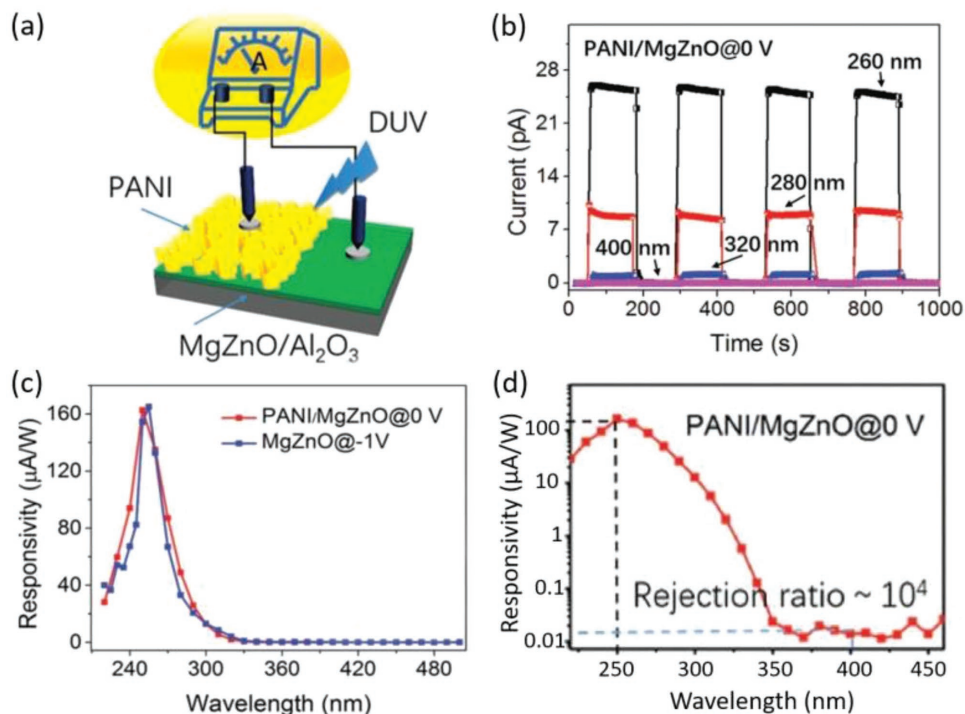


Figure 9. a) Schematic diagram of a PANI/MgZnO heterojunction DUVPD operating without bias voltage. b) Time-dependent photoresponse of the heterojunction photodetector upon illuminations with different wavelengths. c) Spectral response of the PANI/MgZnO photodetector at 0 V bias along with a reference MgZnO photodetector at -1 V bias. d) Spectral response of PANI/MgZnO photodiode in logarithmic scale. Reproduced with permission.^[161] Copyright 2016, Wiley-VCH.

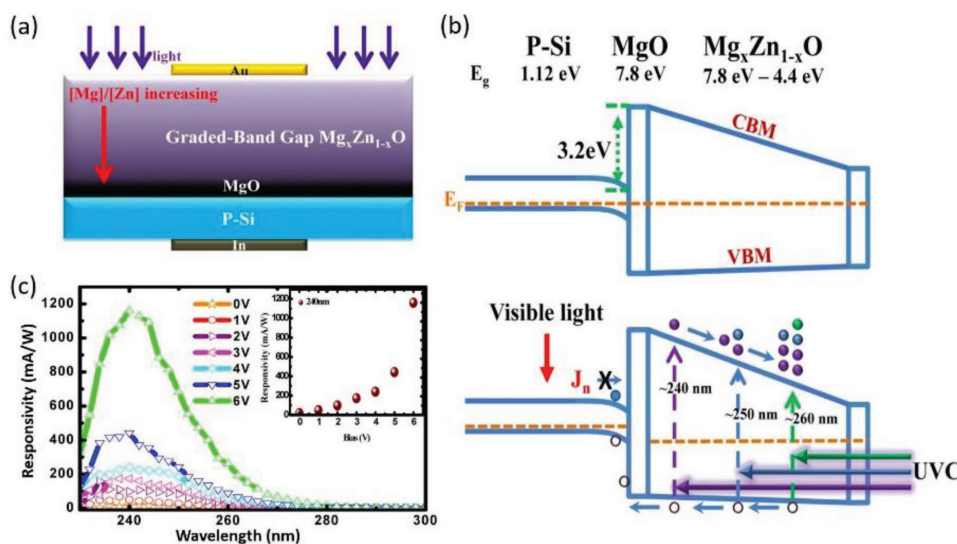


Figure 10. a) Schematic diagram of a DUV photodiode based on the graded-bandgap n-Mg_xZn_{1-x}O/i-MgO/p-Si heterojunction. b) Schematic diagram showing the band alignment of the heterojunction under equilibrium condition (top panel) and under illumination (bottom panel) at reverse bias. c) Spectral responsivity of the photodiode under different reverse bias voltages. Inset shows the responsivity at 240 nm illumination under different reverse bias voltages. Reproduced with permission.^[163] Copyright 2015, Optical Society Publishing.

In conclusion, photoconductors in view of Mg_xZn_{1-x}O thin films usually show summit responsivities ranging from 0.53 mA W⁻¹ to 434 A W⁻¹, while Mg_xZn_{1-x}O thin film-based MSM photodetectors exhibit peak responsivities in the order of 1 mA W⁻¹ to 31.1 A W⁻¹, both of which are much lower than resembling devices made from β-Ga₂O₃ thin films. The photoresponse rejection ratio can reach 10²–10⁴. Moreover, tuning on the atomic ratio of Mg/Zn during material preparation process affords additional degree of freedom to regulate the bandgap, and thus increasing efficiency of the DUV photoresponse properties of the detectors. Optimization of device performance is feasible by rational design of electrode architectures, and doping of Mg_xZn_{1-x}O thin films. On the other hand, heterojunction and Schottky photodiodes made of Mg_xZn_{1-x}O thin films show much lower responsivities in the order of 10⁻⁷ to 1 A W⁻¹, and comparable photoresponse rejection ratio of 10²–10⁴. As is known to all, introducing an interfacial contact layer to the significantly enhancement of carrier collection efficiency has proved to be an efficient approach for improving performance of these devices. However, there still remains some challenges. One critical issue pertains to the extra response band as well as degradation in DUV light detection performance resulting from possible phase separation in Mg_xZn_{1-x}O alloys with moderate Mg content. Another challenge is realizing high-quality p–n (p–i–n) and Schottky junction photodiodes due to the difficulty in achieving effective n- and p-type doping of Mg_xZn_{1-x}O.

5. III-Nitride Compounds

III-nitride compounds refer to materials made of the group III elements (essentially B, Al, Ga, In) and the group V element, N.^[165,166] Typically, they are immediate bandgap semiconductors with values varying from 0.7 eV for InN, 3.4 eV for GaN, 4.5–6.4 eV for BN, to 6.2 eV for AlN.^[165,167] By alloying

these compounds, ternary III-nitride semiconductors like In_xGa_{1-x}N, In_xAl_{1-x}N, and Al_xGa_{1-x}N can offer tunable bandgaps that cover the near-infrared (NIR)–visible–UV region. The chemical bonding within III-nitrides is usually very strong, to a certain extent, it gives them high melting point, mechanical strength, and chemical stability, and renders them resistance to high-current electrical degradation and radiation damage.^[168] In addition, these materials hold advantages of high electron mobility and saturation velocity, high breakdown field, large absorption coefficient, and good thermal stability and conductivity, making them extremely appropriate for high-power and high-speed electronics, blue/UV light-emitting diodes (LEDs) and laser diodes (LDs), and high-frequency transistors operating at high temperatures and in hostile environments.^[165] Among this class of semiconductors, Al_xGa_{1-x}N with a continuously tunable bandgap from 3.4 to 6.2 eV is the most widely explored material for solar-blind DUV light detection.^[8] Owing to the abovementioned distinctive features, we can infer Al_xGa_{1-x}N-based DUVPDs that can tolerate a large working bias voltage and operate at extremely harsh conditions have been realized.^[8] Besides, hexagonal BN (h-BN), the most stable crystalline form of BN, has also emerged as a promising candidate for solar-blind DUV photodetection, because of its extraordinary physical properties, in particular the large band-edge absorption coefficient as high as 7.5 × 10⁵ cm⁻¹.^[169] In the following section, we are going to discuss the research advances in solar-blind DUVPDs constructing its base elementarily on Al_xGa_{1-x}N and on h-BN reported in recent years.

5.1. Photoconductors

5.1.1. Al_xGa_{1-x}N/AlN

Al_xGa_{1-x}N epilayers suitable for solar-blind photoconductors application can grow on sapphire substrate by low pressure

MOCVD.^[170] The as-grown films had a good crystalline quality, as confirmed by the X-ray diffraction (XRD) analysis. Further optoelectronic characterization indicated that the as-fabricated $\text{Al}_x\text{Ga}_{1-x}\text{N}$ devices exhibited high sensitivity to DUV illumination. Notably, the cutoff wavelength of the devices can be briefly adjusted to as low as 271 nm, by tailoring the Al contents. Afterward, large-area AlN layers ($0.50 \times 0.55 \text{ mm}^2$) with different density of inversion domains (IDs) were synthesized on sapphire substrates by the usage of gas source MBE method.^[171] Significant reduction in the ID density was achieved by introducing AlN/GaN short period superlattices after the growth of AlN nucleation layer. Photoconductors made of AlN layers with ID density of 10^6 cm^{-2} showed a very low dark current of 0.5 fA at zero bias, which still remained below 50 fA at a high bias of 30 V. What is more, the devices displayed a peak responsivity of 0.08 A W^{-1} at $\approx 202 \text{ nm}$ and a cutoff wavelength of 213 nm, with a large rejection ratio (R_{202}/R_{285}) exceeding 10^3 .

5.1.2. h-BN

By using MOCVD technique, layers of h-BN have been epitaxially grown on sapphire substrates, prior to which 10 nm thick BN buffer layer serving as nucleation layer and also enhancing the adhesion of the subsequent h-BN epilayer was deposited.^[172] Photoconductors based on such epilayers had a low dark current of $\approx 10^{-11} \text{ A cm}^{-2}$ at a large bias of 100 V, and exhibited a peak photoresponse at 217 nm with a fierce cutoff wavelength at $\approx 230 \text{ nm}$, suggesting great potential for solar-blind DUV photodetection. Recently, 2D h-BN with thickness of several to tens of atomic layers that are ideal for solar-blind DUV photodetection have been successfully synthesized by PLD.^[173,174] Besides, ion beam sputtering deposition can produce uniform and continuous h-BN layers over a large area of decimeter scale on Cu foils, which was transferable to other substrates and was therefore favorable for fabricating optoelectronic devices.^[175] The substrate temperature during the growth process has a substantial influence on the density of grain boundary and crystalline quality, and thus the optoelectronic properties of the as-prepared h-BN layers. Photodetectors made from optimal h-BN layers exhibited high photoresponse characteristics with $I_{\text{light}}/I_{\text{dark}}$ exceeding transcending 10^3 at 212 nm DUV illumination and a steep cutoff wavelength at $\approx 225 \text{ nm}$.^[175] The responsivity, specific detectivity, and response speed are 0.1 mA W^{-1} , $2.4 \times 10^8 \text{ Jones}$, and $0.32/0.63 \text{ s}$, respectively. Due to their good thermal stability and conductivity, h-BN DUVPDs can operate properly with excellent features in stability and repeatability even at a working temperature as high as $400 \text{ }^\circ\text{C}$, suggesting the great future for the use in some special applications where high temperature was required.^[174]

5.2. MSM Photodetectors

5.2.1. $\text{Al}_x\text{Ga}_{1-x}\text{N}/\text{AlN}$ Thin Films

Due to the extremely wide bandgap and the presence of enormous surface states, $\text{Al}_x\text{Ga}_{1-x}\text{N}$ can easily form Schottky contact with most of metal electrodes. Therefore, the majority of $\text{Al}_x\text{Ga}_{1-x}\text{N}$ photodetectors with the geometry of two metal

contacts affixed to opposite sides of the material can be regarded as MSM photodetectors. In general, the $\text{Al}_x\text{Ga}_{1-x}\text{N}$ layers for MSM device application grow on sapphire substrates via MOCVD,^[176–189] MBE,^[190,191] sputtering method,^[192,193] and metal–organic vapor phase epitaxy (MOVPE).^[194,195] In order to push forward with the growth of high-quality $\text{Al}_x\text{Ga}_{1-x}\text{N}$ layers and also to promote the adhesion between the layers and substrates, GaN or AlN layers with thickness of tens to hundreds of nanometers were often employed as buffer or nucleation layers.^[178,180–182,184,187–189,191,193–195] It has been found that with the increase of x value, the peak response as well as the cutoff wavelengths of the MSM photodetectors manifested obvious blue transfer to shorter wavelength, an indicative of variation in the $\text{Al}_x\text{Ga}_{1-x}\text{N}$ bandgap. Meanwhile, the $\text{Al}_x\text{Ga}_{1-x}\text{N}$ MSM devices had dark current as low as tens of femtoamperes even at a very large operating bias voltage of 300 V.^[176,182,183,185] The $I_{\text{light}}/I_{\text{dark}}$ ratio, responsivity, and photoresponse rejection ratio achieved in these studies were usually in the range of 10^2 – 10^7 , 100–400 mA W^{-1} , and 10^2 – 10^4 , respectively, which depended intensely on the operating bias voltage and DUV light intensity. In some cases, ultrafast DUV photodetection with 3 dB bandwidth as large as 150 MHz have also been realized.^[182]

Li et al. have fabricated DUVPDs that consisted in MOCVD-grown high quality AlN epilayers (Figure 11a,b), which demonstrated a peak responsivity with maximum value of 0.4 A W^{-1} at 200 nm and a very vigorous cutoff wavelength at 207 nm.^[183] In addition, the device also possessed a low dark current of $\approx 100 \text{ fA}$ at a large bias of 200 V (Figure 11c), and a large photoresponse rejection ratio (R_{200}/R_{280}) exceeding 10^4 (Figure 11d). The dark current depended strongly on the thickness of the AlN layers. In another study, we find MSM photodetectors based on 4.0 μm thick AlN layers had a dark current of $\approx 50 \text{ fA}$, while the current value increased dramatically to $\approx 300 \text{ fA}$ for 1.5 μm thick AlN-based device at a high voltage of 300 V.^[185] Therefore, these results could be correlated with the distinguished density of the threading dislocation in AlN layers with different thicknesses, as confirmed by the XRD measurement, and suggested that improved sensitivity can be possible by constructing DUVPDs and exploiting thicker AlN layers.

Various studies have shown that the photoresponse of $\text{Al}_x\text{Ga}_{1-x}\text{N}$ MSM photodetector was determined not only by the Al content, but also by the properties of the buffer layer between $\text{Al}_x\text{Ga}_{1-x}\text{N}$ and substrates.^[179,184] In a recent work, the authors found that, with the increase of Al contents (from 0.4 to 0.6 in molar percentage), the cutoff wavelengths of $\text{Al}_x\text{Ga}_{1-x}\text{N}$ MSM photodetectors shifted gradually from 290 to 251 nm, and additionally, both peak and band-edge responsivities reduced monotonously.^[179] Furthermore, by increasing the operational voltage from 3 to 20 V, the peak responsivity rose exponentially by more than 2 orders of magnitude from ≈ 0.1 to $\approx 12 \text{ A W}^{-1}$, indicating the presence of an internal gain mechanism clearly.

Lu and co-workers reported the synthesis of large-area $\text{Al}_{0.4}\text{Ga}_{0.6}\text{N}$ epilayers on AlN buffer layers for solar-blind DUVPDs, which revealed a low dark current density of 3.2 pA cm^{-2} under 20 V bias, and a breakdown voltage of up to 385 V.^[188] When working at $150 \text{ }^\circ\text{C}$, the dark current can keep almost invariant, while the photocurrent decreased by 20–40% in comparison with those at room temperature.^[178,189]

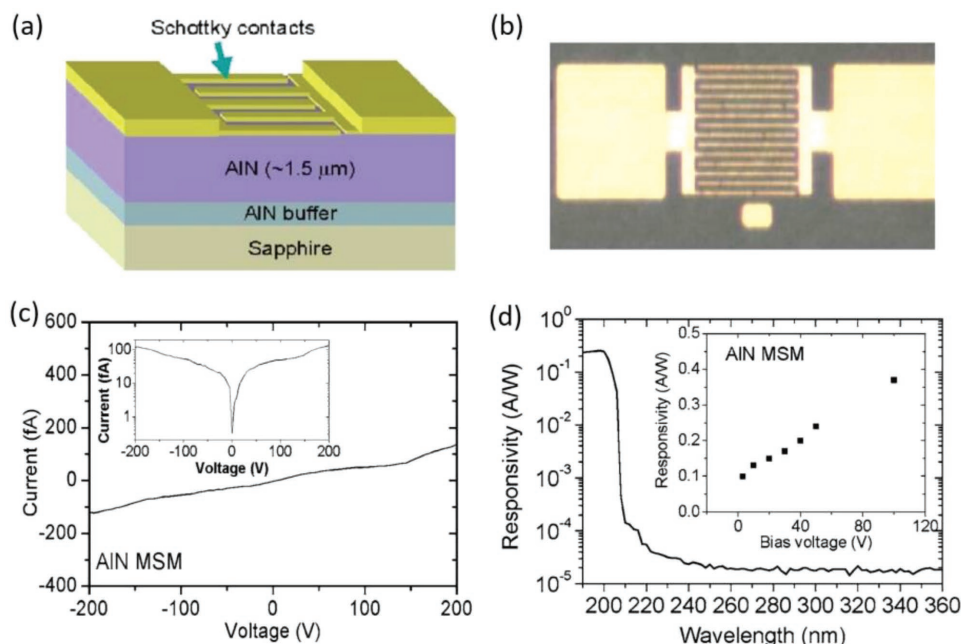


Figure 11. a) Schematic diagram of a MSM photodetector based on AlN epilayer. b) An optical microscopy of the fabricated MSM photodetector. c) I - V characteristic of the AlN MSM photodetector in dark. d) Spectral response of the device at 30 V. The inset shows the responsivity of the device as a function of the applied bias. Reproduced with permission.^[183] Copyright 2006, American Institute of Physics Publishing.

Such a degradation in photocurrent was likely to be caused by the enhanced carrier recombination at high temperatures. The relatively incredible device stability at high temperature and the exceptional high $I_{\text{light}}/I_{\text{dark}}$ ratio of 10^7 upon 254 nm DUV illumination suggest the promising application in rigorous condition. Apart from $\text{Al}_x\text{Ga}_{1-x}\text{N}$, AlN epilayers can be used to fabricate solar-blind DUVPDs for harsh electronics as well (Figure 12a).^[192] The AlN photodetectors on Si showed a dark current as low as ≈ 1 nA even at an operating bias higher than 200 V. As shown in Figure 7b–d, the devices were capable of detecting DUV illumination up to 300 °C with the photo-dark current ratio (PDCR, defined as $(I_{\text{light}} - I_{\text{dark}})/I_{\text{dark}}$) decreasing from 63 at room temperature to 3.5, owing to the small levels of leakage current and high thermal stability of AlN at a high temperature. Nevertheless, further aggrandizing the temperature to 400 °C led to a substantial increase in dark current, which cannot be distinguished from the photocurrent, showing a sign that the devices cannot work properly. It is also worth noting that the devices exhibited fair radiation tolerance, and they can operate properly even after proton radiation exposure with a 3 MeV proton fluence of 10^{13} cm⁻². The excellent temperature tolerance and radiation hardness, together with the fast response speed of $\approx 110/\approx 80$ ms confirmed that the AlN solar-blind DUVPDs hold great promise for the extremely harsh electronic applications, such as sensing, imaging, and intrachip optical interconnects in the space environment marked by high temperature and high radiation.

The device performance of the DUVPDs can be optimized by introducing Al nanoparticles (NPs), so that it can induce surface plasmon resonance under DUV illumination.^[180,181] For example, by exploiting a nanosphere lithography technique, size-controlled Al NP arrays were decorated onto

$\text{Al}_x\text{Ga}_{1-x}\text{N}$ -based MSM photodetectors. This decoration led to not only a reduction in dark current, but also an increase in photocurrent (Figure 13a,b).^[181] As a consequence, the $I_{\text{light}}/I_{\text{dark}}$ ratio risen dramatically from $\approx 10^2$ to $\approx 10^6$ at 269 nm under 20 V bias. Another point worthy of mention was that the peak responsivity was enhanced by more than 25 times, reaching 2.34 A W⁻¹ (Figure 13c). The reduced dark current on one hand is put down to the suppression of carrier transport via conductive defect states by the surface-oxidized Al NPs that act as a passivation layer for $\text{Al}_x\text{Ga}_{1-x}\text{N}$, while the improved photocurrent was due to the increased optical absorption by field enhancement and light scattering by Al NPs (Figure 13e), as well as the injection of hot electrons from the NPs to $\text{Al}_x\text{Ga}_{1-x}\text{N}$ layers (Figure 13d), according to theoretical calculation. On the other hand, the enhanced electromagnetic field surrounding the Al NPs can accelerate the separation of electron–hole pairs, and it will lead to the enhancement of photocurrent.

To overcome drawbacks like large dark current and slow response inherent to UWBG semiconductor-based photodetectors with large internal gains, quasilayer of BGaN monolayer/semi-insulating iron-doped GaN superlattices grown by MOVPE method was employed as the active layer.^[196] It was observed that the usage of superlattice structure can lower the dark current, while maintaining the high internal gain with value of up to 3×10^4 for low optical power, and achieving rapid time response of tens of nanoseconds for high optical power. Furthermore, narrowband DUV photodetection has also been achieved by employing MOVPE-grown ultra-short-period $(\text{AlN})_m/(\text{GaN})_n$ superlattices with tunable well and barrier atomic layer numbers (Figure 14a).^[197] As revealed by the HRTEM image in Figure 14b, the as-grown superlattices contained well-defined, coherently strained GaN and AlN layers

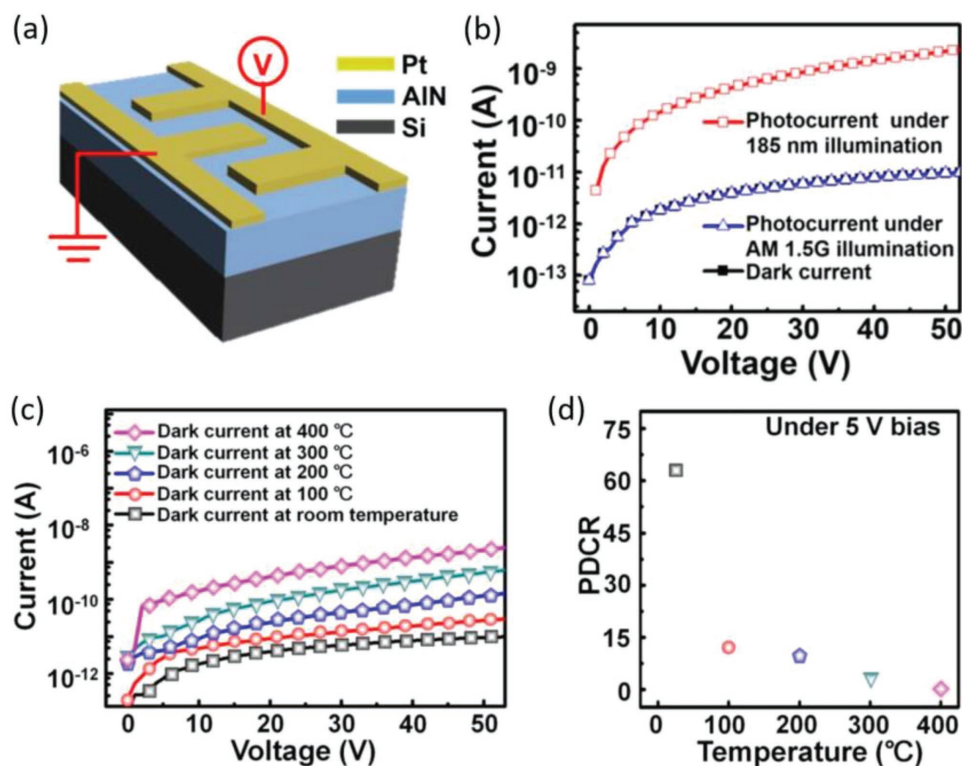


Figure 12. a) Schematic diagram of an AlN MSM photodetector on Si substrate. b) I - V curves of the AlN MSM photodetector measured in the dark and under AM 1.5G illumination and 185 nm DUV illumination. c) I - V curves of the AlN MSM photodetector measured in the dark at different working temperatures. d) PDCR value as a function of temperature under 5 V bias and 185 nm light illumination. Reproduced with permission.^[192] Copyright 2013, Nature Publishing Group.

as thin as two atomic layers. Due to the interband transitions between quantum states along the [0001] direction in ultrathin GaN atomic layers isolated by AlN barriers, the superlattices can exhibit optical absorption bands as narrow as 9 nm at DUV wavelength region, as confirmed by both theoretical and experimental results. Precise adjustment of the atomic layer numbers of 1, 2, 4, and 6 for the GaN 2D layers gave peak response wavelength at 230, 240, 248, and 266 nm, respectively (Figure 14c), which was attributed to the tunable absorption spectrum because of quantum confinement effect. MSM photodetectors based on this special superlattice with 4 atomic layer reached a responsivity of 51 mA W^{-1} under 240 nm DUV illumination at a bias of 40 V. The results suggested great possibility for realizing wavelength selectable and narrowband DUV photodetection without the use of additional optical filters.

5.2.2. AlN Micro-/Nanowires

Zheng et al. presented the triumphant growth of high-quality defect-free AlN micro-/nanowires via a two-step physical vapor transport method.^[198] In darkness, devices made from such an individual micro-/nanowire exhibited a dark current lower than 100 fA at a bias of 20 V together with a large breakdown voltage higher than 100 V. Upon 193 nm DUV radiation, the current increased drastically to as high as 24 nA, giving rise to a large $I_{\text{light}}/I_{\text{dark}}$ ratio exceeding 10^5 . The responsivity reached

0.39 A W^{-1} , which was ≈ 2 orders of magnitude higher than that of AlN film-based devices. Another point is that the detectors showed a sharp response cutoff at the wavelength of 208 nm with a photoresponse rejection ratio (R_{190}/R_{260}) exceeding 10^2 . The rise and decay times were estimated to be <0.1 and <0.2 s, respectively. Such a relatively good response speed can be attributed to the following aspects: 1) the single-crystalline nature of micro-/nanowire with low defect density greatly lowers the probability of carrier scattering and thus retain the high carrier mobility; 2) the reduced dimensionality of the micro-/nanowire provides an effective conductive channel, which can confine the active area of the charge carriers and shorten their transit time.

5.2.3. h-BN/Cubic BN (c-BN)

Apart from $\text{Al}_x\text{Ga}_{1-x}\text{N}$ and the relative heterostructures, BN has also demonstrated great potential for solar-blind DUV MSM photodetector application.^[199,200] High-quality c-BN films have been successfully grown in an electron-cyclotron-resonance microwave plasma CVD or PECVD system.^[201,202] MSM photodetector based on c-BN films displayed a peak responsivity of 32 mA W^{-1} at 180 nm and a very steep cutoff wavelength at 193 nm.^[201] The photoresponse rejection ratio (R_{180}/R_{250}) exceeded 10^4 , suggesting that c-BN was a very feasible material for DUV sensing. By using MOCVD technique, h-BN epilayers have been synthesized, which exhibited a large band-edge absorption coefficient

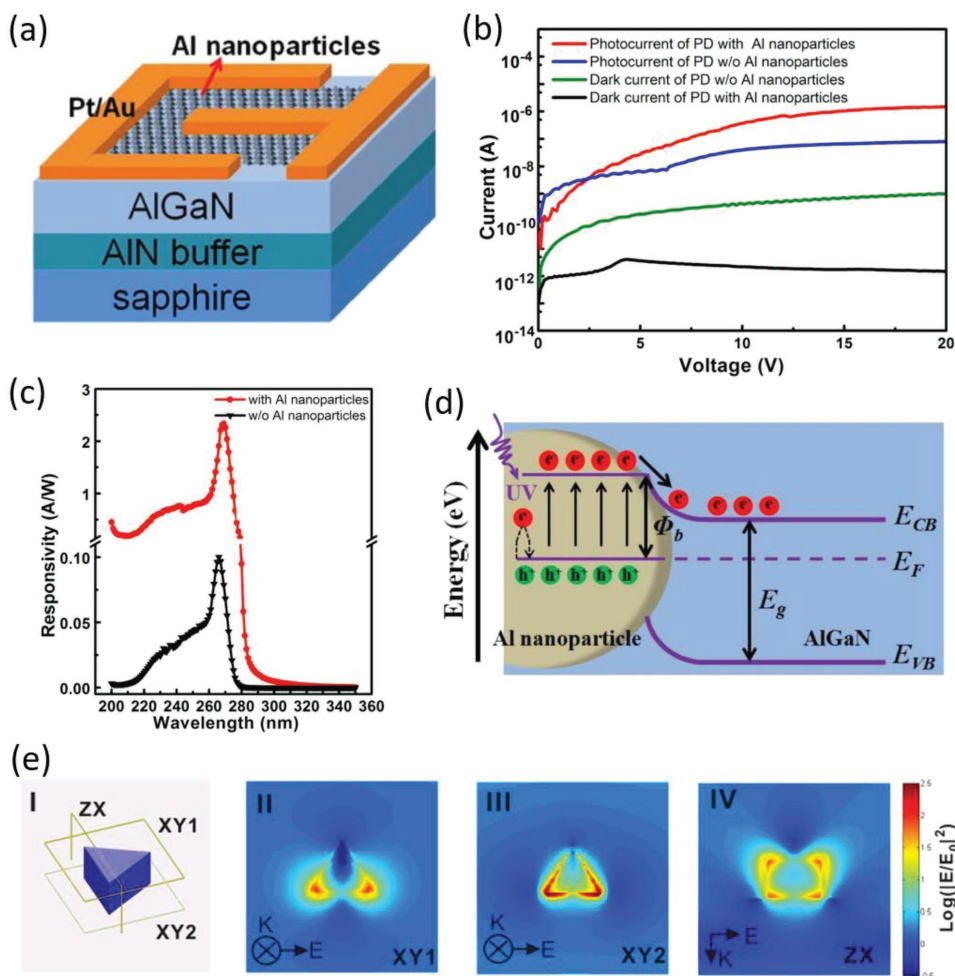


Figure 13. a) Schematic illustration of an AlGaIn-based MSM photodetector with size-controlled and well-ordered Al nanoparticle arrays. b) I - V characteristics of the photodetector with and without Al NPs in dark and under DUV illumination. c) Spectral response of the detector with and without Al NPs under 20 V applied bias. d) Schematic illustrating the charge transfer process between AlGaIn and Al NPs under DUV radiation. e) Electric field intensity distribution at different positions for I) a single Al NP on sapphire under 268 nm light illuminating obtained by finite-difference time-domain (FDTD) simulation: II) the top, III) the bottom, and IV) the side view. Reproduced with permission.^[181] Copyright 2015, American Institute of Physics Publishing.

as high as $7 \times 10^5 \text{ cm}^{-1}$.^[203] Such a high value implied that virtually all incoming photons can be absorbed by only a very thin layer of h-BN with a thickness of $\approx 70 \text{ nm}$. h-BN layer-based MSM photodetectors disclosed a peak responsivity at 220 nm with a sharp cutoff wavelength at $\approx 230 \text{ nm}$. What is more, the device can withstand a large working voltage as high as $\approx 800 \text{ V}$, which is consistent with a breakdown electric field of $\approx 4.4 \text{ MV cm}^{-1}$. 2D h-BN has also been explored as the active material in MSM photodetectors.^[204,205] For instance, h-BN nanosheet photodetector fabricated through PLD technique exhibited a relatively low dark current of $\approx 15 \text{ nA}$ and virtually no sign of breakdown, even at a very large operating bias of 800 V .^[204] The DUV/visible rejection ratio (R_{227}/R_{450}) can reach as high as 10^8 . What is more, the devices showed a fast response speed of 0.6/1.8 ms, much quicker than that of thicker h-BN MSM photodetectors. Recently, Wang et al. brought forth the synthesis of large-sized single-crystalline h-BN domains with a lateral size up to $100 \mu\text{m}$ on Ni foils using ion beam sputtering deposition method.^[205] The MSM photodetectors building its

base on such a h-BN monolayer were extremely sensitive to 190 nm DUV illumination with a large $I_{\text{light}}/I_{\text{dark}}$ ratio of 10^3 .

5.3. p-n and p-i-n Junction Photodiodes

Because of the ascending difficulty in the introduction and activation of p-type dopant such as Mg atoms in $\text{Al}_x\text{Ga}_{1-x}\text{N}$ compounds, construction of $\text{Al}_x\text{Ga}_{1-x}\text{N}$ -based p-n junctions remains a challenge.^[206,207] Nikishin and co-workers expounded that effective p- and n-type doping can be successfully realized by using Mg and Si as dopants, respectively, in superlattices of AlN/AlGa(In)N with AlN content as high as 0.73.^[208] With this advantage, they fabricated solar-blind photodetectors based on p-n junctions of AlN/AlGa(In)N superlattices.^[209] The device structure basically consisted of an AlN nucleation/buffer layer deposited on sapphire, followed by a Si-doped GaN buffer layer, two n- and p-type AlN/AlGa(In)N superlattices, and Mg-doped $\text{Al}_{0.08}\text{Ga}_{0.092}(\text{In})\text{N}$ contact layer. Without any surface

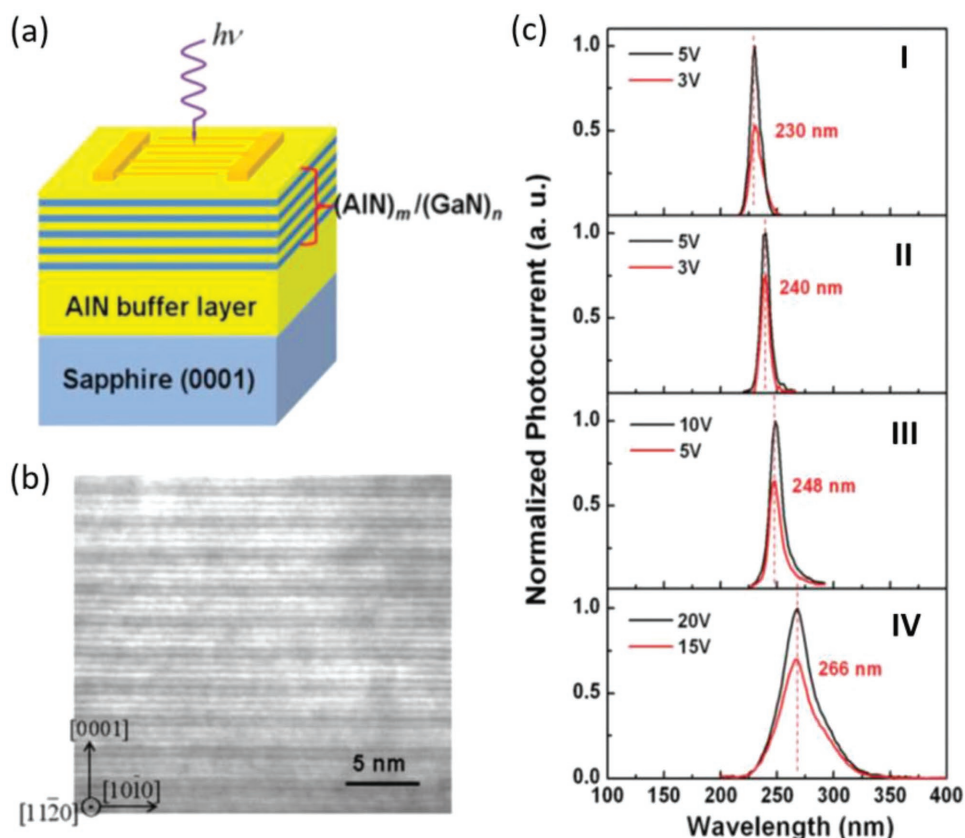


Figure 14. a) 3D schematic of the photodetector-based $(\text{AlN})_m/(\text{GaN})_n$ superlattice. b) A representative cross-sectional TEM image of the superlattice. c) Normalized photocurrent spectra as a function of wavelength under different biases with light illumination. The curves correspond to the GaN 2D layers with atomic layer numbers of 1, 2, 4, and 6 isolated by the same barriers of ≈ 6 AlN atomic layers, respectively. Reproduced with permission.^[197] Copyright 2014, Royal Society of Chemistry.

passivation, the detectors achieved a low dark leakage currents of 0.2–0.3 pA, and high zero-bias resistance of $\approx 1 \times 10^{11} \Omega$. The peak responsivity of 25 mA W^{-1} was obtained at wavelength below 260 nm, which coincides with EQE value of 12.5%. What is more, the device exhibited a large rejection ratio (R_{260}/R_{380}) as high as 10^6 . Recently, higher EQE of $\approx 50\%$ has been achieved in $\text{Al}_{0.64}\text{Ga}_{0.36}\text{N}/\text{Al}_{0.34}\text{Ga}_{0.66}\text{N}$ p–n junction photodetectors with high-Al content multiple quantum wells.^[210] The devices had a peak responsivity of 0.1 A W^{-1} at 250 nm, which dropped off by $>10^3$ at 280 nm. The dark current was <0.1 pA at a bias of -0.5 V. In addition, a bandwidth-limited response time of 0.4 μs was accomplished, suggesting that this structure was potentially useful for high-speed DUV photodetection.

In addition to MSM photodetectors, $\text{Al}_x\text{Ga}_{1-x}\text{N}$ p–i–n photodiodes have been an equally considerable device geometry.^[189,211–227] By virtue of the relatively poor quality of p-type $\text{Al}_x\text{Ga}_{1-x}\text{N}$, the p–i–n photodiodes are typically designed with n-type layer at the bottom. The employed p- and n-type dopants in the reported studies are usually Mg and Si, respectively. However, Si–In codopant was sometimes used as well, which was beneficial for mitigating some of the remaining strain and allowing for the growth of thicker, higher quality, and low resistance n-type conduction layer.^[216] With the purpose of facilitating the collection of photocarriers, a thin p-type GaN (5–10 nm) was even incorporated between the p–i–n

structure and metal contact because p-GaN was more conductive than p- $\text{Al}_x\text{Ga}_{1-x}\text{N}$.^[221,223] Up to now, $\text{Al}_x\text{Ga}_{1-x}\text{N}$ -based p–i–n photodiodes have achieved peak responsivities in the range of 10.8–180 mA W^{-1} (EQE values of 7–90%), which depended strongly on the applied reverse biases. Furthermore, the photoresponse rejection ratios are in the range of 10^3 – 10^6 . Due to the extremely large bandgaps, the $\text{Al}_x\text{Ga}_{1-x}\text{N}$ -based p–i–n photodiodes exhibited very low dark current, yielding a high specific detectivity in the range of 10^{11} – 10^{14} Jones.

In some early studies, $\text{Al}_x\text{Ga}_{1-x}\text{N}$ -based p–i–n photodiodes usually worked in front-illuminated mode, namely the incident photons were absorbed at the front side electrode. These detectors were fabricated by depositing p–i–n structure on GaN templates. For example, an $\text{Al}_x\text{Ga}_{1-x}\text{N}$ photodiode with the structure of front electrode/Mg-doped $\text{Al}_x\text{Ga}_{1-x}\text{N}/\text{Al}_x\text{Ga}_{1-x}\text{N}/\text{Si}$ -doped $\text{Al}_x\text{Ga}_{1-x}\text{N}/\text{Si}$ -doped GaN/GaN/sapphire has grown on sapphire substrates by low-pressure MOCVD, as schematically shown in **Figure 15a**.^[211] In the device, an additional semitransparent electrode and Mg-doped GaN cap layer were employed to advance the carrier collection since p- $\text{Al}_x\text{Ga}_{1-x}\text{N}$ had high resistivity and therefore the collection of photogenerated holes was less efficient. With this design, the peak responsivity can be improved by several orders of magnitude, reaching 0.05 A W^{-1} at 232 nm (Figure 15b), which can be further enhanced to 0.11 A W^{-1} by applying a bias of -5 V.

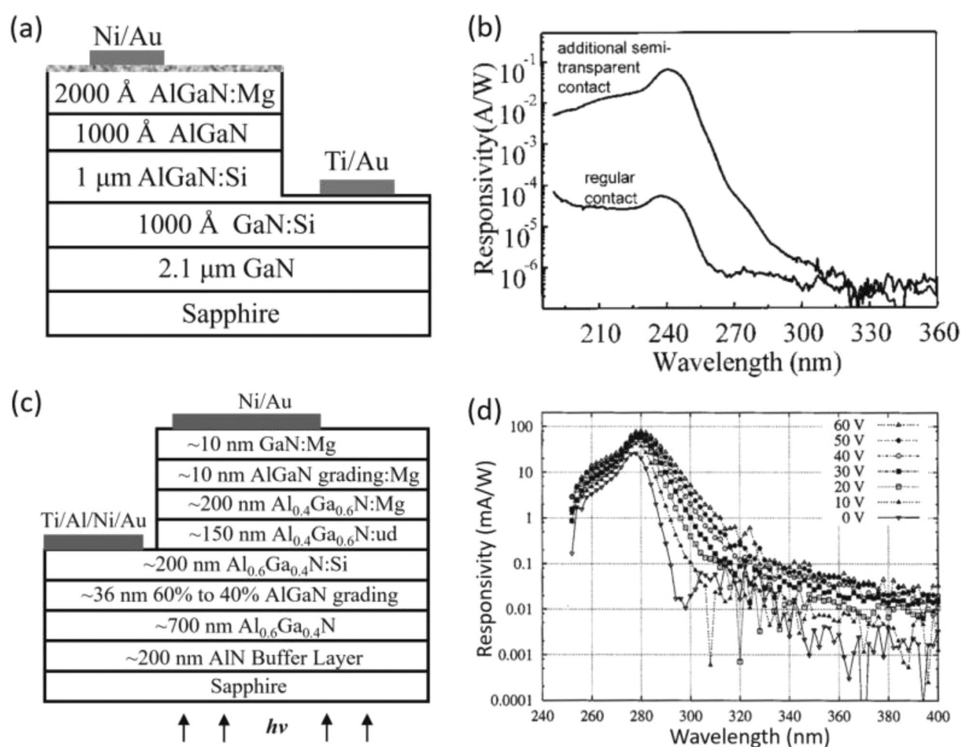


Figure 15. a) Schematic illustration of a front-illuminated $\text{Al}_x\text{Ga}_{1-x}\text{N}$ -based p-i-n photodiode. b) Spectral responsivity of the photodetector comparing traditional and semitransparent contact schemes. Reprinted with permission.^[211] Copyright 2000, American Institute of Physics Publishing. c) Schematic illustration of a back-illuminated $\text{Al}_x\text{Ga}_{1-x}\text{N}$ -based p-i-n photodiode. d) Spectral responsivity of the photodetector at different reverse working biases. Reproduced with permission.^[223] Copyright 2001, IEEE Publishing.

The high responsivity value corresponded to internal quantum efficiency (IQE) of $\approx 90\%$. What is more, the photoresponse rejection ratio (R_{232}/R_{275}) was as high as 10^4 . p-i-n Photodiodes fabricated on lateral epitaxial overgrowth (LEO) GaN can have superior DUV photoresponse performance than that on dislocated GaN. For example, they exhibited a faster response, a sharper cutoff in the spectral response, and a smaller dark current that is several orders of magnitude lower than conventional devices.^[220] Persistent photoconductivity (PPC), in which the recovery from the optical stimulus takes very long time, has been an unfavorable issue in UWBG semiconductor-based solar-blind DUVPDs.^[228,229] In order to reduce the PPC in $\text{Al}_x\text{Ga}_{1-x}\text{N}/\text{GaN}$ photodetectors, Hou et al. employed a localized heating strategy by suppressing device suspension and in situ heating, and eventually it can enable acceleration of the carrier capture rate during operation.^[230] It was found that the PPC behavior was considerably decreased by nearly 3 orders of magnitude from tens of hours to second level, which is very important for high-accuracy and fast-responsive detection application.

To avoid absorption loss, $\text{Al}_x\text{Ga}_{1-x}\text{N}$ photodiodes operating in back-illuminated mode have been developed recently. Considering the relatively small bandgap and efficient absorption of incident UV of <280 nm, thick GaN layer is no longer suitable for growing the p-i-n structure. Therefore, AlN and n-type $\text{Al}_x\text{Ga}_{1-x}\text{N}$ films with higher Al contents were preferable to be employed as buffer and nucleation layers on the bottom of substrates, which had larger bandgap than i- and p-type $\text{Al}_x\text{Ga}_{1-x}\text{N}$ layers, and hence enabling the photons of

interest to reach the depletion region of the photodiodes with minimal absorption loss. Typically, the Al concentrations in the bottom n-type layer were in the range of 0.60–0.40, while the values were 0.37–0.40 in the i- and p-type layers. In addition, the Al content was sometimes graded at the interfaces, which was conducive to minimizing stress between the heterostructure layers and piezoelectric effects. For instance, by using LP-MOCVD technique, p-i-n photodiodes with a structure of sapphire/AlN/ $\text{Al}_{0.6}\text{Ga}_{0.4}\text{N}/\text{Al}_x\text{Ga}_{1-x}\text{N}$ ($0.4 < x < 0.6$)/Si-doped $\text{Al}_{0.4}\text{Ga}_{0.6}\text{N}/\text{i-Al}_{0.4}\text{Ga}_{0.6}\text{N}/\text{Mg-doped Al}_{0.4}\text{Ga}_{0.6}\text{N}/\text{Mg-doped Al}_x\text{Ga}_{1-x}\text{N}$ ($0.0 < x < 0.4$)/Mg-doped GaN/metal contact layer was fabricated (Figure 15c).^[223] At the bias of 0 and -60 V, the devices exhibited peak responsivities of 27 and 79 mA W^{-1} under 280 nm illumination, respectively, with DUV/visible rejection ratio (R_{280}/R_{400}) exceeding 10^3 (Figure 15d). In addition, a very low dark current of ≈ 5 nA cm^{-2} at -10 V was achieved, which released a large specific detectivity as high as 5×10^{13} Jones. A large number of approaches have been developed to optimize the DUV photoresponse.^[216,226,227] For example, the dark current of p-i-n photodiodes can be reduced dramatically by ≈ 2 orders of magnitude, reaching 3 fA at a bias of -6 V, when the p-type GaN cap layer experienced recess etching.^[226] In this case, the peak responsivity was 0.11 A W^{-1} at 260 nm under -10 V bias and a DUV/visible rejection ratio (R_{260}/R_{400}) reached more than 10^4 . What is more, the ultralow dark current led to a high differential resistance of $9.52 \times 10^{15} \Omega$, yielding a thermally limited specific detectivity as high as 4.9×10^{14} Jones. Through surface passivation of the sidewall of the active layers by oxygen plasma,

Kuryatkov et al. reported p–i–n photodiodes based on short period superlattices of AlN/Al_{0.08}Ga_{0.92}N.^[227] A low dark current of ≈3 pA cm⁻² and high zero-bias resistance of ≈6 × 10¹⁴ Ω were realized. Besides, the device exhibited a peak responsivity of 62 mA W⁻¹ at -10 V bias and a DUV/visible rejection ratio (R_{240}/R_{320}) of approaching 10⁵. By using Si–In codoping method, high-performance p–i–n photodiodes with unbiased peak responsivity and EQE of ≈176 mA W⁻¹ and ≈80% at 275 nm, and a DUV/visible rejection ratio (R_{275}/R_{400}) exceeding 10⁶ have been realized.^[216] The EQE value increased to 89% at a bias of -5 V, correspondingly to an IQE as high as ≈98%.

The rapid development of Al_xGa_{1-x}N-based solar-blind DUV photodiodes has also brought about research interests in avalanche photodiodes. However, due to the inherent limitations that can lead to cracking of the material, large dislocation densities, low doping efficiencies, and lattice and thermal expansion mismatches with substrates, the realization of Al_xGa_{1-x}N-based avalanche photodiodes is extremely sophisticated. In 2005, McClintock et al. reported the first observation of avalanche multiplication in Al_xGa_{1-x}N-based photodiodes.^[231] Upon exposure to DUV illumination, the optical gain displayed a soft breakdown originating at relatively low electric fields, and eventually saturating without showing a Geiger mode breakdown. At a bias of -60 V, a maximum optical gain exceeding 700 has been achieved, which corresponded to an electric field strength of 1.7 MV cm⁻¹ in the light of finite element modeling. Recently, avalanche photodiodes with Al_xIn_{1-x}N-/Al_xGa_{1-x}N-distributed Bragg reflectors were numerically demonstrated.^[232] It was revealed that with the introduction of p-type Al_xGa_{1-x}N layer and low Al multiplicative layer, the avalanche breakdown voltage was significantly reduced by 13%, compared with conventional device structure. Such a reduction in avalanche breakdown voltage was partially due to the presence of an internal polarized electric field. Moreover, the higher conductive p-Al_xGa_{1-x}N that shared a lower voltage drop due to a higher doping efficiency is also a contributory factor.

5.4. Schottky Photodiodes

Al_xGa_{1-x}N-based Schottky photodiode has been one of the most studied device geometries for solar-blind DUV photodetection. The Schottky contacts can be formed using electrode including Pd,^[233] Pt,^[234,235] indium-tin-oxide (ITO),^[236] and iridium oxide films.^[237] Moreover, lateral geometry Schottky photodiodes composed of In–Si-codoped Al_xGa_{1-x}N with the maximum Hall electron concentration and mobility of 8 × 10¹⁷ cm⁻³ and 40 cm² V⁻¹ s⁻¹, respectively, and 5 nm thick Pd Schottky contact has been also demonstrated.^[233] For this special geometry, the peak responsivity is 0.033 A W⁻¹ at 275 nm, with a large rejection ratio (R_{275}/R_{305}) of more than 10³. High-quality AlN epilayers grown on SiC substrate, which had excellent lattice match with AlN (≈1%), were coated with 10 nm thick Pt to form Schottky photodiode DUVPD (Figure 16a).^[234] As displayed in Figure 16b, a peak responsivity of 0.12 A W⁻¹ at 200 nm and very sharp cutoff wavelength around 210 nm were attained. In addition, the photodiodes exhibited very high breakdown voltages exceeding 200 V, a very low dark current below 10 fA at a bias of -50 V, and a photoresponse rejection

ratio (R_{200}/R_{280}) approaching 10⁴ (Figure 16c,d). What is more, due to the extremely low leakage current and high zero bias responsivity, the thermally energy limited specific detectivity as high as 1.0 × 10¹⁵ Jones was realized. Besides noble metals, some metal oxides like ITO can also form Schottky contact with Al_xGa_{1-x}N as well.^[236] The as-assembled ITO–Al_xGa_{1-x}N photodiodes exhibited a low dark currents of <1 pA at a bias of -20 V and a breakdown voltages higher than 40 V. Specifically, a maximum responsivity of 44 mA W⁻¹ was achieved at 263 nm, which corresponded to EQE value of 21%. Further time-domain high-frequency measurements showed a 3 dB bandwidth that is as high as 1.10 GHz, signifying promising potential for high-speed DUV photodetection application.

To conclude, photoconductors or MSM photodetectors based on Al_xGa_{1-x}N thin films typically exhibit decent peak responsivities from tens to hundreds of mA W⁻¹, reasonable photoresponse rejection ratio of 10²–10⁴, and high $I_{\text{light}}/I_{\text{dark}}$ ratio of 10²–10⁷. Moreover, these devices possess low dark current in the level of picoamperes, and can withstand extremely high breakdown voltage (hundreds of volts). Tuning the peak response and cutoff wavelength is possible by tailoring the content of Al. Besides, performance enhancement can be realized by optimizing the properties of buffer layer between Al_xGa_{1-x}N and growth substrate, and exploiting surface plasmon resonance effect. In addition, BN-based photoconductors or MSM photodetectors usually show lower responsivity values from 0.1 to 32 mA W⁻¹, with maximum photoresponse rejection ratio exceeding 10⁸ and decent $I_{\text{light}}/I_{\text{dark}}$ ratio of 10³. On the other hand, p–n (p–i–n) or Schottky junction photodiodes made from Al_xGa_{1-x}N thin films can display peak responsivities from tens to hundreds of mA W⁻¹, and high photoresponse rejection ratio in the range of 10³–10⁶. More importantly, due to the extremely low dark current in the level of 10⁻¹⁴–10⁻¹² A, these detectors can achieve high specific detectivity with the maximum value reaching 10¹⁵ Jones. Narrowband DUV photodetection is also realized by exploring a device geometry of ultrashort period (AlN)_m/(GaN)_n superlattices with tunable well and barrier atomic layer numbers. At the current stage, there still remain some issues limiting the development of III-nitride compound-based DUVPDs. For instance, due to the lack of suitable substrates, preparation of Al_xGa_{1-x}N thin films with high quality is rather difficult. Another big challenge is the difficulty to achieve highly conductive p-type Al_xGa_{1-x}N thin films because of the large activation energy of the widely employed Mg dopant in Al_xGa_{1-x}N with high Al content, so it turns out that it restricts exploration of light detection at shorter wavelength.

6. Diamond

Diamond is a solid crystal of tetrahedrally bonded carbon atoms in a covalent network lattice.^[238] It possesses a host of extreme properties, such as exceptional thermal conductivity and saturation velocity, high charge carrier mobility and resistivity, the lowest dielectric constant of all semiconductors, which render the highest figure-of-merit for high-temperature, high-power, and high-frequency operation.^[239–241] In addition, this material has other outstanding features like a wide

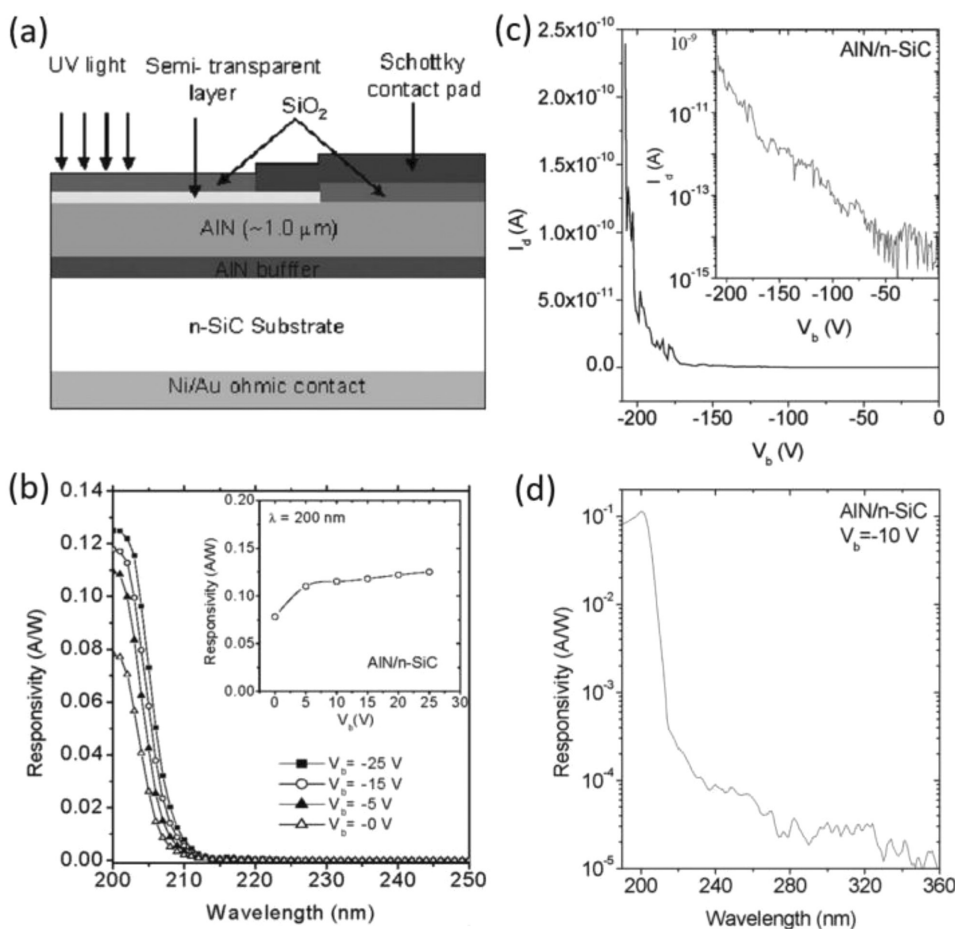


Figure 16. a) Schematic illustration of a Pt/AlN Schottky photodiode on SiC substrate. b) Spectral responsivity of the photodetector at different reverse bias voltages. The inset shows the peak responsivity at 200 nm as a function of working bias. c) I - V characteristics of the photodetector. The inset shows the same plot in semilog scale. d) Spectral responsivity of the photodetector measured at a reverse bias of 10 V. Reproduced with permission.^[234] Copyright 2007, American Institute of Physics Publishing.

bandgap as large as 5.5 eV and radiation and corrosion resistance, making it an attractive candidate for solar-blind DUV photodetection especially in harsh conditions.^[242,243] However, the wide use of diamond for DUV photodetection has been impeded because of the high cost, and difficulty of access to large size diamond.^[13] The establishment of CVD growth processes has paved the way for developing diamond-based DUVPDs.^[13] The wafer-scale polycrystalline diamond that is suitable for DUV detector application can be heteroepitaxially grown on Si substrates. Nevertheless, the high insulating property of undoped diamond makes it impossible to fabricate solar-blind DUVPDs. To address this issue, a number of atoms including B, N, and Mg have been doped into diamond as dopants to tune the electrical property. Extensive study has shown that while the p-type doping of diamond can be readily realized using boron, n-type doping is extremely difficult because of the close packing and rigidity of the diamond lattice that prevents the incorporation of atoms larger than carbon.^[13] In spite of these existing challenges, various types of solar-blind DUVPDs made from diamonds have been realized in recent years. In this section, we will introduce the recent achievement in this field.

6.1. Photoconductors

As an ideal building block for solar-blind DUV photoconductors, the polycrystalline thin film is usually deposited on single-crystal Si substrates or on high-pressure/high-temperature grown Ib(100)-type and IIa(100)-type single-crystal diamonds.^[228,244–256] The synthetic methods so far include microwave-enhanced CVD and PECVD techniques. The detectors typically exhibited steep cutoff wavelengths at around 225 nm. For example, Liao and Koide presented a high-performance planar photoconductor employing unintentionally doped homoepitaxially grown diamond thin film.^[251] The device had a low dark current of around 1 pA, and a large $I_{\text{light}}/I_{\text{dark}}$ ratio exceeding 10^4 under 220 nm DUV illumination at a bias voltage of 20 V (Figure 17a). The responsivity at 220 nm was estimated to be $\approx 6 \text{ A W}^{-1}$ at 3 V bias, corresponding to a photoconductive gain of 33. What is more, the detectors exhibited an unbelievably high DUV/visible rejection ratio (R_{210}/R_{400}) of 10^8 , about 100 times higher than that of Schottky photodiodes made from the same material (Figure 17b).

Beam monitoring of excimer laser operating at the high power density in the DUV region was of particular importance

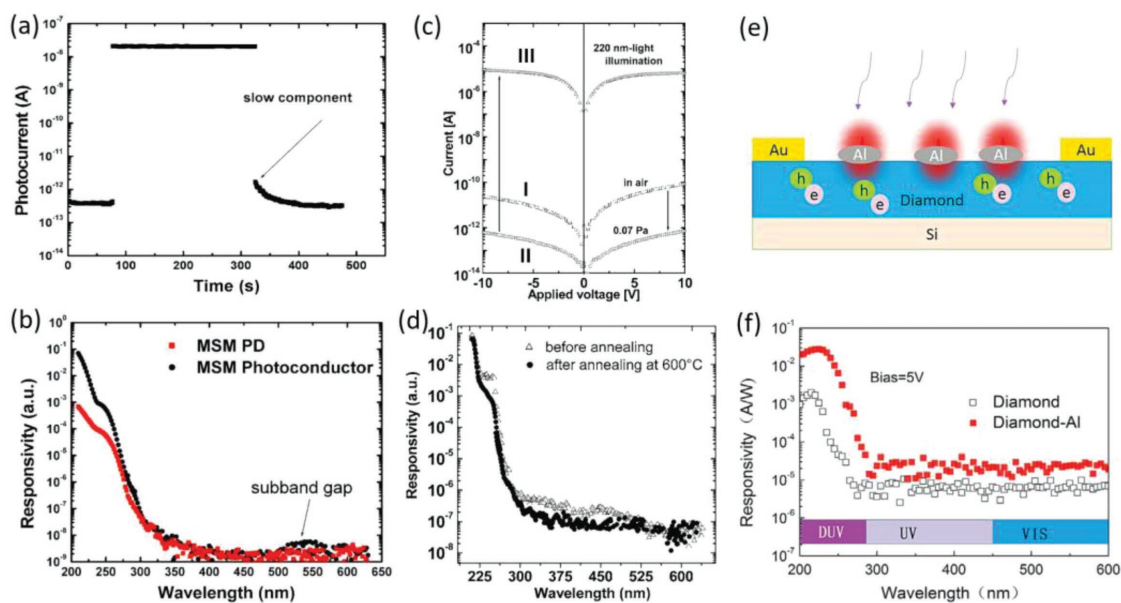


Figure 17. a) Time photoresponse of a diamond photoconductor upon 220 nm DUV light illumination. b) Spectral responsivity of the photoconductor, along with that of a Schottky photodiode made from the same material. Reproduced with permission.^[251] Copyright 2006, American Institute of Physics Publishing. c) I - V characteristics of a diamond-based MSM photodetector in dark measured in I) air, II) in dark, and III) upon 220 nm illumination under a vacuum. d) Spectral responsivity of the MSM photodetector measured on the as-grown state and after the high-temperature annealing at 600 °C, respectively. Reproduced with permission.^[257] Copyright 2005, American Institute of Physics Publishing. e) Schematic illustration of the plasmon-enhanced MSM photodetector consisting of a B-doped diamond film as the active layer between two Au electrodes with Al nanoarrays decorated. f) Spectral responsivity of the diamond MSM photodetectors with and without Al nanoarray decoration. Reproduced with permission.^[261] Copyright 2016, Taylor & Francis.

because of the rapid proliferation of excimer laser systems in areas of industrial interest like micromachining and photolithography. Benefiting from the intrinsic features of radiation hardness and visible blindness, the diamond was a good candidate for monitoring excimer laser radiation.^[244,246–250] Whitfield et al. found that sequentially applied postgrowth treatments (acid, air annealing and methane–air heating) of polycrystalline diamond prior to and following electrode fabrication can progressively change both the responsivity and response speed of diamond-based DUV photoconductors.^[248] With optimal treatment, the peak responsivity at ≈ 200 nm can be enhanced by a factor of ≈ 25 , whereas increasing treatment duration can lead to gradually shortened decay-tail component in response curves, which were related to the change of trap density and trap levels in the materials. When exposed to 193 nm excimer laser pluses with beam intensity higher than 1.5 mJ cm^{-2} and pulse repetition rates exceeding 1 MHz, the transient response of the diamond photodetector with nine treatments was virtually identical to that of a vacuum photodiode, suggesting that the devices may be sufficient for much faster solid-state laser systems. In addition, the viability of diamond photodetectors for use in molecular fluorine laser systems operating at 157 nm has also been assessed.^[249] It was observed that the photoresponse increased gradually with pulse increasing in the range of 1–1.4 mJ cm^{-2} , indicating the high possibility of these devices for application in next generation photolithography stepper tools that were indispensable in the semiconductor industry.

The fabrication of diamond-based photodetector pixels array has recently received increasing research interest due to

its promising application in DUV image sensing.^[245,252] Balducci et al. systematically compared a single-pixel detector and one pixel of a 2×10 pixels array detector.^[252] It was found that the DUV photoresponse behaviors of the two devices were very similar. Significantly, even under illumination of nano-second 193 nm excimer laser pluses, all 8 pixels can perform extremely well, with less than 2% pixel-to-pixel variation in signal response.^[245] The above results indicated good uniformity of the pixel array devices and the feasibility for fabricating DUV imaging sensor.

6.2. MSM Photodetectors

To date, a number of diamond-based MSM photodetectors have been fabricated by choosing Ti/Au, tungsten carbide (WC), Al, Au, and Pd as electrode materials which can form Schottky contacts with diamond.^[257–262] Alvarez et al. presented a high-performance MSM photodetector made from boron-doped homoepitaxial diamond thin films.^[257] The dark current of the devices was greatly reduced by more than 1 order of magnitude under vacuum condition, reaching less than 1 pA at a bias voltage of 0.4 V (Figure 17c). The detectors were highly sensitive to 220 nm DUV illumination with a very large $I_{\text{light}}/I_{\text{dark}}$ ratio of $\approx 10^7$. What is more, the peak responsivity exceeded 200 A W^{-1} at 10 V bias, indicating a large photoconductive gain due to the modification of Schottky barrier under band-to-band illumination. Once the device was annealed at 600 °C, the photoresponse at near UV–visible will be slightly suppressed, leading to a high DUV/visible rejection ratio (R_{210}/R_{630}) of 10^6 (Figure 17d).

The photoresponse of diamond-based MSM photodetectors can be optimized by shrinking the electrode spacing,^[258] exploiting surface plasmonic effect^[261] and material surface treatments.^[262] For instance, by reducing the electrode spacing from 10 to 0.14 μm , the responsivity of diamond-based MSM photodetectors increased by nearly 2 orders of magnitude from ≈ 0.34 to $\approx 15 \text{ mA W}^{-1}$ at a bias voltage of 1 V.^[258] The relatively high responsivity was ascribed to the full depletion of the shrunk electrode spacing at low biases. Through assembling of Al crescent-shaped arrays on homoepitaxial diamond thin films, Shi et al. developed a localized surface plasmon (LSP)-enhanced MSM DUVPD (Figure 17e).^[261] Under 225 nm illumination and at 5 V, the devices showed peak responsivity of 28 mA W^{-1} , which was tenfold higher than that of the pure diamond photodetector (Figure 17f). The enhancement was apparently related to near-field optical coupling between Al LSPs and diamond excitons through the improved optical absorption in the material layer.

The origins of photoconductive gain observed in diamond-based MSM photodetectors have been discussed. Liao et al. found that the gain depended strongly on both the DUV light intensity and the operation voltage.^[259] As disclosed by numerical analysis, the I - V characteristics followed thermionic-field emission tunneling at low DUV light intensity, and field-emission tunneling at high DUV light intensity, which can account for the photocurrent gain at these two light intensity regions, respectively. The tunneling processes can be related to a thin interface barrier layer at the metal/diamond interface induced

by the deep interface traps when exposed to DUV illumination. In another relevant study, it was observed that a shallow level with the activation energy of 0.21 eV and capture cross-section of $9.9 \times 10^{-20} \text{ cm}^2$ existed in the bandgap of diamond, as confirmed by charge-based deep level transient spectroscopy.^[260] Such a shallow level can trap photoinduced minority carriers during DUV light radiation process, and then detrapp slowly via thermal excitation or tunneling effect after removing the light source, leading to the persistent photoconductivity. The trapping process can also reduce the probability of carrier recombination, which contributed to the high responsivity and large photocurrent gain.

6.3. Heterojunction and Schottky Photodiodes

Graphene, a star material for its excellent property in optics and physics, has been combined with diamond thin film for DUV photodiode application (Figure 18a).^[263] Typical device fabrication procedures involve peeling off of 2 μm diamond film from the growth Si substrate, transfer of the film onto flexible substrates, and wet-transfer of graphene onto the back side of the diamond film. The zero-bias barrier height was estimated to be 0.947 and 0.89 eV for the graphene/diamond and graphene/p-diamond heterojunctions, respectively. Such a difference in barrier height is related to the Fermi level difference of graphene on diamond and p-diamond, as well as the difference in the interface defects. Upon 220 nm light

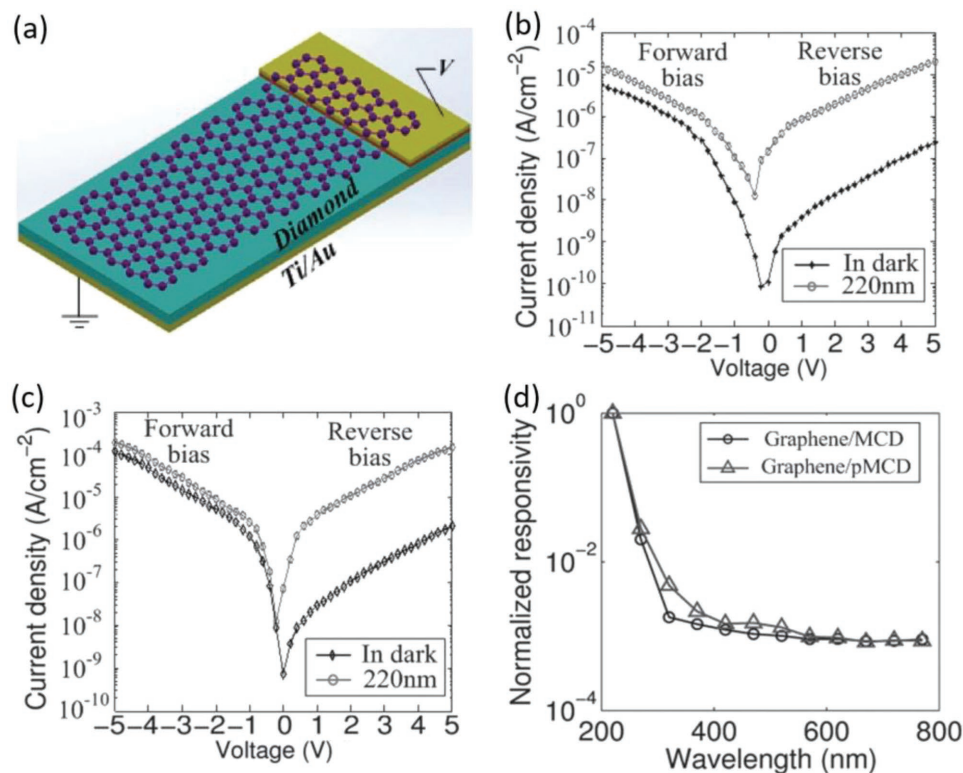


Figure 18. a) Conceptual illustration of the DUV detector based on the graphene/microcrystalline diamond heterojunction. I - V characteristics of b) graphene/diamond and c) graphene/p-diamond heterojunction photodetector in dark and upon 220 nm DUV radiation. d) Normalized spectral responsivity of the two photodetectors. Reproduced with permission.^[263] Copyright 2017, Wiley-VCH.

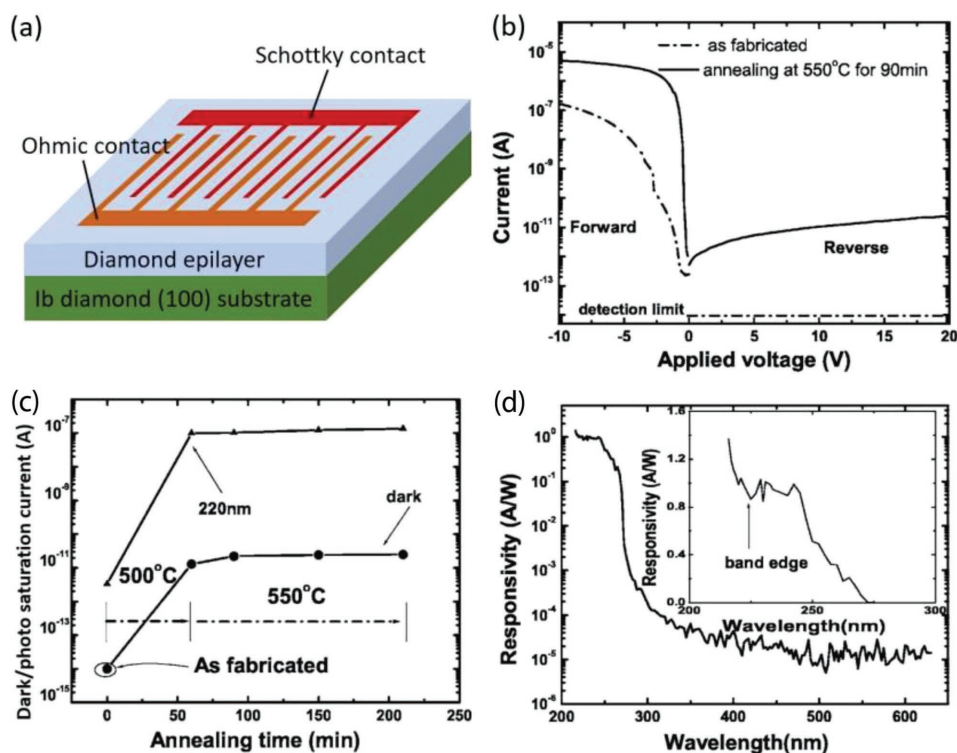


Figure 19. a) Schematic illustration of the interdigitated-finger Schottky photodiode based on diamond epilayer. b) I – V characteristics of a WC/diamond Schottky photodiode before and after annealing at 550 °C for 90 min, respectively. c) Dependence of the saturated dark current and photocurrent of the device under 220 nm DUV light illumination on the annealing temperatures and times. d) Spectral responsivity of the WC Schottky photodiode measured at -1 V bias after annealing at 550 °C for 90 min. Reproduced with permission.^[265] Copyright 2005, American Institute of Physics Publishing.

radiation, pronounced photoresponse was observed under both forward and reverse bias voltages for two devices (Figure 18b,c). The peak responsivity for the graphene/diamond and graphene/p-diamond reached 0.2 and 1.4 A W⁻¹, respectively, at a bias of -5 V. This high responsivity indicated a photocurrent gain due to the defects at graphene/diamond interface that can capture and trap photogenerated carriers. What is more, both devices exhibited a large DUV/visible rejection ratio (R_{220}/R_{400}) of $\approx 10^3$ (Figure 18d).

Other materials including Au, WC, and hafnium nitride (HfN) thin films have also been selected to assemble diamond-based Schottky photodiodes.^[264–269] Whitfield et al. reported DUV Schottky photodiodes constructed from lightly p-doped CVD-grown diamond thin films on Si substrate and 10 nm thick Au Schottky electrode.^[264] The devices showed good rectifying activity in darkness, with a reverse bias breakdown voltage exceeding 100 V and a low dark current less than 2 pA at a bias of -50 V. The detectors were sensitive to DUV illumination, with cutoff wavelength at around 220 nm. The DUV/visible rejection ratio (R_{200}/R_{600}) reached 10^5 , which was more than tenfold higher than that of interdigitated photoconductive devices. However, Koide found that thermal annealing which induced metallurgical reactions between diamond and metal will reduce Schottky barrier height of the contact metals, while metal compounds can keep stable on the diamond at elevated temperatures.^[268] With this theory, he tried to develop thermally stable diamond-based Schottky photodiodes by using

WC and HfN as Schottky contacts (Figure 19a).^[265,266] The dependence of both electrical and optoelectrical characteristics of the WC Schottky photodiodes on temperature was systematically studied.^[265] It was observed that annealing below 300 °C did not influence the electrical properties, while annealing at 550 °C can greatly optimize the ideality factor of the Schottky junctions, suggesting improved Schottky contact interface after high-temperature annealing (Figure 19b). Annealing at 550 °C also led to increased dark current from 10^{-14} to 10^{-11} A at a bias of -20 V (Figure 19c). Upon exposure to 220 nm illumination, the photocurrent of 550 °C-annealed samples was enhanced dramatically by 4×10^3 , leading to a large $I_{\text{light}}/I_{\text{dark}}$ ratio exceeding 10^4 (Figure 19c). What is more, as shown in Figure 19d, the DUV/visible rejection ratio (R_{220}/R_{500}) can reach $\approx 10^5$, and the peak responsivity was estimated to be 0.99 A W⁻¹, indicative of a photocurrent gain. As discussed in the graphene/diamond heterojunction detectors, the origin of the gain was probably related to annealing induced defects at the diamond/WC interface. In addition, they also found that at a low temperature range (room temperature to ≈ 140 °C), the short-circuit photocurrent of WC Schottky photodiodes reduced rapidly, while that of HfN Schottky devices gradually decreased with increasing annealing temperature.^[266] Note that both electrical and optoelectrical properties of these devices can keep unaffected when prolonging the annealing duration at high temperature, signifying promising potential of metal carbide and nitride contacts for developing thermally stable

diamond-based DUV Schottky photodiodes. Metal–insulator–semiconductor (MIS) DUV photodiodes with the architecture of Al/intrinsic diamond/p-doped diamond have been exhibited excellent rectifying behavior with dark current at $\approx 10^{-14}$ A at a bias of -70 V.^[270] A photovoltaic current at zero bias was observed, implying the capability to function as self-driven DUVPDs.

In summary, diamond-based photoconductors show responsivities of several A W^{-1} , $I_{\text{light}}/I_{\text{dark}}$ ratio of 10^4 , and high photoresponse rejection ratio of 10^8 , while MSM photodetectors made from diamond materials usually exhibit largely variable responsivity values from 0.34 mA W^{-1} to 200 A W^{-1} , large $I_{\text{light}}/I_{\text{dark}}$ ratio as high as 10^7 , and good photoresponse rejection ratio of 10^6 . Some strategies to enhance device performance include optimizing the electrode geometry, exploiting surface plasmonic effect and material surface treatments. On the other hand, diamond-based heterojunction and Schottky junction photodiodes typically display reasonable responsivities from 0.2 to 1.4 A W^{-1} , and decent photoresponse rejection ratio of 10^3 – 10^5 . What is more, these devices hold extremely low dark current with minimum value as low as 10^{-14} A.

7. Other Materials and Device Architectures

In the previous sections, we have introduced the research achievements of various kinds of solar-blind DUVPDs based on UWBG semiconductors including Ga_2O_3 , $\text{Mg}_x\text{Zn}_{1-x}\text{O}$, III-nitride compounds, and diamonds. In this part, we will summarize the development of solar-blind DUVPDs made from

other UWBG semiconductors such as other ternary metal oxides, perovskite oxides, and so on, and give the introduction of heterojunction-based solar-blind DUV phototransistors reported in literatures.

7.1. Other Ternary Metal Oxides

In addition to $\text{Mg}_x\text{Zn}_{1-x}\text{O}$, there are also some other ternary metal oxides which possess extremely large bandgaps and are suitable for solar-blind DUV detection. These ternary metal oxides include $\text{Ni}_x\text{Mg}_{1-x}\text{O}$,^[271] $(\text{Ga}_{1-x}\text{In}_x)_2\text{O}_3$,^[272] $\text{Zr}_{0.5}\text{Ti}_{0.5}\text{O}_2$,^[273] $\text{In}_2\text{Ge}_2\text{O}_7$,^[274–276] Zn_2GeO_4 ,^[276–279] and ZnGa_2O_4 .^[280] For example, high-quality $\text{Ni}_x\text{Mg}_{1-x}\text{O}$ thin films have been epitaxially grown on lattice matched MgO substrate via plasma-assisted MBE method.^[271] DUVPD made from the $\text{Ni}_x\text{Mg}_{1-x}\text{O}$ thin films exhibited peak responsivity of 12 mA W^{-1} at ≈ 250 nm, and a DUV/visible rejection ratio (R_{250}/R_{400}) of ≈ 800 . As an optional material for DUV photodetection, $(\text{Ga}_{1-x}\text{In}_x)_2\text{O}_3$ thin films can be grown on the sapphire substrate through sol–gel method.^[272] Optical absorption showed that bandgap of the product decreased linearly from ≈ 5.0 to ≈ 4.2 eV, as indium content increased from 0 to 0.4 (Figure 20a). It was found that photoconductors based on $(\text{Ga}_{1-x}\text{In}_x)_2\text{O}_3$ with indium content below 0.2 showed sensitivity to DUV illumination (Figure 20b). However, the DUV/near UV rejection ratio is not very high, probably due to the inferior crystalline quality of the $(\text{Ga}_{1-x}\text{In}_x)_2\text{O}_3$ thin films. Recently, novel DUV photoconductors made from solution-processed $\text{Zr}_{0.5}\text{Ti}_{0.5}\text{O}_2$ thin films have also been developed.^[273] The devices with Pt electrodes exhibited a low dark current of only 17 pA, and a responsivity of

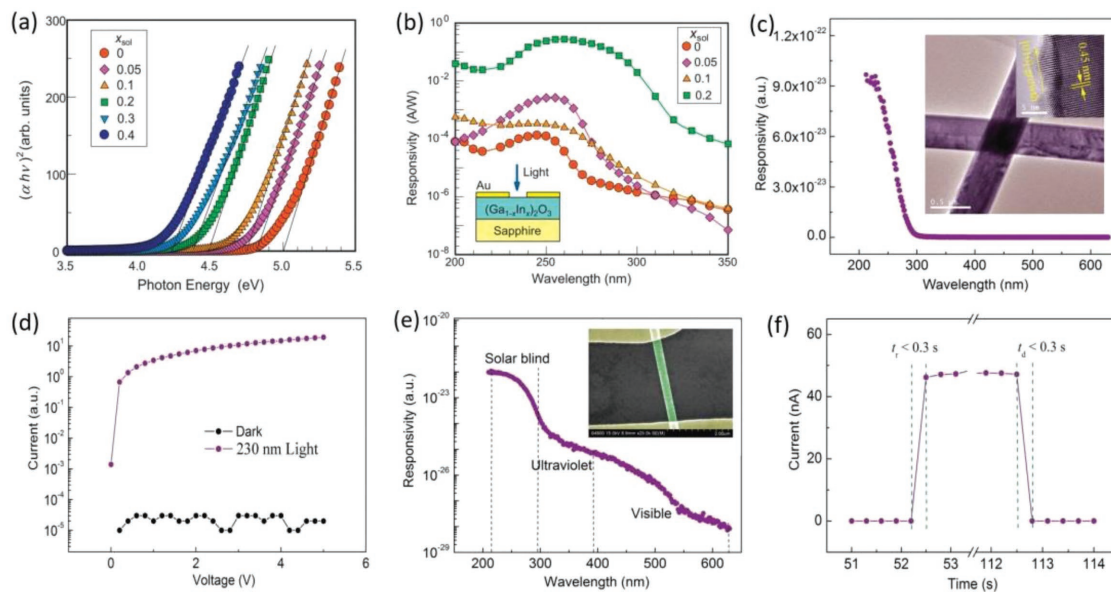


Figure 20. a) Square of absorption coefficient as a function of photon energy for sol–gel-prepared $(\text{Ga}_{1-x}\text{In}_x)_2\text{O}_3$ films in various contents. b) Spectral responsivity of photoconductors based on $(\text{Ga}_{1-x}\text{In}_x)_2\text{O}_3$ films in various contents. The inset shows the schematic illustration of the photodetector. Reproduced with permission.^[272] Copyright 2010, Wiley-VCH. c) Spectral responsivity of an individual $\text{In}_2\text{Ge}_2\text{O}_7$ -nanobelt photodetector. The inset shows the TEM image of individual nanobelt, and the corresponding HRTEM image. d) I – V curves of the photodetector in dark and upon 230 nm radiation. e) Spectral responsivity of the photodetector in semilog scale, showing the DUV/near UV and DUV/visible rejection ratios. The inset shows a typical SEM image of a nanobelt device. f) A typical cycle of time response, showing the rise and decay times. Reproduced with permission.^[274] Copyright 2010, Wiley-VCH.

620 mA W⁻¹ under 250 nm DUV radiation. Moreover, a fast response speed with rise/fall times of 424.1/154 ms was also achieved.

High-quality single-crystalline In₂Ge₂O₇ NBs have been synthesized by a vapor transport process (inset in Figure 20c).^[274] Photoconductors based on individual NB showed high sensitivity to DUV illumination with a high peak responsivity up to 3.9×10^5 A W⁻¹ at ≈ 230 nm and a cutoff wavelength at ≈ 290 nm (Figure 20c). As depicted in Figure 20d, the dark current was in the level of 10^{-14} A, and the $I_{\text{light}}/I_{\text{dark}}$ ratio was as high as $\approx 10^6$. Moreover, the DUV/near UV and DUV/visible rejection ratios were 2–3 and 3–6 orders of magnitude, respectively (Figure 20e). The devices also exhibited a fast response speed with both rise and fall times less than 0.3 s (Figure 20f). The high device performance can be related mainly to the prolonged lifetime of photocarriers due to numerous surface traps and one dimensionality which led to shortened carrier transit time. Besides, the high-quality material also contributes to the high device performance. In fact, the responsivity can be further increased to 7.34×10^5 A W⁻¹ by decorating CuO NPs onto In₂Ge₂O₇ NBs.^[275] The presence of a large number of local heterojunctions between coated NPs and NBs can enhance the spatial separation of photogenerated electrons and holes and therefore reduce charge carrier recombination.

Another promising material that has recently been extensively studied is Zn₂GeO₄ NW which can be grown by CVD method. Thanks to the unique NW–NW junction barrier-dominated

conductance for network devices, photoconductors based on Zn₂GeO₄ NW networks showed relatively fast response speed (rise/fall times: 0.3/0.2 s) to 254 nm DUV illumination.^[278] Such a DUV light-induced barrier height modulation was much faster than the oxygen absorption/desorption processes occurring at the surface of NWs. Meanwhile, MSM photodetectors composed of individual Zn₂GeO₄ NW showed an extremely low dark current less than 0.1 pA at a bias of 8 V, and DUV/visible rejection ratio (R_{245}/R_{380}) up to $\approx 10^4$.^[277] The peak responsivity can reach 38.3 A W⁻¹, which corresponded to a photocurrent gain of ≈ 200 . Through the analysis of light intensity-dependent photocurrent generation and carrier transport, the authors concluded that the gain was associated with the shrinking of the depletion region upon DUV radiation as a result of the trapping of photoexcited carriers by defect states at the NW/electrode interface. Recently, DUVPDs based on individual Zn₂GeO₄ NW with a high responsivity of 5.11×10^3 A W⁻¹ have been reported by Zhou et al. (Figure 21a–c).^[279] A decent specific detectivity of $\approx 2.91 \times 10^{11}$ Jones and a rapid response speed with rise/fall times of $\approx 10/\approx 13$ ms were achieved (Figure 21d), respectively. Such a high device performance was ascribed to the high-quality single-crystalline characteristics and large aspect ratio of the Zn₂GeO₄ NWs.

Zinc gallate (ZnGa₂O₄), the last ternary metal oxide with an ultrawide bandgap of 4.4–5.2 eV, has found application in DUVPD. By using vapor–liquid–solid (VLS), mist CVD, or MOCVD, single crystalline ZnGa₂O₄ structures in the form of nanowire, and thin film have been successfully synthesized.^[281–283] Recently, Song and co-workers reported the

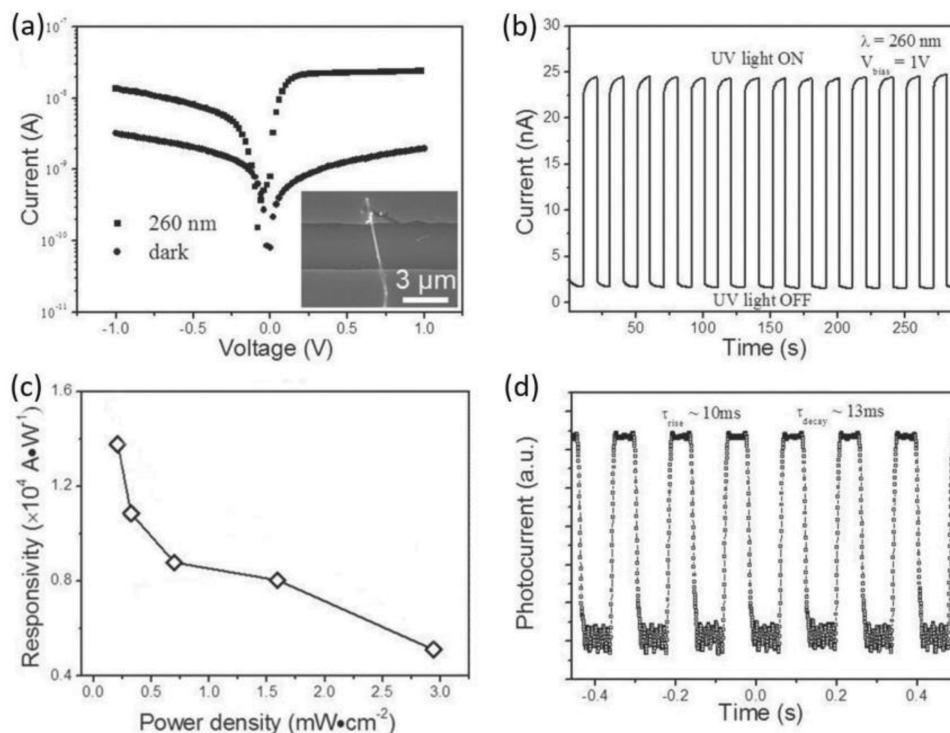


Figure 21. a) *I*–*V* curves of a Zn₂GeO₄ nanowire-based photodetector in dark and exposed to a DUV light of 260 nm. The inset shows a representative SEM image of the photodetector. b) Time response behavior of the photodetector. c) Light intensity dependent responsivity of the device at a bias of 1 V. d) The transient response measured at an incident light frequency of 10 Hz, which shows the rise and decay times. Reproduced with permission.^[279] Copyright 2010, Wiley-VCH.

synthesis of a new ZnGa_2O_4 microflower crystal through a solvothermal route.^[280] It was found that the solar-blind DUVPD based on the microflower crystal exhibits good wavelength selectivity with relatively large light to dark current ratio, fast response speed, and stable photocurrent stability at zero bias voltage.

7.2. Perovskite Oxides

Perovskite oxides refer to a group of functional materials with general formula ABO_3 or A_2BO_4 , which have attracted considerable attention during the past decades due to their advantageous features, such as dielectric, piezoelectric, ferroelectric, ferromagnetic, superconducting, and optical characteristics.^[284]

Among the perovskite oxides' family, LaAlO_3 (LAO) possesses a wide bandgap of ≈ 5.6 eV and excellent chemical and thermal stability, showing great promise as a candidate for solar-blind DUV light detection. So far, several LAO-based DUVPDs have been fabricated by choosing metal-interdigitated electrodes or ITO-metal asymmetric electrodes.^[284–286] The devices were characterized by low noise current on the order of several picoamperes in darkness. The peak responsivity achieved in these devices were tens of mA W^{-1} . For instance, LAO detectors with Au electrodes exhibited high sensitivity to 200 nm DUV illumination with a cutoff wavelength at ≈ 210 nm (Figure 22a,b).^[284] The peak responsivity was 71.8 mA W^{-1} , and a rejection ratio (R_{200}/R_{290}) reached more than 10^2 (Figure 22b). A later work found that devices with Pt-interdigitated electrodes showed much lower dark current than that of devices with Au electrodes

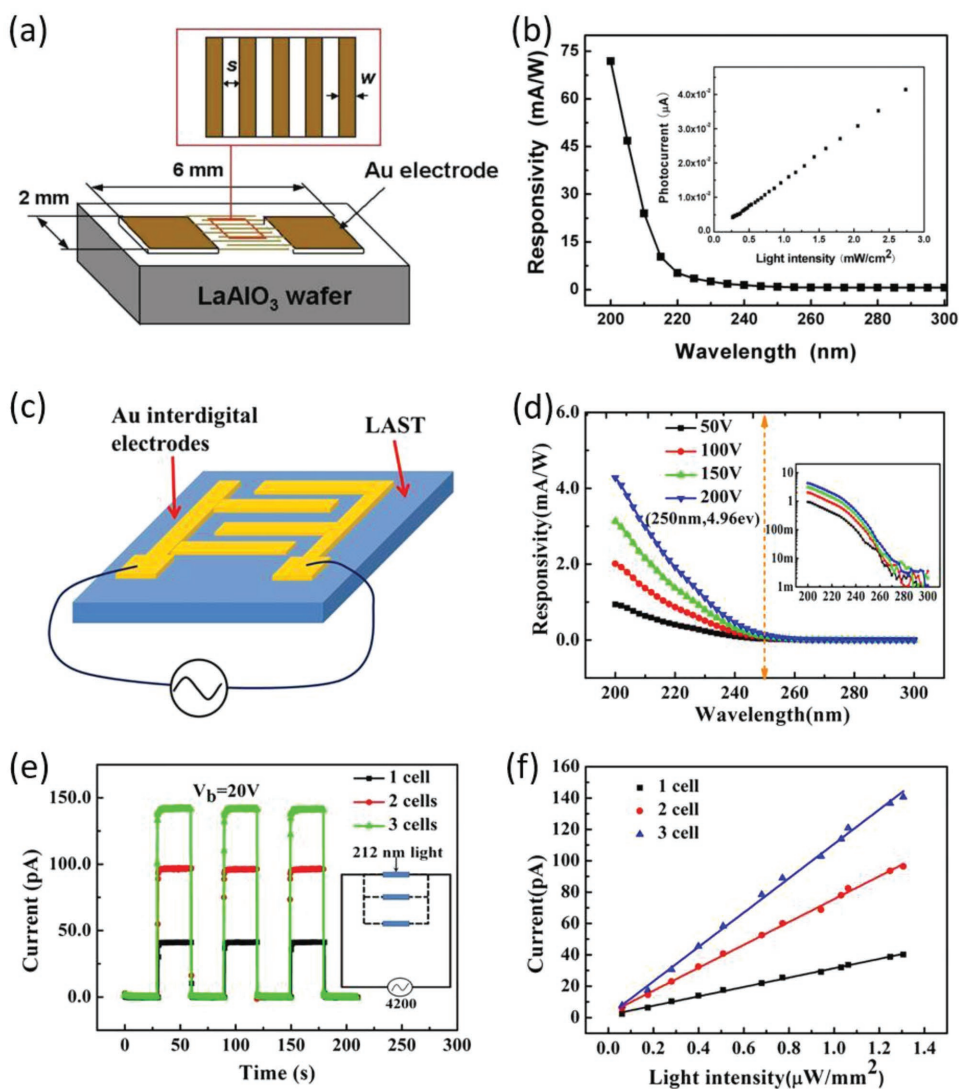


Figure 22. a) Schematic diagram of the LaAlO_3 photodetector with interdigitated electrodes. b) Spectral response of the photodetector at 10 V bias. The inset is the photocurrent variation with the incident DUV light intensity. Reproduced with permission.^[284] Copyright 2009, Optical Society Publishing. c) Schematic diagram of the LSAT photodetector with interdigital electrodes. d) Spectral response of the photodetector at different biases. Inset is a replot of responsivity curve in a logarithmic scale. e) Time response of the devices with different interdigitated electrode cell numbers under illumination of a 212 nm light at 20 V bias. The inset shows the schematic circuit of measurement. f) Photocurrent variation with the light intensity under illumination of 212 nm light with different cell numbers. Reproduced with permission.^[287] Copyright 2017, American Institute of Physics Publishing.

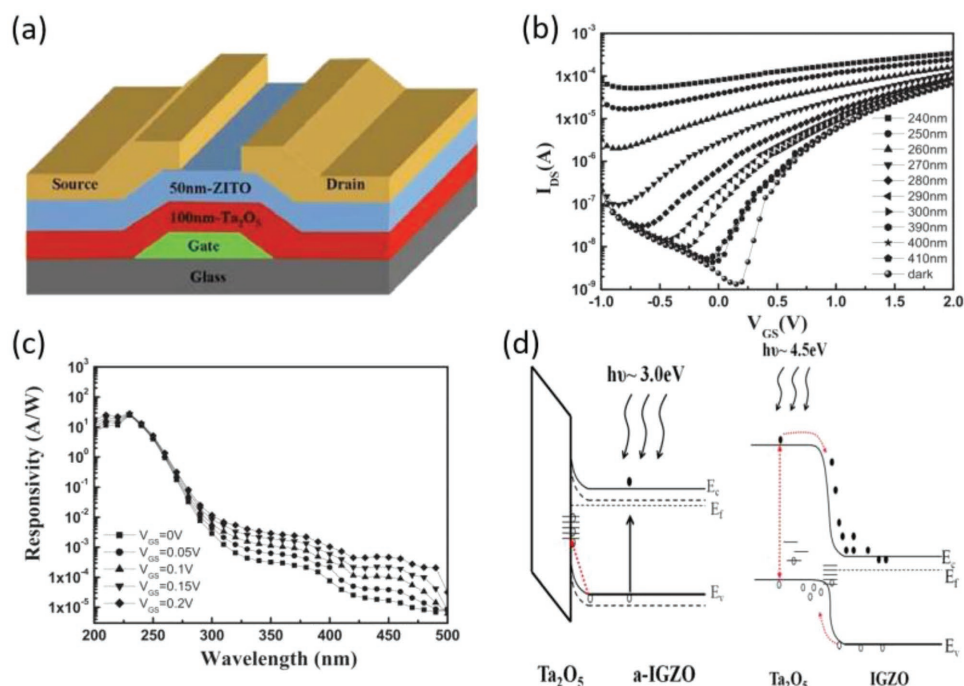


Figure 23. a) Schematic diagram of a heterojunction phototransistor with a conducting metal oxide as the charge transport channel, and a UWBG semiconductor as the DUV light absorbing media. b) Transfer characteristics of a Ta₂O₅/a-ZITO heterojunction phototransistor under illuminations with different wavelengths. Reproduced with permission.^[288] Copyright 2012, Institute of Electrical and Electronic Engineers. c) Spectral response of the device at varied gate biases. d) Energy band diagrams of the heterojunction phototransistor under illumination. Reproduced with permission.^[289] Copyright 2012, American Institute of Physics Publishing.

(4.1 vs 14.6 pA at 10 V bias), which was probably attributed to the high density steps and facets on the LAO (110) surface, and the large lattice mismatch at the Pt/LAO interface.^[285] By constructing devices with a geometry of ITO/LAO/Ag, Guo et al. presented DUVPDs with a low dark current of ≈ 1 pA at a large bias of 200 V, implying the great possibility of this material for realizing solar-blind DUVPDs with larger breakdown voltages.^[286]

In addition to LAO, DUVPDs made from (LaAlO₃)_{0.3}–(SrAl_{0.5}Ta_{0.5}O₃)_{0.7} (LSAT) single crystals have also been reported recently (Figure 22c).^[287] Under an applied voltage of 200 V, the devices exhibited a peak responsivity and specific detectivity of 4 mA W⁻¹ and $\approx 10^{11}$ Jones, at 200 nm radiation, respectively (Figure 22d). The DUV/UV rejection ratio (R_{200}/R_{290}) was more than 10³ (Figure 22d). Furthermore, the authors also found that the photocurrent response increased linearly with increasing the cell number in LSAT photodetectors with multiple interdigitated electrode cells connected in parallel (Figure 22e,f), suggesting good uniformity in photoresponse performance between different devices.

7.3. Heterojunction Phototransistors

Heterojunction phototransistors are promising for highly sensitive photodetection due to the high photocurrent gain. In previous studies, heterojunction solar-blind DUV phototransistors are mainly comprised of conducting metal oxides as the charge carrier transport channel, and UWBG semiconductors as the

absorbing media for DUV illumination (Figure 23a).^[288–291] The conducting metal oxides involved include magnetron-sputtered amorphous zinc indium tin oxide (a-ZITO) and amorphous indium gallium zinc oxide (a-IGZO) with a thickness of 50 nm, while the employed UWBG semiconductors are Ta₂O₅ or Ga₂O₃ thin films with tens to hundreds of nanometers in thickness. The UWBG semiconductors also serve as the gate dielectric layer in these devices. Typically, the devices exhibited high current on–off ratio in the range of 10⁴–10⁶, with low dark currents on the order of 10⁻¹⁰–10⁻⁹ A without DUV illumination. The dark current can be further reduced to as low as 10⁻¹¹ A by increasing oxygen partial pressure during the preparation of the Ta₂O₅ or Ga₂O₃,^[289,290] or employing a 20 nm thick SiO₂ interlayer.^[290] Upon DUV radiation, the detectors displayed high sensitivity with DUV/visible rejection ratio (R_{250}/R_{420} , R_{250}/R_{390}) reaching 10⁴–10⁶ (Figure 23b,c). Moreover, the achieved responsivities were as high as 1.38–6.4 A W⁻¹, indicating a photoconductive gain in these devices. The working mechanism of this type of devices can be interpreted by the following processes, as illustrated in Figure 23d. When shined by DUV illumination with photon energy higher than the bandgap of UWBG semiconductor (Ta₂O₅ or Ga₂O₃), electron–hole pairs are produced in both the UWBG semiconductor and conducting metal oxide (a-ZITO or a-IGZO). Owing to the alignment of band energy levels, electrons in the UWBG semiconductor drift toward the conducting metal oxide, while holes diffuse to the valence band of the conducting metal oxide or are trapped in the UWBG semiconductor. As a consequence, the photoinduced carriers are collected by the source–drain electrodes, producing high

photocurrents. Under near UV radiation, electron–hole pairs can also be generated in the conducting metal oxide due to its relatively narrower bandgap (3.3 eV for a-ZITO and 3.0 eV for a-IGZO). However, the produced photocurrent is rather limited because of the much lower absorption coefficient of a-ZITO or a-IGZO.

In another report, Shi et al. presented a heterojunction DUV phototransistors consisting of graphene as the conducting channel, which was modified with ZrO₂ quantum dots (QDs) as the DUV light absorbing media.^[292] Optical absorption of the DUV light creates electron–hole pairs in the QDs. Thanks to the formation of a built-in electric field, the holes are then transferred toward the graphene, whereas the electrons are trapped in the QDs serving as an additional light tunable gate. The transferred holes continue to transport in the graphene channel, leading to the formation of sizeable photocurrent. Specifically, such a device exhibited a high responsivity of 22 A W⁻¹ at a low operating voltage, with good wavelength selectivity to DUV wavelength range of 220–250 nm.

In summary, DUVPDs based on thin films of other ternary metal oxides usually have relatively poor device performance with responsivities of only tens to hundreds of mA W⁻¹, photoresponse rejection ratio of ≈800, and dark current in the level of 10⁻¹¹ A, whereas devices made from nanostructures of these materials can exhibit much higher responsivity values in the range of 10²–10⁵ A W⁻¹, larger photoresponse rejection ratio of 10³–10⁶, and lower dark current of 10⁻¹³–10⁻¹⁴ A. Additionally, perovskite oxide-based DUVPDs typically possess responsivities in the level of tens of mA W⁻¹, decent photoresponse rejection ratio of 10²–10³, and reasonable dark current of 10⁻¹² A. Moreover, devices made of these two group of materials have comparable specific detectivity values of ≈10¹¹ Jones. On the other hand, heterojunction DUV phototransistors, which exploit conducting metal oxides as channel materials, usually display responsivity values of 1.38–6.4 A W⁻¹, photoresponse rejection ratio of 10⁴–10⁶, and dark current in the level of 10⁻¹¹–10⁻⁹ A. Further improvement in responsivity is feasible by making use of graphene as the channel media.

8. Conclusion and Challenges

The appealing material properties of inorganic UWBG semiconductors including Ga₂O₃, Mg_xZn_{1-x}O, III-nitride compounds (Al_xGa_{1-x}N/AlN and BN), diamond, etc., have made themselves ideal platforms for solar-blind DUV light detection. Based on these materials, various types of DUVPDs, i.e., photoconductors, MSM photodetectors, p–n (p–i–n) photodiodes, Schottky photodiodes, avalanche photodiodes, and heterojunction phototransistor, which operate on different working mechanisms, have been extensively explored. So far, the detectors in reported literatures can typically attain good DUV photoresponse performance in terms of large photosensitivity ($I_{\text{light}}/I_{\text{dark}}$ ratio), low dark current, respectable responsivity, high photoresponse rejection ratio, sharp response cutoff, and relatively rapid response speed, as summarized in **Table 2**. **Figure 24** plots responsivity versus dark current of some representative DUVPDs based on UWBG

semiconductors. Clearly, Ga₂O₃-based detectors usually exhibit the highest responsivity values accompanying with large dark current, while III-nitride compound (Al_xGa_{1-x}N/AlN)-based devices normally possess extremely low dark current but suffer from low responsivity. DUVPDs made from diamond display moderate performance in both responsivity and dark current, whereas the responsivities of Mg_xZn_{1-x}O-based detectors need to be further improved. In addition, DUVPDs fabricated from micro-/nanostructures of UWBG semiconductors often show higher responsivity values, compared with those of devices based on their thin film counterpart. **Table 3** summarizes some of the typical performance parameters of reported DUV photodiodes/APDs based on UWBG semiconductors, along with those of commercial UV-enhanced Si photodiodes/APDs. Apparently, in comparison with commercial UV-enhanced Si photodiodes, UWBG semiconductor DUV photodiodes usually have comparable or even higher responsivity and specific detectivity values. Unfortunately, the response speed of these devices can hardly rival with that of commercial detectors. On the other hand, UWBG semiconductor DUV APDs (Ga₂O₃ APDs) display superior device performance in terms of much higher responsivity and specific detectivity than commercial UV-enhanced Si APDs. More importantly, UWBG semiconductor DUVPDs are operational at high temperatures and in caustic environment. The above merits pave the way for highly sensitive solar-blind DUV light detection in many practical applications, where traditional DUVPDs can scarcely be applicable properly. Some DUVPDs made from III-nitride compounds or diamonds have already been commercialized for applications such as fire sensors, engine control, or environmental monitoring. However, it is worth noting that UWBG semiconductor DUVPDs will complement rather than replace Si photodetectors at the current stage, due to issues regarding the reproducibility and reliability of the devices.

Although significant achievements have been made, there are still many challenges that need to be tackled prior to the commercialization of UWBG semiconductor-based DUVPDs. For Ga₂O₃, considerable progresses have been achieved in bulk crystal growth, epitaxial deposition, defect and impurity control, etc., which lay a solid foundation for developing high-performance DUVPDs. Semiconducting or highly conductive n-type Ga₂O₃ can be successfully produced by appropriately optimizing the growth conditions or by doping. However, there remains controversy in the origin of n-type conductivity in the material to date. On the other hand, achieving p-type doping in Ga₂O₃ is still rather difficult because of the high activation energy of acceptors and strong localization of holes. These issues greatly limit the applications of Ga₂O₃ to MSM and Schottky junction photodetectors. For Mg_xZn_{1-x}O, one big problem is the potential phase separation in alloys with moderate Mg content, which usually results in an extra response band and may degrade the performance for solar-blind DUV light detection. Another challenge pertains to the realization of effective n- and p-type doping of Mg_xZn_{1-x}O, which is crucial for fabricating high-quality p–n (p–i–n) and Schottky junction photodetectors, and additional efforts are needed in future. With regard to the III-nitride compounds, the first issue lies in the difficulties in growing high-quality Al_xGa_{1-x}N material because of the lack of a suitable

Table 2. Summary of performance parameters of some representative solar-blind DUVPDs based on UWBG semiconductors.

Geometry	Mode	Wavelength [nm]	Bandgap [eV]	I_{dark} [nA]	$I_{\text{light}}/I_{\text{dark}}$	R [A W^{-1}]	τ_r [s]/ τ_d [s]	D^* [Jones]	Ref.
Au/ β -Ga ₂ O ₃ /Au	Photoconductor	255	≈ 4.98	0.26 (20 V)	8.50×10^2 (20 V)	17		7×10^{12}	[47]
Au/Ti/ α -Ga ₂ O ₃ /Ti/Au	Photoconductor	254	≈ 5.15	1.02 (10 V)	40 (10 V)	1.50×10^{-2}	>1	–	[58]
Au-/Cr-/In-doped Ga ₂ O ₃ NB/Cr/Au	Photoconductor	250	≈ 4.90	1×10^{-4} (6 V)	9.10×10^2 (6 V)	5.47×10^2	$1/<0.60$	–	[69]
Graphene/ β -Ga ₂ O ₃ /Cr/Au	MSM photodetector	254	4.90	1.10×10^3 (4 V)	3.41×10^2 (4 V)	39.30	$94.83/2.19 \times 10^2$	5.92×10^{13}	[82]
β -Ga ₂ O ₃ /NSTO	n–n Photodiode	254	≈ 4.80	0.42 (0 V)	20 (0 V)	43.31	9.86/7.52	–	[108]
β -Ga ₂ O ₃ /Si	p–n Photodiode	254	4.90	8.50×10^2 (3 V)	9.2×10^2 (3 V)	3.70×10^2	6.33/2.99	–	[109]
ZnO/Ga ₂ O ₃ core/shell microwire	p–n Photodiode	254	4.90	1×10^{-2} (–4 V)	$\approx 10^6$ (–5 V)	1.30×10^3	$2 \times 10^{-5}/8.57 \times 10^{-4}$	9.91×10^{14}	[114]
Au/MgZnO/Au	Photoconductor	238/266	≈ 5.10	1.60×10^{-2} (15 V)	$\approx 10^4$ (15 V)	0.27	$-/1.67 \times 10^{-6}$	–	[140]
Au/MgZnO/Au	Photoconductor	270	≈ 4.20	5×10^{-3} (3 V)	3×10^4 (3 V)	4.50×10^{-3}	>1	–	[141]
MgZnO/MgO/Si	p–i–n Photodiode	240/266	7.80	–	–	1.16	$-/1.50 \times 10^{-5}$	–	[157]
Au/MgZnO/Au	MSM photodetector	267	≈ 4.3	2.67×10^{-3} (10 V)	$\approx 10^5$ (20 V)	0.31	–	1.14×10^{13}	[159]
MgZnO/Si	p–n Photodiode	–	–	2 (–3 V)	≈ 300 (± 3 V)	≈ 10.5	>10	–	[160]
PANI/MgZnO	p–n Photodiode	250	–	4.40×10^{-4} (–1 V)	6.82×10^6 (–1 V)	1.60×10^{-4}	4.80/5.10	1.50×10^{11}	[161]
metal/AlN/metal	Photoconductor	202	≈ 4.00	5×10^{-5} (30 V)	–	0.08	–	–	[171]
Pt-/B-doped GaN/Pt	MSM photodetector	266	–	4.68×10^5 (10 V)	1.85 (10 V)	0.03	$1.50 \times 10^{-8}/4.40 \times 10^{-8}$	–	[196]
Au/Mo/BN/Mo/Au	MSM photodetector	180	≈ 6.42	–	$>10^4$	3.20×10^{-2}	–	–	[201]
AlN/AlGaIn	p–n Photodiode	260	–	$(2-3) \times 10^{-4}$ (0 V)	–	2.50×10^{-2}	–	1.40×10^{12}	[209]
Al _{0.4} Ga _{0.6} N	p–i–n Photodiode	280	–	5×10^{-6} (10 V)	–	9.30×10^{-2}	>1	7.50×10^{14}	[226]
AlGaIn/Pd	Schottky photodiode	275	–	0.6 (–3 V)	$>10^3$	3.30×10^{-2}	–	–	[233]
AlN/Ni/Au	Schottky photodiode	200	6.10	1×10^{-5} (50 V)	–	0.12	–	1×10^{15}	[234]
Al/diamond/Al	Photoconductor	210	5.50	4×10^{-3} (100 V)	7.5	2	$2.50 \times 10^{-4}/-$	–	[253]
Diamond/graphene	Schottky photodiode	220	5.45	–	–	1.4	–	–	[263]
Diamond/WC	Schottky photodiode	220	5.50	$<1 \times 10^{-4}$ (5 V)	–	4×10^{-3}	$\approx 10/-$	–	[269]
Au/Pt/Ni _{0.54} Mg _{0.46} O/Pt/Au	Photoconductor	250	–	<25 (10 V)	800 (10 V)	1.20×10^{-2}	$-/7.69$	–	[271]
Pt/Zr _{0.5} Ti _{0.5} O ₂ /Pt	MSM photodetector	250	–	1.7×10^{-2} (5 V)	$>10^2$	0.62	0.42/0.15	–	[273]
Au/Cr/In ₂ Ge ₂ O ₇ NB/Cr/Au	Photoconductor	230	≈ 4.43	–	$\approx 10^6$ (5 V)	3.90×10^5	$4 \times 10^{-3}/6.93 \times 10^{-3}$	–	[274]
Au/Cr/Zn ₂ GeO ₄ NW/Cr/Au	MSM photodetector	260	4.68	1 (1 V)	≈ 10 (1 V)	5.11×10^3	0.01/1.30 $\times 10^{-2}$	2.91×10^{11}	[279]
Au/(LaAlO ₃) _{0.3} -SrAl _{0.5} Ta _{0.5} O ₃) _{0.7} /Au	Photoconductor	212	≈ 4.96	5.82×10^{-3} (200 V)	–	4×10^{-3}	$5.63 \times 10^{-10}/-$	1×10^{11}	[287]

substrate, which normally leads to a high density of defects and cracks. Some emerging solutions like LEO have proved to be useful for decreasing dislocations. Unfortunately, it is not applicable to back-illuminated photodiodes. The employment of low-temperature AlN interlayers or AlN substrates has been proved to be an effective avenue for reducing defects and cracks, which requires further exploration. Another equally important problem involves how to manufacture highly conductive p-type Al_xGa_{1-x}N thin films, because most of the acceptors are likely unionized at room temperature due to the large activation energy of the widely used Mg dopant in Al_xGa_{1-x}N with high Al content. This limits the exploration of light detection at shorter

wavelength, and thus the development of new approaches to enhance p-type conductivity, such as short period superlattices, is in urgent demand. As for diamond, in spite of the progress in growing single-crystalline material, commercially available single crystals are still not larger enough. In addition, polycrystalline diamonds of a good enough quality are not readily available to date. Therefore, appropriate technologies to produce large size diamonds of high crystalline quality should be developed to meet the requirement of the semiconductor industry. On the other hand, approaches to realize n-type doping need to be established, which sets a great challenge for applying diamond in p–n (p–i–n) and Schottky junction photodetectors.

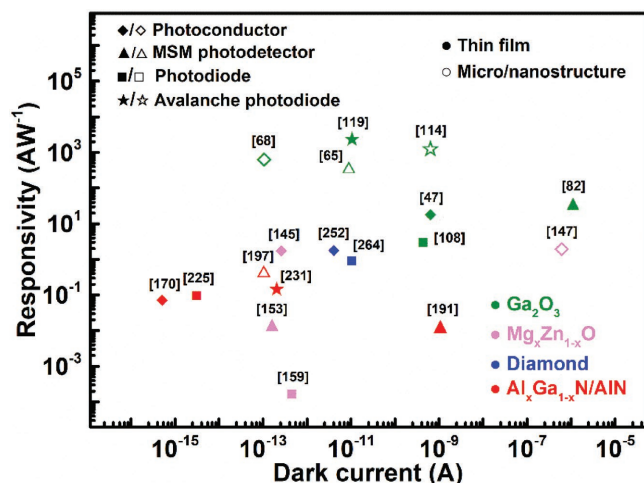


Figure 24. A plot showing responsivity versus dark current of some representative solar-blind DUVPDs based on various UWBG semiconductors.

An increasing research interest focuses on the exploration of nanostructured UWBG semiconductors (i.e., β -Ga₂O₃ NW/NB, 2D h-BN, ternary metal oxide NW/NB) in solar-blind DUV light detection, due to the possibility of low cost and large-scale production of nanostructured materials, as well as their unique material properties that enable superior device performance. Nevertheless, since the heterogeneity of nanostructured materials significantly affects the homogeneity of the device performance, reliable control of not only diameter, length, crystallinity, and orientation assembly, but also physical and chemical properties of these materials is of critical importance and remains a big challenge.

In spite of many hurdles existed in this field, there is still much room for UWBG semiconductor DUVPDs. It is envisioned that future research work should focus primarily on production of DUV sensing materials with good enough qualities, realization of both effective p- and n-type doping of

the materials, as well as rational design of novel conceptual devices. For example, the future device design should concentrate on improving the response speed, the repeatability, and reproducibility of UWBG semiconductor DUVPDs. With the above successes, the first aim for future work shall be to realize single component of DUVPDs that possess comparable or even superior device performance in all aspects, compared with commercially available DUV light detectors. On the other hand, large-area (wafer-scale) uniformity of material preparation, long-term stability and durability, large-scale production and integration, as well as environmental-friendly and cost-effective processing techniques of the devices are the most pivotal issues that require more research efforts from the perspective of practical applications. Therefore, the next aim for future work should be to realize focal plane array (FPA) by integrating individual components (pixel devices) for solar-blind DUV imager application. Currently, solar-blind FPAs with maximum 320 × 256 pixels have been realized with the use of Al_xGa_{1-x}N p-i-n photodiode arrays, and their application as solar-blind cameras have also been demonstrated.^[293,294] It is believed that more persistent efforts should be made to realize solar-blind FPAs with higher pixel resolution and to construct FPAs using other UWBG semiconductors. In addition, some new concepts such as plasmonic technologies and self-powered DUV light detection that are useful for improving device performance or reducing power consumption can be developed as well. In practice, the selection of DUV sensing materials should depend primarily on the requirement of target applications since UWBG semiconductor DUVPDs usually exhibit largely varied performance in different aspects. Additionally, the compatibility between materials and fabrication processes, as well as operation conditions should be taken into consideration when selecting photoelectric materials. It is expected that more achievements in the field of UWBG semiconductor solar-blind DUV photo-detection will be attained to meet huge demands of various applications in the future.

Table 3. Summary of typical performance parameters of UWBG semiconductor-based solar-blind DUV photodiodes/APDs and commercial UV-enhanced Si photodiodes/APDs.

	Device geometry/model	R [A W ⁻¹]	D* [Jones]	Response time [s]
UWBG semiconductor DUVPDs	Ga ₂ O ₃ photodiode	0.07–96.13	–	10 ⁻⁴ –10 ⁻³
	Ga ₂ O ₃ APD	(11.1–5.18) × 10 ³	10 ¹² –10 ¹⁵	10 ⁻⁵ –10 ⁻³
	Mg _x Zn _{1-x} O photodiode	10 ⁻⁷ –1	10 ¹¹	–
	Al _x Ga _{1-x} N photodiode	0.01–0.18	10 ¹¹ –10 ¹⁵	–
	Diamond photodiode	0.2–1.4	–	<1–≈10
Commercial UV-enhanced Si photodiodes	Photodiode (UV-001, OSI optoelectronics)	0.09–0.14 (254 nm)	≈1.4 × 10 ¹²	2 × 10 ⁻⁷
	Photodiode (UV-005DQ, OSI optoelectronics)	0.12 (200 nm)	≈6.63 × 10 ¹²	2 × 10 ⁻⁷
	Photodiode (SM1PD2A, Thorlabs)	0.08–0.12 (200–280 nm)	≈2.93 × 10 ¹²	4.5 × 10 ⁻⁷
	APD (S12053-02, Hamamatsu Photonics)	5–8 (200–250 nm)	–	–
	APD (APD410A2, Thorlabs)	4–8 (200–250 nm)	≈7.87 × 10 ¹⁰ –≈1.57 × 10 ¹¹	–
	APD (APD430A2, Thorlabs)	8–17 (200–250 nm)	≈3.78 × 10 ¹⁰ –≈8.03 × 10 ¹⁰	–

Acknowledgements

This work was supported by the National Natural Science Foundation of China (NSFC, Grant Nos. 21501038, 61575059, 61675062, 51672065), the Fundamental Research Funds for the Central Universities (Grant Nos. JZ2018HGPB0275, JZ2018HGTA0220), and the China Postdoctoral Science Foundation (Grant No. 103471013).

Conflict of Interest

The authors declare no conflict of interest.

Keywords

deep ultraviolet, light detection, optoelectronic devices, solar-blind, ultrawide-bandgap semiconductors

Received: August 27, 2018

Revised: November 20, 2018

Published online: January 7, 2019

- [1] H. Chen, H. Liu, Z. Zhang, K. Hu, X. Fang, *Adv. Mater.* **2016**, *28*, 403.
- [2] P. E. Glaser, *Science* **1968**, *162*, 857.
- [3] M. Razeghi, A. Rogalski, *J. Appl. Phys.* **1996**, *79*, 7433.
- [4] H. Chen, K. Liu, L. Hu, A. A. Al-Ghamdi, X. Fang, *Mater. Today* **2015**, *18*, 493.
- [5] U. Schühle, J.-F. Hochedez, in *Observing Photons in Space: A Guide to Experimental Space Astronomy* (Eds: M. C. E. Huber, A. Pauluhn, J. L. Culhane, J. G. Timothy, K. Wilhelm, A. Zehnder), Springer, New York, NY **2013**, pp. 467–477.
- [6] L. Sang, M. Liao, M. Sumiya, *Sensors* **2013**, *13*, 10482.
- [7] L. H. Zeng, M. Z. Wang, H. Hu, B. Nie, Y. Q. Yu, C. Y. Wu, L. Wang, J. G. Hu, C. Xie, F. X. Liang, L. B. Luo, *ACS Appl. Mater. Interfaces* **2013**, *5*, 9362.
- [8] M. Razeghi, *Proc. IEEE* **2002**, *90*, 1006.
- [9] S. J. Pearton, J. Yang, P. H. Cary, F. Ren, J. Kim, M. J. Tadjer, M. A. Mastro, *Appl. Phys. Rev.* **2018**, *5*, 011301.
- [10] Z. X. Zhang, L. H. Zeng, X. W. Tong, Y. Gao, C. Xie, Y. H. Tsang, L. B. Luo, Y. C. Wu, *J. Phys. Chem. Lett.* **2018**, *9*, 1185.
- [11] M. Razeghi, *IEEE Photonics J.* **2011**, *3*, 263.
- [12] M. Liao, Y. Koide, J. Alvarez, M. Imura, J.-P. Kleider, *Phys. Rev. B* **2008**, *78*, 045112.
- [13] E. Monroy, F. Omnès, F. Calle, *Semicond. Sci. Technol.* **2003**, *18*, R33.
- [14] M. N. Yoder, *IEEE Trans. Electron Devices* **1996**, *43*, 1633.
- [15] S. Fujita, *Jpn. J. Appl. Phys.* **2015**, *54*, 030101.
- [16] L. Zhu, W. S. Wang, Z. G. Yao, X. Q. Zhang, Y. S. Wang, *Solid-State Electron.* **2013**, *80*, 14.
- [17] M. Zhong, Z. Wei, X. Meng, F. Wu, J. Li, *J. Alloys Compd.* **2015**, *619*, 572.
- [18] X. Zhao, Z. Wu, D. Guo, W. Cui, P. Li, Y. An, L. Li, W. Tang, *Semicond. Sci. Technol.* **2016**, *31*, 065010.
- [19] Z. G. Shao, D. J. Chen, H. Lu, R. Zhang, D. P. Cao, W. J. Luo, Y. D. Zheng, L. Li, Z. H. Li, *IEEE Electron Device Lett.* **2014**, *35*, 372.
- [20] R. J. Kaplar, A. A. Allerman, A. M. Armstrong, M. H. Crawford, J. R. Dickerson, A. J. Fischer, A. G. Baca, E. A. Douglas, *ECS J. Solid State Sci. Technol.* **2017**, *6*, Q3061.
- [21] J. Y. Tsao, S. Chowdhury, M. A. Hollis, D. Jena, N. M. Johnson, K. A. Jones, R. J. Kaplar, S. Rajan, C. G. Van de Walle, E. Bellotti, C. L. Chua, R. Collazo, M. E. Coltrin, J. A. Cooper, K. R. Evans, S. Graham, T. A. Grotjohn, E. R. Heller, M. Higashiwaki, M. S. Islam, P. W. Juodawlkis, M. A. Khan, A. D. Koehler, J. H. Leach, U. K. Mishra, R. J. Nemanich, R. C. N. Pilawa-Podgurski, J. B. Shealy, Z. Sitar, M. J. Tadjer, A. F. Witulski, M. Wraback, J. A. Simmons, *Adv. Electron. Mater.* **2018**, *4*, 1600501.
- [22] S. Mitra, A. Aravindh, G. Das, Y. Pak, I. Ajia, K. Loganathan, E. Di Fabrizio, I. S. Roqan, *Nano Energy* **2018**, *48*, 551.
- [23] L. Peng, L. Hu, X. Fang, *Adv. Mater.* **2013**, *25*, 5321.
- [24] L. Su, W. Yang, J. Cai, H. Chen, X. Fang, *Small* **2017**, *13*, 1701687.
- [25] S. M. Sze, K. K. Ng, *Physics of Semiconductor Devices*, Wiley, New York **2007**.
- [26] I. B. Khriplovich, A. A. Pomeransky, *Electron. Power* **1998**, *16*, 34.
- [27] C. Xie, Y. Wang, Z.-X. Zhang, D. Wang, L. B. Luo, *Nano Today* **2018**, *19*, 41.
- [28] M. Buscema, J. O. Island, D. J. Groenendijk, S. I. Blanter, G. A. Steele, H. S. J. van der Zant, A. Castellanos-Gomez, *Chem. Soc. Rev.* **2015**, *44*, 3691.
- [29] G. Konstantatos, E. H. Sargent, *Nat. Nanotechnol.* **2010**, *5*, 391.
- [30] C. Xie, C. Mak, X. Tao, F. Yan, *Adv. Funct. Mater.* **2017**, *27*, 1603886.
- [31] X. H. Chen, S. Han, Y. M. Lu, P. J. Cao, W. J. Liu, Y. X. Zeng, F. Jia, W. Y. Xu, X. K. Liu, D. L. Zhu, *J. Alloys Compd.* **2018**, *747*, 869.
- [32] E. G. Villora, K. Shimamura, K. Kitamura, K. Aoki, *Appl. Phys. Lett.* **2006**, *88*, 031105.
- [33] M. M. Ruan, L. X. Song, Z. Yang, Y. Teng, Q. S. Wang, Y. Q. Wang, *J. Mater. Chem. C* **2017**, *5*, 7161.
- [34] A. E. Romanov, S. I. Stepanov, V. I. Nikolaev, V. E. Bougrov, *Rev. Adv. Mater. Sci.* **2016**, *44*, 63.
- [35] H. von Wenckstern, *Adv. Electron. Mater.* **2017**, *3*, 1600350.
- [36] M. Pavesi, F. Fabbri, F. Boschi, G. Piacentini, A. Baraldi, M. Bosi, E. Gombia, A. Parisini, R. Fornari, *Mater. Chem. Phys.* **2018**, *205*, 502.
- [37] Z. Ji, J. Du, J. Fan, W. Wang, *Opt. Mater.* **2006**, *28*, 415.
- [38] Y. Kokubun, K. Miura, F. Endo, S. Nakagomi, *Appl. Phys. Lett.* **2007**, *90*, 031912.
- [39] T. Oshima, T. Okuno, S. Fujita, *Jpn. J. Appl. Phys.* **2007**, *46*, 7217.
- [40] D. Guo, Z. Wu, P. Li, Y. An, H. Liu, X. Guo, H. Yan, G. Wang, C. Sun, L. Li, W. Tang, *Opt. Mater. Express* **2014**, *4*, 1067.
- [41] X. Z. Liu, P. Guo, T. Sheng, L. X. Qian, W. L. Zhang, Y. R. Li, *Opt. Mater.* **2016**, *51*, 203.
- [42] L. X. Qian, Y. Wang, Z. H. Wu, T. Sheng, X. Z. Liu, *Vacuum* **2017**, *140*, 106.
- [43] Z. H. Wu, L. X. Qian, T. Sheng, Y. Y. Zhang, X. Z. Liu, in *2016 IEEE Int. Conf. on Electron Devices and Solid-State Circuits*, IEEE, Piscataway, NJ **2016**, pp. 82–85.
- [44] L. X. Qian, X. Z. Liu, T. Sheng, W. L. Zhang, Y. R. Li, P. T. Lai, *AIP Adv.* **2016**, *6*, 045009.
- [45] D. Patil-Chaudhari, M. Ombaba, J. Y. Oh, H. Mao, K. H. Montgomery, A. Lange, S. Mahajan, J. M. Woodall, M. S. Islam, *IEEE Photonics J.* **2017**, *9*, 1.
- [46] S. Oh, Y. Jung, M. A. Mastro, J. K. Hite, C. R. Eddy, J. Kim, *Opt. Express* **2015**, *23*, 28300.
- [47] G. C. Hu, C. X. Shan, N. Zhang, M. M. Jiang, S. P. Wang, D. Z. Shen, *Opt. Express* **2015**, *23*, 13554.
- [48] S. Ahn, F. Ren, S. Oh, Y. Jung, J. Kim, M. A. Mastro, J. K. Hite, C. R. Eddy, S. J. Pearton, *J. Vac. Sci. Technol., B: Nanotechnol. Microelectron.: Mater., Process., Meas., Phenom.* **2016**, *34*, 041207.
- [49] F. Alema, B. Hertog, O. Ledyae, D. Volovik, G. Thoma, R. Miller, A. Osinsky, P. Mukhopadhyay, S. Bakhshi, H. Ali, W. V. Schoenfeld, *Phys. Status Solidi A* **2017**, *214*, 1600688.
- [50] S. Rafiqe, L. Han, H. Zhao, *Phys. Status Solidi A* **2017**, *214*, 1700063.
- [51] D. Guo, X. Qin, M. Lv, H. Shi, Y. Su, G. Yao, S. Wang, C. Li, P. Li, W. Tang, *Electron. Mater. Lett.* **2017**, *13*, 483.
- [52] W. Cui, Q. Ren, Y. S. Zhi, X. L. Zhao, Z. P. Wu, P. G. Li, W. H. Tang, *J. Nanosci. Nanotechnol.* **2018**, *18*, 3613.

- [53] Z. Wu, G. Bai, Y. Qu, D. Guo, L. Li, P. Li, J. Hao, W. Tang, *Appl. Phys. Lett.* **2016**, *108*, 211903.
- [54] Y. P. Qian, D. Y. Guo, X. L. Chu, H. Z. Shi, W. K. Zhu, K. Wang, X. K. Huang, H. Wang, S. L. Wang, P. G. Li, X. H. Zhang, W. H. Tang, *Mater. Lett.* **2017**, *209*, 558.
- [55] W. Li, X. Zhao, Y. Zhi, X. Zhang, Z. Chen, X. Chu, H. Yang, Z. Wu, W. Tang, *Appl. Opt.* **2018**, *57*, 538.
- [56] K.-Y. Chen, C.-C. Hsu, H.-C. Yu, Y.-M. Peng, C.-C. Yang, Y.-K. Su, *IEEE Trans. Electron Devices* **2018**, *65*, 1817.
- [57] H.-Y. Lee, J.-T. Liu, C.-T. Lee, *IEEE Photonics Technol. Lett.* **2018**, *30*, 549.
- [58] D. Y. Guo, X. L. Zhao, Y. S. Zhi, W. Cui, Y. Q. Huang, Y. H. An, P. G. Li, Z. P. Wu, W. H. Tang, *Mater. Lett.* **2016**, *164*, 364.
- [59] X. Zhao, Z. Wu, W. Cui, Y. Zhi, D. Guo, L. Li, W. Tang, *ACS Appl. Mater. Interfaces* **2017**, *9*, 983.
- [60] P. Feng, J. Y. Zhang, Q. H. Li, T. H. Wang, *Appl. Phys. Lett.* **2006**, *88*, 153107.
- [61] Y. Li, T. Tokizono, M. Liao, M. Zhong, Y. Koide, I. Yamada, J.-J. Delaunay, *Adv. Funct. Mater.* **2010**, *20*, 3972.
- [62] W. Y. Weng, T. J. Hsueh, S. J. Chang, G. J. Huang, S. P. Chang, *IEEE Photonics Technol. Lett.* **2010**, *22*, 709.
- [63] D. Guo, Z. Wu, P. Li, Q. Wang, M. Lei, L. Li, W. Tang, *RSC Adv.* **2015**, *5*, 12894.
- [64] W. Y. Weng, T. J. Hsueh, S.-J. Chang, G. J. Huang, S. C. Hung, *IEEE Trans. Nanotechnol.* **2011**, *10*, 1047.
- [65] J. Du, J. Xing, C. Ge, H. Liu, P. Liu, H. Hao, J. Dong, Z. Zheng, H. Gao, *J. Phys. D: Appl. Phys.* **2016**, *49*, 425105.
- [66] S. Kumar, S. Dhara, R. Agarwal, R. Singh, *J. Alloys Compd.* **2016**, *683*, 143.
- [67] L. Li, E. Auer, M. Liao, X. Fang, T. Zhai, U. K. Gautam, A. Lugstein, Y. Koide, Y. Bando, D. Golberg, *Nanoscale* **2011**, *3*, 1120.
- [68] R. Zou, Z. Zhang, Q. Liu, J. Hu, L. Sang, M. Liao, W. Zhang, *Small* **2014**, *10*, 1848.
- [69] W. Tian, C. Zhi, T. Zhai, S. Chen, X. Wang, M. Liao, D. Golberg, Y. Bando, *J. Mater. Chem.* **2012**, *22*, 17984.
- [70] W. Feng, X. Wang, J. Zhang, L. Wang, W. Zheng, P. Hu, W. Cao, B. Yang, *J. Mater. Chem. C* **2014**, *2*, 3254.
- [71] S. Oh, J. Kim, F. Ren, S. J. Pearton, J. Kim, *J. Mater. Chem. C* **2016**, *4*, 9245.
- [72] Y. Teng, L. X. Song, A. Ponchel, Z. K. Yang, J. Xia, *Adv. Mater.* **2014**, *26*, 6238.
- [73] W. Tian, H. Lu, L. Li, *Nano Res.* **2015**, *8*, 382.
- [74] D. Y. Guo, Z. P. Wu, Y. H. An, X. C. Guo, X. L. Chu, C. L. Sun, L. H. Li, P. G. Li, W. H. Tang, *Appl. Phys. Lett.* **2014**, *105*, 023507.
- [75] C.-Y. Huang, R.-H. Horng, D.-S. Wu, L.-W. Tu, H.-S. Kao, *Appl. Phys. Lett.* **2013**, *102*, 011119.
- [76] D. Zhang, W. Zheng, R. C. Lin, T. T. Li, Z. J. Zhang, F. Huang, *J. Alloys Compd.* **2018**, *735*, 150.
- [77] S. Rajamani, K. Arora, A. Belov, D. Korolev, A. Nikolskaya, Y. Usov, D. Pavlov, A. Mikhaylov, D. Tetelbaum, M. Kumar, M. Kumar, *IEEE Sens. J.* **2018**, *18*, 4046.
- [78] W. Y. Weng, T. J. Hsueh, S. J. Chang, G. J. Huang, H. T. Hsueh, *IEEE Sens. J.* **2011**, *11*, 999.
- [79] T.-C. Wei, D.-S. Tsai, P. Ravadgar, J.-J. Ke, M.-L. Tsai, D.-H. Lien, C.-Y. Huang, R.-H. Horng, J.-H. He, *IEEE J. Sel. Top. Quantum Electron.* **2014**, *20*, 112.
- [80] F.-P. Yu, S.-L. Ou, D.-S. Wu, *Opt. Mater. Express* **2015**, *5*, 1240.
- [81] A. Singh Pratiyush, S. Krishnamoorthy, S. Vishnu Solanke, Z. Xia, R. Muralidharan, S. Rajan, D. N. Nath, *Appl. Phys. Lett.* **2017**, *110*, 221107.
- [82] W.-Y. Kong, G.-A. Wu, K.-Y. Wang, T.-F. Zhang, Y.-F. Zou, D.-D. Wang, L. B. Luo, *Adv. Mater.* **2016**, *28*, 10725.
- [83] M. Ai, D. Guo, Y. Qu, W. Cui, Z. Wu, P. Li, L. Li, W. Tang, *J. Alloys Compd.* **2017**, *692*, 634.
- [84] S.-J. Cui, Z.-X. Mei, Y.-N. Hou, Q.-S. Chen, H.-L. Liang, Y.-H. Zhang, W.-X. Huo, X.-L. Du, *Chin. Phys. B* **2018**, *27*, 067301.
- [85] A. S. Pratiyush, S. Krishnamoorthy, S. Kumar, Z. Xia, R. Muralidharan, S. Rajan, D. N. Nath, *Jpn. J. Appl. Phys.* **2018**, *57*, 060313.
- [86] C. Yang, H. Liang, Z. Zhang, X. Xia, P. Tao, Y. Chen, H. Zhang, R. Shen, Y. Luo, G. Du, *RSC Adv.* **2018**, *8*, 6341.
- [87] Q. Feng, L. Huang, G. Han, F. Li, X. Li, L. Fang, X. Xing, J. Zhang, W. Mu, Z. Jia, D. Guo, W. Tang, X. Tao, Y. Hao, *IEEE Trans. Electron Devices* **2016**, *63*, 3578.
- [88] S. Oh, M. A. Mastro, M. J. Tadjer, J. Kim, *ECS J. Solid State Sci. Technol.* **2017**, *6*, Q79.
- [89] W. Mu, Z. Jia, Y. Yin, Q. Hu, J. Zhang, Q. Feng, Y. Hao, X. Tao, *CrystEngComm* **2017**, *19*, 5122.
- [90] W. Cui, D. Guo, X. Zhao, Z. Wu, P. Li, L. Li, C. Cui, W. Tang, *RSC Adv.* **2016**, *6*, 100683.
- [91] S. Ghose, S. Rahman, L. Hong, J. S. Rojas-Ramirez, H. Jin, K. Park, R. Klie, R. Droopad, *J. Appl. Phys.* **2017**, *122*, 095302.
- [92] L.-X. Qian, H.-F. Zhang, P. T. Lai, Z.-H. Wu, X.-Z. Liu, *Opt. Mater. Express* **2017**, *7*, 3643.
- [93] I. López, A. Castaldini, A. Cavallini, E. Nogales, B. Méndez, J. Piqueras, *J. Phys. D: Appl. Phys.* **2014**, *47*, 415101.
- [94] Y. L. Wu, S.-J. Chang, W. Y. Weng, C. H. Liu, T. Y. Tsai, C. L. Hsu, K. C. Chen, *IEEE Sens. J.* **2013**, *13*, 2368.
- [95] S.-H. Yuan, C.-C. Wang, S.-Y. Huang, D.-S. Wu, *IEEE Electron Device Lett.* **2018**, *39*, 220.
- [96] Y. An, X. Chu, Y. Huang, Y. Zhi, D. Guo, P. Li, Z. Wu, W. Tang, *Prog. Nat. Sci.: Mater. Int.* **2016**, *26*, 65.
- [97] R. Lin, W. Zheng, D. Zhang, Z. Zhang, Q. Liao, L. Yang, F. Huang, *ACS Appl. Mater. Interfaces* **2018**, *10*, 22419.
- [98] S. Oh, C.-K. Kim, J. Kim, *ACS Photonics* **2018**, *5*, 1123.
- [99] Y. Peng, Y. Zhang, Z. Chen, D. Guo, X. Zhang, P. Li, Z. Wu, W. Tang, *IEEE Photonics Technol. Lett.* **2018**, *30*, 993.
- [100] L.-X. Qian, Z.-H. Wu, Y.-Y. Zhang, P. T. Lai, X.-Z. Liu, Y.-R. Li, *ACS Photonics* **2017**, *4*, 2203.
- [101] S. H. Lee, S. Bin Kim, Y.-J. Moon, S. M. Kim, H. J. Jung, M. S. Seo, K. M. Lee, S.-K. Kim, S. W. Lee, *ACS Photonics* **2017**, *4*, 2937.
- [102] S. Cui, Z. Mei, Y. Zhang, H. Liang, X. Du, *Adv. Opt. Mater.* **2017**, *5*, 1700454.
- [103] W. Y. Weng, T. J. Hsueh, S. J. Chang, G. J. Huang, H. T. Hsueh, *IEEE Sens. J.* **2011**, *11*, 1491.
- [104] S. Nakagomi, T. Sato, Y. Takahashi, Y. Kokubun, *Sens. Actuators, A* **2015**, *232*, 208.
- [105] P. Li, H. Shi, K. Chen, D. Guo, W. Cui, Y. Zhi, S. Wang, Z. Wu, Z. Chen, W. Tang, *J. Mater. Chem. C* **2017**, *5*, 10562.
- [106] S. Nakagomi, T. Momo, S. Takahashi, Y. Kokubun, *Appl. Phys. Lett.* **2013**, *103*, 072105.
- [107] Y. Qu, Z. Wu, M. Ai, D. Guo, Y. An, H. Yang, L. Li, W. Tang, *J. Alloys Compd.* **2016**, *680*, 247.
- [108] D. Guo, H. Liu, P. Li, Z. Wu, S. Wang, C. Cui, C. Li, W. Tang, *ACS Appl. Mater. Interfaces* **2017**, *9*, 1619.
- [109] X. C. Guo, N. H. Hao, D. Y. Guo, Z. P. Wu, Y. H. An, X. L. Chu, L. H. Li, P. G. Li, M. Lei, W. H. Tang, *J. Alloys Compd.* **2016**, *660*, 136.
- [110] Y. An, Y. Zhi, Z. Wu, W. Cui, X. Zhao, D. Guo, P. Li, W. Tang, *Appl. Phys. A: Mater. Sci. Process.* **2016**, *122*, 1036.
- [111] K. Arora, N. Goel, M. Kumar, M. Kumar, *ACS Photonics* **2018**, *5*, 2391.
- [112] G. Shin, H.-Y. Kim, J. Kim, *Korean J. Chem. Eng.* **2018**, *35*, 574.
- [113] Z. Wu, L. Jiao, X. Wang, D. Guo, W. Li, L. Li, F. Huang, W. Tang, *J. Mater. Chem. C* **2017**, *5*, 8688.
- [114] B. Zhao, F. Wang, H. Chen, Y. Wang, M. Jiang, X. Fang, D. Zhao, *Nano Lett.* **2015**, *15*, 3988.
- [115] B. Zhao, F. Wang, H. Chen, L. Zheng, L. Su, D. Zhao, X. Fang, *Adv. Funct. Mater.* **2017**, *27*, 1700264.

- [116] M. Chen, B. Zhao, G. Hu, X. Fang, H. Wang, L. Wang, J. Luo, X. Han, X. Wang, C. Pan, Z. L. Wang, *Adv. Funct. Mater.* **2018**, *28*, 1706379.
- [117] X. Chen, Y. Xu, D. Zhou, S. Yang, F. Ren, H. Lu, K. Tang, S. Gu, R. Zhang, Y. Zheng, J. Ye, *ACS Appl. Mater. Interfaces* **2017**, *9*, 36997.
- [118] H. Li, Y. Li, G. Xiao, X. Gao, Q. Li, Y. Chen, T. Fu, T. Sun, F. Zhang, N. Yu, *Opt. Mater. Express* **2018**, *8*, 794.
- [119] W. E. Mahmoud, *Sol. Energy Mater. Sol. Cells* **2016**, *152*, 65.
- [120] Y. Chen, Y. Lu, C. Lin, Y. Tian, C. Gao, L. Dong, C. Shan, *J. Mater. Chem. C* **2018**, *6*, 5727.
- [121] K. Kikuchi, S. Imura, K. Miyakawa, M. Kubota, E. Ohta, *Thin Solid Films* **2014**, *550*, 635.
- [122] A. Kalra, S. Vura, S. Rathkanthiwar, R. Muralidharan, S. Raghavan, D. N. Nath, *Appl. Phys. Express* **2018**, *11*, 064101.
- [123] P. Jaiswal, U. Ul Muazzam, A. S. Pratiyush, N. Mohan, S. Raghavan, R. Muralidharan, S. A. Shivashankar, D. N. Nath, *Appl. Phys. Lett.* **2018**, *112*, 021105.
- [124] Z.-D. Huang, W. Y. Weng, S. J. Chang, C.-J. Chiu, T.-J. Hsueh, S.-L. Wu, *IEEE Sens. J.* **2013**, *13*, 3462.
- [125] Z.-D. Huang, W.-Y. Weng, S.-J. Chang, Y.-F. Hua, C.-J. Chiu, T.-Y. Tsai, *IEEE Photonics Technol. Lett.* **2013**, *25*, 1809.
- [126] T. Oshima, T. Okuno, N. Arai, N. Suzuki, S. Ohira, S. Fujita, *Appl. Phys. Express* **2008**, *1*, 011202.
- [127] R. Suzuki, S. Nakagomi, Y. Kokubun, N. Arai, S. Ohira, *Appl. Phys. Lett.* **2009**, *94*, 222102.
- [128] R. Suzuki, S. Nakagomi, Y. Kokubun, *Appl. Phys. Lett.* **2011**, *98*, 131114.
- [129] X. Chen, K. Liu, Z. Zhang, C. Wang, B. Li, H. Zhao, D. Zhao, D. Shen, *ACS Appl. Mater. Interfaces* **2016**, *8*, 4185.
- [130] B. Nie, J. G. Hu, L. B. Luo, C. Xie, L. H. Zeng, P. Lv, F. Z. Li, J. S. Jie, M. Feng, C. Y. Wu, Y. Q. Yu, S. H. Yu, *Small* **2013**, *9*, 2872.
- [131] X. J. Yang, D. Y. Jiang, Z. X. Guo, W. Zhang, N. Hu, Y. H. Duan, S. Gao, Q. C. Liang, T. Zheng, J. W. Lv, *Mater. Res. Bull.* **2018**, *98*, 275.
- [132] A. N. Andriotis, M. Menon, *J. Appl. Phys.* **2015**, *117*, 125708.
- [133] J. Sengupta, A. Ahmed, R. Labar, *Mater. Lett.* **2013**, *109*, 265.
- [134] B. K. Sonawane, M. P. Bhole, D. S. Patil, *Opt. Quantum Electron.* **2009**, *41*, 17.
- [135] M. N. H. Mia, M. F. Pervez, M. K. Hossain, M. Reefaz Rahman, M. J. Uddin, M. A. Al Mashud, H. K. Ghosh, M. Hoq, *Results Phys.* **2017**, *7*, 2683.
- [136] W. Yang, S. S. Hullavarad, B. Nagaraj, I. Takeuchi, R. P. Sharma, T. Venkatesan, R. D. Vispute, H. Shen, *Appl. Phys. Lett.* **2003**, *82*, 3424.
- [137] S. Han, S. M. Liu, Y. M. Lu, P. J. Cao, W. J. Liu, Y. X. Zeng, F. Jia, X. K. Liu, D. L. Zhu, *J. Alloys Compd.* **2017**, *694*, 168.
- [138] H. Chen, J. Zhang, Z. Chen, H. Liu, X. Ma, Q. Li, G. Chu, S. Chu, *J. Phys. D: Appl. Phys.* **2018**, *51*, 175104.
- [139] Z. G. Ju, C. X. Shan, D. Y. Jiang, J. Y. Zhang, B. Yao, D. X. Zhao, D. Z. Shen, X. W. Fan, *Appl. Phys. Lett.* **2008**, *93*, 173505.
- [140] S. Han, Z. Zhang, J. Zhang, L. Wang, J. Zheng, H. Zhao, Y. Zhang, M. Jiang, S. Wang, D. Zhao, C. Shan, B. Li, D. Shen, *Appl. Phys. Lett.* **2011**, *99*, 242105.
- [141] K. W. Liu, D. Z. Shen, C. X. Shan, J. Y. Zhang, D. Y. Jiang, Y. M. Zhao, B. Yao, D. X. Zhao, *J. Phys. D: Appl. Phys.* **2008**, *41*, 125104.
- [142] D. Y. Jiang, C. X. Shan, J. Y. Zhang, Y. M. Lu, B. Yao, D. X. Zhao, Z. Z. Zhang, D. Z. Shen, C. L. Yang, *J. Phys. D: Appl. Phys.* **2009**, *42*, 025106.
- [143] C. Tian, D. Jiang, Z. Tan, Q. Duan, R. Liu, L. Sun, J. Qin, J. Hou, S. Gao, Q. Liang, J. Zhao, *Mater. Res. Bull.* **2014**, *60*, 46.
- [144] G. Li, *Opt. Eng.* **2011**, *50*, 113801.
- [145] Y. Zhao, J. Zhang, D. Jiang, C. Shan, Z. Zhang, B. Yao, D. Zhao, D. Shen, *ACS Appl. Mater. Interfaces* **2009**, *1*, 2428.
- [146] M. M. Fan, K. W. Liu, Z. Z. Zhang, B. H. Li, X. Chen, D. X. Zhao, C. X. Shan, D. Z. Shen, *Appl. Phys. Lett.* **2014**, *105*, 011117.
- [147] M. M. Fan, K. W. Liu, X. Chen, X. Wang, Z. Z. Zhang, B. H. Li, D. Z. Shen, *ACS Appl. Mater. Interfaces* **2015**, *7*, 20600.
- [148] C.-Z. Wu, L.-W. Ji, S.-M. Peng, Y.-L. Chen, S.-J. Young, *Electrochem. Solid-State Lett.* **2011**, *14*, J55.
- [149] T. Takagi, H. Tanaka, S. Fujita, S. Fujita, *Jpn. J. Appl. Phys.* **2003**, *42*, L401.
- [150] Q. Zheng, F. Huang, J. Huang, Q. Hu, D. Chen, K. Ding, *IEEE Electron Device Lett.* **2012**, *33*, 1033.
- [151] F. Alema, B. Hertog, O. Ledyev, D. Volovik, R. Miller, A. Osinsky, S. Bakhshi, W. V. Schoenfeld, *Sens. Actuators, A* **2016**, *249*, 263.
- [152] L. K. Wang, Z. G. Ju, C. X. Shan, J. Zheng, D. Z. Shen, B. Yao, D. X. Zhao, Z. Z. Zhang, B. H. Li, J. Y. Zhang, *Solid State Commun.* **2009**, *149*, 2021.
- [153] L. K. Wang, Z. G. Ju, J. Y. Zhang, J. Zheng, D. Z. Shen, B. Yao, D. X. Zhao, Z. Z. Zhang, B. H. Li, C. X. Shan, *Appl. Phys. Lett.* **2009**, *95*, 131113.
- [154] Q. Zheng, F. Huang, K. Ding, J. Huang, D. Chen, Z. Zhan, Z. Lin, *Appl. Phys. Lett.* **2011**, *98*, 221112.
- [155] S. Han, J. Zhang, Z. Zhang, Y. Zhao, L. Wang, J. Zheng, B. Yao, D. Zhao, D. Shen, *ACS Appl. Mater. Interfaces* **2010**, *2*, 1918.
- [156] P. Wang, Q. Zhen, Q. Tang, Y. Yang, L. Guo, K. Ding, F. Huang, *Opt. Express* **2013**, *21*, 18387.
- [157] X. Xie, Z. Zhang, B. Li, S. Wang, M. Jiang, C. Shan, D. Zhao, H. Chen, D. Shen, *Opt. Express* **2014**, *22*, 246.
- [158] P. Wang, Q. H. Zheng, Q. Tang, Y. T. Yang, L. X. Guo, F. Huang, Z. J. Song, Z. Y. Zhang, *Opt. Lett.* **2014**, *39*, 375.
- [159] D. Jiang, C. Tian, G. Yang, J. Qin, Q. Liang, J. Zhao, J. Hou, S. Gao, *Mater. Res. Bull.* **2015**, *67*, 158.
- [160] H. L. Liang, Z. X. Mei, Q. H. Zhang, L. Gu, S. Liang, Y. N. Hou, D. Q. Ye, C. Z. Gu, R. C. Yu, X. L. Du, *Appl. Phys. Lett.* **2011**, *98*, 221902.
- [161] H. Chen, P. Yu, Z. Zhang, F. Teng, L. Zheng, K. Hu, X. Fang, *Small* **2016**, *12*, 5809.
- [162] C. Yang, X. M. Li, W. D. Yu, X. D. Gao, X. Cao, Y. Z. Li, *J. Phys. D: Appl. Phys.* **2009**, *42*, 152002.
- [163] X. Xie, Z. Zhang, B. Li, S. Wang, D. Shen, *Opt. Express* **2015**, *23*, 32329.
- [164] M. Toporkov, P. Mukhopadhyay, H. Ali, V. Beletsky, F. Alema, A. Osinsky, W. V. Schoenfeld, in *Proc. SPIE – The Int. Society for Optical Engineering* (Eds: F. H. Teherani, D. C. Look, D. J. Rogers), SPIE, Bellingham, WA **2017**, p. 101051N.
- [165] A. R. Acharya, *Himalayan Phys.* **2013**, *4*, 22.
- [166] S. C. Jain, M. Willander, J. Narayan, R. Van Overstraeten, *J. Appl. Phys.* **2000**, *87*, 965.
- [167] N. Izyumskaya, D. O. Demchenko, S. Das, Ü. Özgür, V. Avrutin, H. Morkoç, *Adv. Electron. Mater.* **2017**, *3*, 1600485.
- [168] F. A. Ponce, D. P. Bour, *Nature* **1997**, *386*, 351.
- [169] L. H. Li, Y. Chen, *Adv. Funct. Mater.* **2016**, *26*, 2594.
- [170] C. Touzi, F. Omnès, T. Boufaden, P. Gibart, B. El Jani, *Microelectron. J.* **2006**, *37*, 336.
- [171] S. Nikishin, B. Borisov, M. Pandikunta, R. Dahal, J. Y. Lin, H. X. Jiang, H. Harris, M. Holtz, *Appl. Phys. Lett.* **2009**, *95*, 054101.
- [172] T. C. Doan, J. Li, J. Y. Lin, H. X. Jiang, *AIP Adv.* **2016**, *6*, 075213.
- [173] M. Sajjad, W. M. Jadwisieniczak, P. Feng, *Nanoscale* **2014**, *6*, 4577.
- [174] M. Rivera, R. Velázquez, A. Aldabahi, A. F. Zhou, P. Feng, *Sci. Rep.* **2017**, *7*, 42973.
- [175] H. Liu, J. Meng, X. Zhang, Y. Chen, Z. Yin, D. Wang, Y. Wang, J. You, M. Gao, P. Jin, *Nanoscale* **2018**, *10*, 5559.
- [176] B. Yang, D. J. H. Lambert, T. Li, C. J. Collins, M. M. Wong, U. Chowdhury, R. D. Dupuis, J. C. Campbell, *Electron. Lett.* **2000**, *36*, 1866.

- [177] T. Li, D. J. H. Lambert, A. L. Beck, C. J. Collins, B. Yang, M. M. Wong, U. Chowdhury, R. D. Dupuis, J. C. Campbell, *J. Electron. Mater.* **2001**, *30*, 872.
- [178] F. Xie, H. Lu, D. Chen, X. Ji, F. Yan, R. Zhang, Y. Zheng, L. Li, J. Zhou, *IEEE Sens. J.* **2012**, *12*, 2086.
- [179] S. Rathkhanthiwar, A. Kalra, S. V. Solanke, N. Mohta, R. Muralidharan, S. Raghavan, D. N. Nath, *J. Appl. Phys.* **2017**, *121*, 164502.
- [180] G. Bao, D. Li, X. Sun, M. Jiang, Z. Li, H. Song, H. Jiang, Y. Chen, G. Miao, Z. Zhang, *Opt. Express* **2014**, *22*, 24286.
- [181] W. Zhang, J. Xu, W. Ye, Y. Li, Z. Qi, J. Dai, Z. Wu, C. Chen, J. Yin, J. Li, H. Jiang, Y. Fang, *Appl. Phys. Lett.* **2015**, *106*, 021112.
- [182] N. Biyikli, I. Kimukin, T. Tut, O. Aytur, E. Ozbay, *Electron. Lett.* **2005**, *41*, 274.
- [183] J. Li, Z. Y. Fan, R. Dahal, M. L. Nakarmi, J. Y. Lin, H. X. Jiang, *Appl. Phys. Lett.* **2006**, *89*, 213510.
- [184] S. V. Averine, P. I. Kuznetsov, V. A. Zhitov, N. V. Alkeev, *Solid-State Electron.* **2008**, *52*, 618.
- [185] B. N. Pantha, R. Dahal, M. L. Nakarmi, N. Nepal, J. Li, J. Y. Lin, H. X. Jiang, Q. S. Paduano, D. Weyburne, *Appl. Phys. Lett.* **2007**, *90*, 241101.
- [186] V. S. Chivukula, D. Ciplys, M. S. Shur, J. Yang, R. Gaska, in *2009 IEEE Int. Ultrasonics Symp.*, IEEE, Piscataway, NJ **2009**, pp. 2789–2792.
- [187] X. Wang, X. Wang, B. Wang, J. Ran, H. Xiao, C. Wang, G. Hu, *Front. Optoelectron. China* **2009**, *2*, 113.
- [188] F. Xie, H. Lu, D. J. Chen, P. Han, R. Zhang, Y. D. Zheng, L. Li, W. H. Jiang, C. Chen, *Electron. Lett.* **2011**, *47*, 930.
- [189] X. Li, D. Zhao, D. Jiang, Z. Liu, P. Chen, L. Le, J. Yang, X. He, S. Zhang, J. Zhu, H. Wang, B. Zhang, J. Liu, H. Yang, *J. Vac. Sci. Technol., B: Nanotechnol. Microelectron.: Mater., Process., Meas., Phenom.* **2014**, *32*, 031204.
- [190] J.-Y. Duboz, N. Grandjean, A. Dussaigne, M. Mosca, J.-L. Reverchon, P. G. Verly, R. H. Simpson, *Eur. Phys. J.: Appl. Phys.* **2006**, *33*, 5.
- [191] G. Mazzeo, G. Conte, J.-L. Reverchon, A. Dussaigne, J.-Y. Duboz, *Appl. Phys. Lett.* **2006**, *89*, 223513.
- [192] D.-S. Tsai, W.-C. Lien, D.-H. Lien, K.-M. Chen, M.-L. Tsai, D. G. Senesky, Y.-C. Yu, A. P. Pisano, J.-H. He, *Sci. Rep.* **2013**, *3*, 2628.
- [193] M. R. Chen, S. H. Chang, T. C. Chen, C. H. Hsu, H. L. Kao, J. I. Chyi, *Phys. Status Solidi A* **2010**, *207*, 224.
- [194] M. Brendel, M. Helbling, A. Knigge, F. Brunner, M. Weyers, *J. Appl. Phys.* **2015**, *118*, 244504.
- [195] M. Helbling, M. Weyers, A. Knigge, M. Brendel, F. Brunner, *Electron. Lett.* **2015**, *51*, 1598.
- [196] H. Srour, J. P. Salvestrini, A. Ahaitouf, S. Gautier, T. Moudakir, B. Assouar, M. Abarkan, S. Hamady, A. Ougazzaden, *Appl. Phys. Lett.* **2011**, *99*, 221101.
- [197] N. Gao, W. Lin, X. Chen, K. Huang, S. Li, J. Li, H. Chen, X. Yang, L. Ji, E. T. Yu, J. Kang, *Nanoscale* **2014**, *6*, 14733.
- [198] W. Zheng, F. Huang, R. Zheng, H. Wu, *Adv. Mater.* **2015**, *27*, 3921.
- [199] A. F. Zhou, A. Aldalbahi, P. Feng, *Opt. Mater. Express* **2016**, *6*, 3286.
- [200] A. Aldalbahi, M. Rivera, M. Rahaman, A. Zhou, W. Mohammed Alzuraiqi, P. Feng, *Nanomaterials* **2017**, *7*, 454.
- [201] A. Soltani, H. A. Barkad, M. Mattalah, B. Benbakhti, J.-C. De Jaeger, Y. M. Chong, Y. S. Zou, W. J. Zhang, S. T. Lee, A. BenMoussa, B. Giordanengo, J.-F. Hochedez, *Appl. Phys. Lett.* **2008**, *92*, 053501.
- [202] Y. B. Li, J. W. Zhong, L. M. Zhou, C. L. Sun, X. Wang, H. S. Yang, W. Milne, *Mater. Sci. Forum* **2016**, *879*, 1117.
- [203] J. Li, S. Majety, R. Dahal, W. P. Zhao, J. Y. Lin, H. X. Jiang, *Appl. Phys. Lett.* **2012**, *101*, 171112.
- [204] A. Aldalbahi, P. Feng, *IEEE Trans. Electron Devices* **2015**, *62*, 1885.
- [205] H. Wang, X. Zhang, H. Liu, Z. Yin, J. Meng, J. Xia, X. M. Meng, J. Wu, J. You, *Adv. Mater.* **2015**, *27*, 8109.
- [206] J. Li, T. N. Oder, M. L. Nakarmi, J. Y. Lin, H. X. Jiang, *Appl. Phys. Lett.* **2002**, *80*, 1210.
- [207] Y. Chen, Z. Zhang, H. Jiang, Z. Li, G. Miao, H. Song, *J. Mater. Chem. C* **2018**, *6*, 4936.
- [208] G. Kipshidze, V. Kuryatkov, B. Borisov, M. Holtz, S. Nikishin, H. Temkin, *Appl. Phys. Lett.* **2002**, *80*, 3682.
- [209] V. Kuryatkov, A. Chandolu, B. Borisov, G. Kipshidze, K. Zhu, S. Nikishin, H. Temkin, M. Holtz, *Appl. Phys. Lett.* **2003**, *82*, 1323.
- [210] S. Muhtadi, S. M. Hwang, A. L. Coleman, A. Lunev, F. Asif, V. S. N. Chava, M. V. S. Chandrashekar, A. Khan, *Appl. Phys. Express* **2017**, *10*, 011004.
- [211] D. Walker, V. Kumar, K. Mi, P. Sandvik, P. Kung, X. H. Zhang, M. Razeghi, *Appl. Phys. Lett.* **2000**, *76*, 403.
- [212] T. Tut, T. Yelboga, E. Ulker, E. Ozbay, *Appl. Phys. Lett.* **2008**, *92*, 103502.
- [213] G.-S. Wang, H. Lu, F. Xie, D.-J. Chen, F.-F. Ren, R. Zhang, Y.-D. Zheng, *Chin. Phys. Lett.* **2012**, *29*, 097302.
- [214] M. L. Lee, Y. H. Yeh, S. J. Tu, *IEEE J. Quantum Electron.* **2012**, *48*, 1305.
- [215] E. Cicek, R. McClintock, C. Y. Cho, B. Rahnema, M. Razeghi, *Appl. Phys. Lett.* **2013**, *103*, 181113.
- [216] E. Cicek, R. McClintock, C. Y. Cho, B. Rahnema, M. Razeghi, *Appl. Phys. Lett.* **2013**, *103*, 191108.
- [217] M. Yang, M. Chong, D. Zhao, X. Wang, Y. Su, J. Sun, X. Sun, *J. Semicond.* **2014**, *35*, 064008.
- [218] R. McClintock, A. Yasan, K. Mayes, D. Shiell, S. R. Darvish, P. Kung, M. Razeghi, *Appl. Phys. Lett.* **2004**, *84*, 1248.
- [219] C. J. Collins, U. Chowdhury, M. M. Wong, B. Yang, A. L. Beck, R. D. Dupuis, J. C. Campbell, *Appl. Phys. Lett.* **2002**, *80*, 3754.
- [220] G. Parish, S. Keller, P. Kozodoy, J. P. Ibbetson, H. Marchand, P. T. Fini, S. B. Fleischer, S. P. DenBaars, U. K. Mishra, E. J. Tarsa, *Appl. Phys. Lett.* **1999**, *75*, 247.
- [221] D. J. H. Lambert, M. M. Wong, U. Chowdhury, C. Collins, T. Li, H. K. Kwon, B. S. Shelton, T. G. Zhu, J. C. Campbell, R. D. Dupuis, *Appl. Phys. Lett.* **2000**, *77*, 1900.
- [222] C. Pernet, A. Hirano, M. Iwaya, T. Detchprohm, H. Amano, I. Akasaki, *Jpn. J. Appl. Phys.* **2000**, *39*, L387.
- [223] T. Li, D. J. H. Lambert, M. M. Wong, C. J. Collins, B. Yang, A. L. Beck, U. Chowdhury, R. D. Dupuis, J. C. Campbell, *IEEE J. Quantum Electron.* **2001**, *37*, 538.
- [224] A. Hirano, C. Pernet, M. Iwaya, T. Detchprohm, H. Amano, I. Akasaki, *Phys. Status Solidi A* **2001**, *188*, 293.
- [225] P. C. Alejandro, S. Keller, T. Li, U. K. Mishra, J. S. Speck, S. P. DenBaars, *Phys. Status Solidi A* **2004**, *201*, 2185.
- [226] N. Biyikli, I. Kimukin, O. Aytur, E. Ozbay, *IEEE Photonics Technol. Lett.* **2004**, *16*, 1718.
- [227] V. V. Kuryatkov, B. A. Borisov, S. A. Nikishin, Y. Kudryavtsev, R. Asomoza, V. I. Kuchinskii, G. S. Sokolovskii, D. Y. Song, M. Holtz, *J. Appl. Phys.* **2006**, *100*, 096104.
- [228] Y. Koide, M. Y. Liao, M. Imura, *Diamond Relat. Mater.* **2010**, *19*, 205.
- [229] J. Bao, I. Shalish, Z. Su, R. Gurwitz, F. Capasso, X. Wang, Z. Ren, *Nanoscale Res. Lett.* **2011**, *6*, 404.
- [230] M. Hou, H. So, A. J. Suria, A. S. Yalamarthy, D. G. Senesky, *IEEE Electron Device Lett.* **2017**, *38*, 56.
- [231] R. McClintock, A. Yasan, K. Minder, P. Kung, M. Razeghi, *Appl. Phys. Lett.* **2005**, *87*, 241123.
- [232] C. Yao, X. Ye, R. Sun, G. Yang, J. Wang, Y. Lu, P. Yan, J. Cao, *Appl. Phys. A: Mater. Sci. Process.* **2017**, *123*, 439.
- [233] V. Adivarahan, G. Simin, G. Tamulaitis, R. Srinivasan, J. Yang, M. Asif Khan, M. S. Shur, R. Gaska, *Appl. Phys. Lett.* **2001**, *79*, 1903.
- [234] R. Dahal, T. M. Al Tahtamouni, Z. Y. Fan, J. Y. Lin, H. X. Jiang, *Appl. Phys. Lett.* **2007**, *90*, 263505.

- [235] T. M. Al tahtamouni, J. Y. Lin, H. X. Jiang, *Appl. Phys. Lett.* **2012**, *101*, 192106.
- [236] N. Biyikli, I. Kimukin, T. Kartaloglu, O. Aytur, E. Ozbay, *Appl. Phys. Lett.* **2003**, *82*, 2344.
- [237] L. van Schalkwyk, W. E. Meyer, J. M. Nel, F. D. Auret, P. N. M. Ngoepe, *Phys. B* **2014**, *439*, 93.
- [238] A. Banerjee, D. Bernoulli, H. Zhang, M.-F. Yuen, J. Liu, J. Dong, F. Ding, J. Lu, M. Dao, W. Zhang, Y. Lu, S. Suresh, *Science* **2018**, *360*, 300.
- [239] E. Kohn, M. Adamschik, P. Schmid, A. Denisenko, A. Aleksov, W. Ebert, *J. Phys. D: Appl. Phys.* **2001**, *34*, R77.
- [240] W. J. Zhang, X. M. Meng, C. Y. Chan, Y. Wu, I. Bello, S. T. Lee, *Appl. Phys. Lett.* **2003**, *82*, 2622.
- [241] R. Long, Y. Dai, M. Guo, L. Yu, B. Huang, R. Zhang, W. Zhang, *Diamond Relat. Mater.* **2008**, *17*, 234.
- [242] A. Mainwood, *Semicond. Sci. Technol.* **2000**, *15*, R55.
- [243] Y.-J. Lu, C.-N. Lin, C.-X. Shan, *Adv. Opt. Mater.* **2018**, *6*, 1800359.
- [244] S. P. Lansley, O. Gaudin, M. D. Whitfield, R. D. McKeag, N. Rizvi, R. B. Jackman, *Diamond Relat. Mater.* **2000**, *9*, 195.
- [245] S. P. Lansley, O. A. Williams, H. Ye, N. Rizvi, M. D. Whitfield, R. D. McKeag, R. B. Jackman, *Phys. Status Solidi A* **2002**, *193*, 476.
- [246] G. Mazzeo, G. Conte, M. C. Rossi, S. Salvatori, V. Ralchenko, *Phys. Status Solidi C* **2004**, *1*, 261.
- [247] G. Mazzeo, G. Prestopino, G. Conte, S. Salvatori, *Sens. Actuators, A* **2005**, *123*, 199.
- [248] M. D. Whitfield, S. P. Lansley, O. Gaudin, R. D. McKeag, N. Rizvi, R. B. Jackman, *Diamond Relat. Mater.* **2001**, *10*, 650.
- [249] M. D. Whitfield, S. P. Lansley, O. Gaudin, R. D. McKeag, N. Rizvi, R. B. Jackman, *Diamond Relat. Mater.* **2001**, *10*, 693.
- [250] R. Brescia, A. De Sio, E. Pace, M. C. Castex, *Diamond Relat. Mater.* **2004**, *13*, 938.
- [251] M. Liao, Y. Koide, *Appl. Phys. Lett.* **2006**, *89*, 113509.
- [252] A. Balducci, M. Bruzzi, A. De Sio, M. G. Donato, G. Faggio, M. Marinelli, G. Messina, E. Milani, M. E. Morgada, E. Pace, G. Pucella, S. Santangelo, M. Scoccia, S. Scuderi, A. Tucciarone, G. Verona-Rinati, *Nucl. Instrum. Methods Phys. Res., Sect. A* **2006**, *567*, 188.
- [253] E. V. Gorokhov, A. N. Magunov, V. S. Feshchenko, A. A. Altukhov, *Instrum. Exp. Tech.* **2008**, *51*, 280.
- [254] F. Mendoza, V. Makarov, B. R. Weiner, G. Morell, *Appl. Phys. Lett.* **2015**, *107*, 201605.
- [255] M. D. Whitfield, S. P. Lansley, O. Gaudin, R. D. Mckeag, N. Rizvi, R. B. Jackman, *Phys. Status Solidi A* **2001**, *185*, 99.
- [256] S. Manolopoulos, D. Clarke, G. Derbyshire, G. Jones, P. Read, M. Torbet, *Nucl. Instrum. Methods Phys. Res., Sect. A* **2003**, *510*, 406.
- [257] J. Alvarez, M. Liao, Y. Koide, *Appl. Phys. Lett.* **2005**, *87*, 113507.
- [258] M. Liao, J. Alvarez, M. Imura, Y. Koide, *Appl. Phys. Lett.* **2007**, *91*, 163510.
- [259] M. Liao, X. Wang, T. Teraji, S. Koizumi, Y. Koide, *Phys. Rev. B* **2010**, *81*, 033304.
- [260] L. Wang, X. Chen, G. Wu, W. Guo, S. Cao, K. Shang, W. Han, *Thin Solid Films* **2011**, *520*, 752.
- [261] X. Shi, Z. Yang, S. Yin, H. Zeng, *Mater. Technol.* **2016**, *31*, 544.
- [262] F. N. Li, J. W. Zhang, X. L. Wang, Z. C. Liu, W. Wang, J. Fu, T. F. Zhu, H. X. Wang, *Superlattices Microstruct.* **2016**, *100*, 258.
- [263] M. Wei, K. Yao, Y. Liu, C. Yang, X. Zang, L. Lin, *Small* **2017**, *13*, 1701328.
- [264] M. D. Whitfield, S. S. M. Chan, R. B. Jackman, *Appl. Phys. Lett.* **1996**, *68*, 290.
- [265] M. Liao, Y. Koide, J. Alvarez, *Appl. Phys. Lett.* **2005**, *87*, 022105.
- [266] Y. Koide, M. Liao, J. Alvarez, *Diamond Relat. Mater.* **2006**, *15*, 1962.
- [267] M. Liao, Y. Koide, J. Alvarez, *Appl. Phys. Lett.* **2007**, *90*, 123507.
- [268] Y. Koide, *Appl. Surf. Sci.* **2008**, *254*, 6268.
- [269] M. Liao, L. Sang, T. Teraji, M. Imura, J. Alvarez, Y. Koide, *Jpn. J. Appl. Phys.* **2012**, *51*, 090115.
- [270] D. Alfieri, S. Almaviva, A. De Sio, M. G. Donato, G. Faggio, A. Giannini, G. Messina, S. Morgante, E. Pace, S. Santangelo, S. Scuderi, P. Tripodi, *Radiat. Eff. Defects Solids* **2010**, *165*, 737.
- [271] J. W. Mares, R. C. Boutwell, M. Wei, A. Scheurer, W. V. Schoenfeld, *Appl. Phys. Lett.* **2010**, *97*, 161113.
- [272] Y. Kokubun, T. Abe, S. Nakagomi, *Phys. Status Solidi A* **2010**, *207*, 1741.
- [273] M. Zhang, X. Gu, K. Lv, W. Dong, S. Ruan, Y. Chen, H. Zhang, *Appl. Surf. Sci.* **2013**, *268*, 312.
- [274] L. Li, P. S. Lee, C. Yan, T. Zhai, X. Fang, M. Liao, Y. Koide, Y. Bando, D. Golberg, *Adv. Mater.* **2010**, *22*, 5145.
- [275] W. Tian, C. Zhi, T. Zhai, X. Wang, M. Liao, S. Li, S. Chen, D. Golberg, Y. Bando, *Nanoscale* **2012**, *4*, 6318.
- [276] Z. Liu, H. Huang, B. Liang, X. Wang, Z. Wang, D. Chen, G. Shen, *Opt. Express* **2012**, *20*, 2982.
- [277] C. Li, Y. Bando, M. Liao, Y. Koide, D. Golberg, *Appl. Phys. Lett.* **2010**, *97*, 161102.
- [278] C. Yan, N. Singh, P. S. Lee, *Appl. Phys. Lett.* **2010**, *96*, 053108.
- [279] X. Zhou, Q. Zhang, L. Gan, X. Li, H. Li, Y. Zhang, D. Golberg, T. Zhai, *Adv. Funct. Mater.* **2016**, *26*, 704.
- [280] Y. Teng, L. X. Song, W. Liu, Z. Y. Xu, Q. S. Wang, M. M. Ruan, *J. Mater. Chem. C* **2016**, *4*, 3113.
- [281] Z. Lou, L. Li, G. Shen, *Nano Res.* **2015**, *8*, 2162.
- [282] T. Oshima, M. Niwa, A. Mukai, T. Nagami, T. Suyama, A. Ohtomo, *J. Cryst. Growth* **2014**, *386*, 190.
- [283] R.-H. Horng, C.-Y. Huang, S.-L. Ou, T.-K. Juang, P.-L. Liu, *Cryst. Growth Des.* **2017**, *17*, 6071.
- [284] J. Xing, E. Guo, K. Jin, H. Lu, J. Wen, G. Yang, *Opt. Lett.* **2009**, *34*, 1675.
- [285] E.-J. Guo, H.-B. Lu, M. He, J. Xing, K.-J. Jin, G.-Z. Yang, *Appl. Opt.* **2010**, *49*, 2557.
- [286] M. Zhang, G. Liu, X. Gu, J. Zhou, W. Guo, L. Shen, S. Ruan, *J. Nanosci. Nanotechnol.* **2014**, *14*, 3827.
- [287] J. Du, C. Ge, J. Xing, J. Li, K. Jin, J. Yang, H. Guo, M. He, C. Wang, H. Lu, G. Yang, *AIP Adv.* **2017**, *7*, 035302.
- [288] C. J. Chiu, S. S. Shih, W.-Y. Weng, S.-J. Chang, Z. D. Hung, T.-Y. Tsai, *IEEE Photonics Technol. Lett.* **2012**, *24*, 1018.
- [289] T. H. Chang, C. J. Chiu, W. Y. Weng, S. J. Chang, T. Y. Tsai, Z. D. Huang, *Appl. Phys. Lett.* **2012**, *101*, 261112.
- [290] T. H. Chang, C. J. Chiu, S. J. Chang, T. Y. Tsai, T. H. Yang, Z. D. Huang, W. Y. Weng, *Appl. Phys. Lett.* **2013**, *102*, 221104.
- [291] S.-J. Chang, T. H. Chang, W. Y. Weng, C. J. Chiu, S. P. Chang, *IEEE J. Sel. Top. Quantum Electron.* **2014**, *20*, 125.
- [292] X. Shi, X. Liu, H. Zeng, *Mater. Res. Bull.* **2017**, *96*, 458.
- [293] R. McClintock, K. Mayes, A. Yasan, D. Shiell, P. Kung, M. Razeghi, *Appl. Phys. Lett.* **2005**, *86*, 011117.
- [294] J. P. Long, S. Varadaraajan, J. Matthews, J. F. Schetzina, *Opto-Electron. Rev.* **2002**, *10*, 251.